

Studies of soil-vegetation-atmosphere feedback processes with WRF on the convection permitting scale

**Dissertation zur Erlangung des Doktorgrades der Naturwissenschaften
(Dr. rer. nat.)**

**Fakultät Naturwissenschaften
Universität Hohenheim**

Institut für Physik und Meteorologie (IPM)

vorgelegt von

Josipa Milovac

aus Kroatien



Stuttgart – Hohenheim, 2016

Dean: Prof. Dr. Heinz Breer

1st reviewer: Prof. Dr. Volker Wulfmeyer

2nd reviewer: Prof. Dr. Clemens Simmer

Submitted on: 19 July 2016

Oral examination on: 28 November 2016

In dedication to my late grandmother

Marija Čikotić

(1938-2015),

Who was my life mentor, a genuinely humble, strong and truly amazing woman, a fighter who I miss so much.

Acknowledgements

This thesis presents an outcome of a three years' PhD research within the Project PAK 346/RU 1695 funded by Deutsche Forschungsgemeinschaft [(DFG), German Research Council] and supported by a grant from the Ministry of Science, Research and Arts of Baden-Württemberg (AZ Zu 33-721.3-2). The University of Hohenheim Differential Absorption Lidar measurements were performed within the Project Transregio 32, also funded by DFG.

All the research work and this thesis would not have been possible without the support and guidance of certain extraordinary people I was lucky enough to be surrounded with. I am using the opportunity here to assert my deep gratitude to those people who left a deep footprint on my professional and personal life during these research years.

First and foremost, I would like to express my sincere gratitude to my advisors Dr. Kirsten Warrach-Sagi and Prof. Dr. Volker Wulfmeyer for recognising my scientific potential and giving me an opportunity to become a part of an amazing community of scientists at the Institute of Physics and Meteorology at the University of Hohenheim. Their continuous support, constructive discussions and criticism, patience, motivation, and immense knowledge were crucial in all stages of my research journey.

I would like to thank all my colleagues from the Institute of Physics and Meteorology, namely Alexander Geissler, Dr. Viktoria Mohr, Elizabeth Ott, Dr. Hans-Stefan Bauer, Simon Metzendorf, Dr. Eva Hammann, Dr. Hans-Dieter Wize mann, Dr. Andrea Riede, Dr. Atoossa Bakhshaii and Dr. Takuya Kawabata for all the support and their comradeship. Special thanks to Dr. Thomas Schwitalla for his scientific and endless technical support, as well as to Dr. Andreas Behrendt and Florian Späth for sharing their expertise and helping me to broaden my knowledge with respect to the meteorological measurements and instrumentation. A very special thanks goes to Dr. Oliver Branch for sharing his knowledge unselfishly and continuously, and for being a friend and unconditional support all the way through my study.

My sincere appreciation is extended to all the people involved in the RU 1695 project, particularly to Dr. Joachim Ingwersen for sharing his knowledge and always giving valuable advices and constructive comments.

I am forever indebted to Prof. Dr. Branko Grisogono who was the wind beneath my wings always when I needed it, especially in the moment when I was about to change the direction in my professional life from operational to scientific meteorology. His pushing the boundaries brought me to the place where I am today.

A special thanks goes to Marko, Matea, Nina, Sanja, Mladen, Anita, Ivana, Viktorija, Josip, Marina, Edita, Vlatka, and Tomislav for their unconditional friendship, love, patience and endless support, which gave me strength to move forward.

Finally, I take this opportunity to express the profound gratitude from the bottom of my heart to my beloved family, brother Mirko, sis Tash, and especially to my mum Meri and my father Branko for always believing in me. Their endless love gave me the spiritual strength to overcome all the obstacles that came on my way all these years and to be the person I am.

Zusammenfassung

Landsystemmodelle, die Wechselwirkungen zwischen Land und Atmosphäre sowie Mensch und Umwelt berücksichtigen können, sind für verlässliche Klimaprojektionen in heterogenen, landwirtschaftlich geprägte Regionen von großer Bedeutung. Bei einer Auflösung, die fein genug ist, um eine detaillierte Landnutzung zu berücksichtigen, benötigen Modelle eine differenzierte Darstellung der Prozesse in der planetaren Grenzschicht (PBL) und an der Landoberfläche, um Änderungen von Schlüsselkomponenten wie Niederschlag oder Temperatur vorhersagen zu können. Die Bewertung von Turbulenzparametrisierungen und Landoberflächenmodellen (LSM) ist wesentlich für die Weiterentwicklung von Modellen, aber auch für das Verständnis wichtiger Phänomene wie Rückkopplungen im Boden-Vegetation-Atmosphäre (SVA) Kontinuum. Aufgrund fehlender geeigneter Beobachtungen wurden bisher jedoch aussagekräftige Bewertungen erschwert. In der vorliegenden Arbeit wird basierend auf bisher einzigartigen Profilmessungen der Einfluss der Verwendung unterschiedlicher PBL-Parameterisierungen und LSMen untersucht. Außerdem wird ermittelt, wie SVA-Rückkopplungen im Modell simuliert werden.

Mit dem Weather Research and Forecasting (WRF) Modell wurde ein Ensemble von sechs Modellläufen bei konvektionserlaubender Auflösung mit unterschiedlichen Kombinationen von LSMen (NOAH und NOAH-MP) und PBL-Parameterisierungen (zwei lokale und zwei nicht-lokale Ansätze) verwirklicht. Die Analyse wurde für zwei Fallstudien – einer trockenen und einer konvektiven Wetterlage – für drei unterschiedliche Standorte in Deutschland durchgeführt. Für die trockene Fallstudie wurden Haupteigenschaften der konvektiven PBL (CBL) analysiert und Simulationen mit hochauflösenden Wasserdampf-Differential Absorption Lidar (DIAL) Messungen verglichen. Bei der konvektiven Fallstudie lag der Schwerpunkt auf der Untersuchung der Modelldarstellung des Umfelds vor dem Konvektionsereignis mit anschließender Konvektion und folgendem Niederschlag. In beiden Fällen wurde das Verhalten der simulierten SVA-Rückkopplungsprozesse basierend auf einem innovativen “Mischungsdiagramm-Ansatz“ beurteilt.

Die Ergebnisse zeigen, dass die nicht-lokalen PBL-Parameterisierungen eine trockenere und höhere CBL erzeugen als die lokalen PBL-Parameterisierungen. Diese Ergebnisse

sind abhängig von Parametern, die in den Prandtl-Schicht-Parametrisierungen berechnet werden und häufig selbst mit den PBL-Parametrisierungen verbunden sind. Desweiteren erzeugt das LSM NOAH-MP trockenere Bedingungen in der Atmosphäre als NOAH; der Unterschied beträgt bis zu 1.4 gkg^{-1} in den Profilen der Mischungsverhältnisse. In der oberen CBL sind diese Unterschiede stärker ausgeprägt als in Bodennähe. Die Mischungsdiagramme weisen darauf hin, dass diese Abweichungen hauptsächlich auf die Entrainment-Flüsse zurückzuführen sind. Bei der trockenen Fallstudie ist das Entrainment der trockenen Luft bei NOAH-MP bis zu 6 mal größer als mit NOAH, während bei der konvektiven Fallstudie der Unterschied schwächer ist (bis zu 1.5 mal höher mit NOAH-MP). Dieses Ergebnis legt nahe, dass der Unterschied der Simulation der CBL zwischen den beiden LSMen stark mit der Aufteilung der Energie an der Landoberfläche verbunden ist – je höher das Bowen-Verhältnis, desto höher der Unterschied zwischen den LSMen. Demnach scheint WRF auf die Wahl der LSMe empfindlicher zu reagieren, wenn das Bowen-Verhältnis höher ist. NOAH und NOAH-MP wiesen in Bezug auf den Feuchtegehalt der freien Troposphäre deutliche Unterschiede auf, welche wiederum das Verhalten der simulierten Konvektion und des damit verbundenen Niederschlags stark beeinflussen. Wie sensitiv die räumliche Variabilität und der Niederschlag bezüglich des LSM und der PBL Parametrisierung sind, hängt deutlich von der Region ab.

Ein deutliches Ergebnis dieser Arbeit ist die Erkenntnis, dass WRF bei der Grenzschichtentwicklung empfindlicher auf die Wahl des LSMs als auf die Wahl der PBL-Parametrisierung reagiert. Zudem ist der Einfluss dieser Sensitivität nicht auf die untere CBL beschränkt, sondern reicht hoch bis zur Inversionsschicht und der unteren Troposphäre sowohl für trockene als auch konvektive Wetterlagen. Andererseits zeigte sich, dass die simulierte Stärke der Kopplung zwischen Landoberfläche und Atmosphäre stark vom Bowen-Verhältnis abhängt.

Diese Synergien von hochauflösenden Messungen und Modellsimulationen in Verbindung mit einer verbesserten Darstellung der Landoberflächenprozesse wird nicht nur weitere Parametrisierungsentwicklungen unterstützen, sondern auch unser Verständnis des Zusammenspiels zwischen Landoberfläche und Atmosphäre erweitern.

Abstract

Land system models which can incorporate land-atmosphere and human-environment interactions are vital for reliable climate projections in heterogeneous agricultural landscapes. At resolutions fine enough to resolve detailed land use, models need a sophisticated representation of planetary boundary layer (PBL) and land surface processes in order to predict changes in key quantities like precipitation or temperatures. Assessment of turbulence schemes and land surface models (LSM) is fundamental therefore not only to advance model development, but also to understand important phenomena like feedbacks within the soil-vegetation-atmosphere (SVA) continuum. Up until now however, a lack of appropriate observations has impeded any comprehensive assessments. Here, through comparisons with so far unique profile measurements, the study investigates the impact of using different PBL schemes and LSMs, and explores how SVA feedbacks are simulated by the model.

Using the Weather Research and Forecasting (WRF) model, a six member ensemble was run, at a convection permitting resolution, with varying combinations of LSMs (NOAH and NOAH-MP) and PBL schemes (two local and two non-local approaches). The analysis was performed for two case studies – a dry and a convective weather situation – in three different locations in Germany. During the dry case, key convective PBL (CBL) features were analysed, and the simulations were compared with high resolution water vapour differential absorption lidar measurements. For the convective case, the focus was on exploring the model representation of the pre-convective environment and the ensuing convection and precipitation. In both cases, the nature of the simulated SVA feedback processes was assessed through an innovative “mixing diagram” approach.

Results show that the nonlocal PBL schemes produce a drier and higher CBL than the local schemes. These results are sensitive to parameters calculated in the surface layer schemes, which are themselves often paired with PBL schemes. Furthermore, the NOAH-MP LSM produces drier atmospheric conditions than NOAH, with a difference in mixing ratio profiles ranging up to 1.4 gkg^{-1} . These variations are more pronounced in the upper CBL than close to the ground. The mixing diagrams indicate that these deviations are mainly related to entrainment fluxes. In the dry case, NOAH-MP’s dry air entrainment is up to 6 times higher than with NOAH, while in the convective case the

difference is not as pronounced (up to 1.5 higher with NOAH-MP). This suggests that the difference in the simulation of the CBL between the two LSMs is strongly linked to the surface energy partitioning – the higher the Bowen ratio, the greater the difference between the LSMs. Thus, WRF appears to be more sensitive to the choice of LSM at higher Bowen ratios. NOAH and NOAH-MP exhibit marked differences in representing atmospheric variables such as moisture. Those differences are not constrained to the lower atmosphere close to the land surface, but extended to the lower troposphere. The variations in free tropospheric moisture between the LSMs strongly affects the nature of the simulated convection, and associated precipitation. The degree of sensitivity of the spatial variability and amount of the precipitation with respect to the selection of LSM and PBL scheme shows a strong dependence on the analysed region.

A distinct finding of this thesis is the greater sensitivity of WRF with respect to the PBL development to the selection of the LSM, than to the PBL scheme. Furthermore, the impact of this sensitivity is not constrained to the lower CBL, but extends up to the interfacial layer and the lower troposphere - for both dry and convective weather conditions. On the other hand, it is clear that the simulated coupling strength between the land surface and atmosphere is very sensitive to the surface Bowen ratio.

The synergies between high resolution measurements and model simulations, with an advanced representation of the land surface processes, will facilitate not only further development of parameterization schemes, but also an improvement in our understanding of land-atmosphere interactions.

Contents

1. Introduction.....	1
1.1. The planetary boundary layer.....	2
1.2. The soil-vegetation-atmosphere system.....	3
1.3. Deep moist convection.....	6
1.4. Motivation.....	9
1.4. Aims and objectives.....	12
2. Experimental setup and methodology.....	14
2.1. The WRF model.....	14
2.2. Land surface models.....	19
2.2.1. NOAH land surface model.....	19
2.2.2. NOAH MP land surface model.....	21
2.3. Planetary Boundary Layer schemes.....	23
2.3.1. The local approach: MYJ and MYNN.....	24
2.3.2. The nonlocal approach: YSU and ACM2.....	26
3. Dry case study.....	30
3.1. Study area and weather conditions.....	30
3.2. Measurements.....	31
3.3. Methodology - the mixing diagram.....	33
3.4. Results.....	35
3.4.1. Absolute humidity profiles.....	36
a) Sensitivity to the PBL parameterizations.....	36
b) Sensitivity to the LSMs.....	38
3.4.2. Temperature profiles.....	39
3.4.3. Planetary boundary layer height.....	41
3.4.4. Land-atmosphere coupling.....	43
3.5. Discussion.....	47
3.5.1. Sensitivity to the PBL schemes.....	47

3.5.2.	Sensitivity to the LSM	50
4.	Convective case study	55
4.1.	Study area	55
4.2.	Case description	56
4.3.	Results and discussion	58
4.3.1.	Accumulated precipitation	61
4.3.2.	Clouds	65
4.3.3.	Atmospheric conditions in the lower PBL	66
4.3.4.	Vertical cross-sections	69
4.3.5.	Vertical profiles	71
4.3.6.	Land-atmosphere coupling	73
4.4.	Discussion	77
4.4.1.	Sensitivity to PBL schemes	77
4.4.2.	Sensitivity to LSMs	83
5.	General conclusions	87
6.	Outlook	94
7.	Abbreviations	97
8.	Symbols	99
9.	List of tables	102
10.	List of figures	104
11.	Bibliography	111
12.	Appendices	129
	Curriculum Vitae	133
	Declaration of Originality	136

1. Introduction

Climate change is changing not only temperature statistics and trends, but is also starting to modify the water cycle, particularly spatial and temporal patterns of precipitation. Already in recent decades it has been observed that such changes impact plant growth and consequently the evolution of agricultural landscapes. The magnitude of these impacts depends on the location, agricultural system, degree of warming and water availability (Hamilton et al., 2015). It is expected that these effects of climate change will be persistent or even intensified in the future due to climate change.

In order to increase our understanding of the evolution of agricultural landscapes under a changing climate in southern Germany, an interdisciplinary project was established - Research Unit (RU) 1695 (<https://klimawandel.uni-hohenheim.de/110767?&L=1>). The main idea of the project is to develop a land system model, capable of capturing land-atmosphere and human-environment interactions at high spatial (~ 1 km) and temporal resolution. This land system model is based on a coupled atmospheric and land surface model (LSM), further coupled to a crop model and a multi-agent model. This model chain will lead to a more realistic representation of processes at the land surface and vegetation dynamic, and we can expect an improvement of simulated feedbacks between the land surface, vegetation and the atmosphere, and consequently an improvement in climate projections. Therefore, it is vital to understand these feedbacks to advance climate modelling applications important for society, such as seasonal forecasting and climate projections (e.g. Seneviratne and Stöckli, 2008; Lenderink and van Meijgaard, 2008; Zolina et al., 2013).

Modelling and observational studies of the land-atmosphere coupling suggest that the coupling strength varies with respect to time and location (e.g. Koster et al, 2006; Guo et al., 2006; Seneviratne and Stöckli, 2008; Teuling et al., 2009). Furthermore, modelling studies such as Hohenegger et al. (2009) and Knist et al. (2016) showed that this coupling is also sensitive to model configuration and resolution.

The Weather Research and Forecasting atmospheric model (WRF; Skamarock et al. 2008) was selected as the basis of the land system model. WRF can be coupled to a selection of LSMs, whose main purpose is to compute surface water and energy balances.

It also includes multiple parameterization options for sub-grid scale processes, both at the land surface and in the atmosphere. This flexibility makes the model particularly suitable for testing and assessing parameterization schemes, over various timescales, locations and weather conditions.

As a part of the RU 1605 project, this thesis contributes to a better understanding of processes in the planetary boundary layer (PBL) and at the land surface, and also how these are represented or parameterized in the WRF model. Furthermore, the thesis explores the feedbacks between the land surface and the atmosphere, both in dry and convective weather conditions over Germany. In this section, a theoretical background on the PBL, soil-vegetation-atmosphere (SVA) system and deep moist convection (DMC) is given to provide background knowledge for the thesis. Motivating aspects are presented through state of the art research with respect to numerical modelling on regional scales. The section is closed with the thesis aims and objectives, as well as the key questions to be answered during this thesis.

1.1. The planetary boundary layer

Most of our lives we spend in the lowest portion of the atmosphere, formally known as the PBL. Located between the Earth's surface and the free troposphere, the PBL is highly sensitive to spatial and temporal changes at the surface. Over land surfaces, the PBL evolves with the diurnal cycle and has a well-defined structure within high pressure regions (Figure 1).

In the morning hours, after sunrise, the mixed layer starts to form above the surface layer (Figure 1). It is characterised by strong turbulent mixing which smoothens the gradients of moisture and potential temperature. By the afternoon the CBL is well mixed, with the moisture and potential temperature profiles almost constant. A layer above the mixed layer that separates the CBL from the free atmosphere is the interfacial layer. In this layer, the most important dynamical process is entrainment, which can be defined as the turbulent mixing of air from aloft into the CBL (e.g. Otte et al., 2001). The free atmospheric air is usually drier with higher potential temperature than the air in the CBL and, therefore entrainment tends to cause a deepening of the CBL. At sunset, due to lack of radiative heating, turbulence ceases and the CBL collapses. Just before sunset and after the CBL collapse, a residual layer forms above the nighttime stable PBL. The residual

layer has no direct interaction with the land surface and therefore is not considered as a part of the PBL, but it contains its properties and influences the PBL evolution, especially during the morning and evening transition periods (e.g. Stull, 1988; Angevine, 2008; Blay-Carreras et al., 2014).

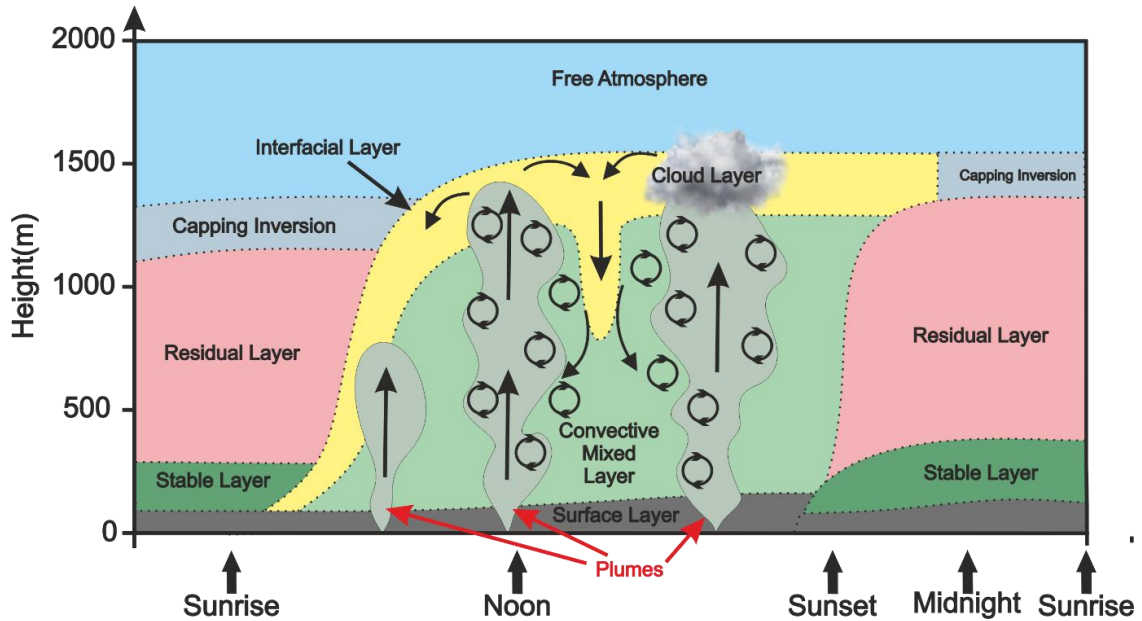


Figure 1. Schematic representation of the PBL diurnal evolution. The arrows denote the mean direction of heat and moisture transport. Circles with arrows represent turbulent eddies, which form the main mechanism of transportation in the convective PBL.

1.2. The soil-vegetation-atmosphere system

The SVA system is a very complex interacting system that consists of soil, vegetation, and the overlying atmosphere as compartments. The system is characterized by the presence of numerous feedback mechanisms between the compartments in which the incoming solar radiation (S) and the atmospheric longwave radiation (L), together with the soil and land properties determine partitioning of the total radiative energy (R_N) absorbed by the land surface (Figure 2). This is partitioned into turbulent sensible heat (H) and latent heat (λE) fluxes, which are generally directed upward from the land surface during the daytime, and which strongly impact on PBL structure. The remaining energy goes into ground heat flux (G).

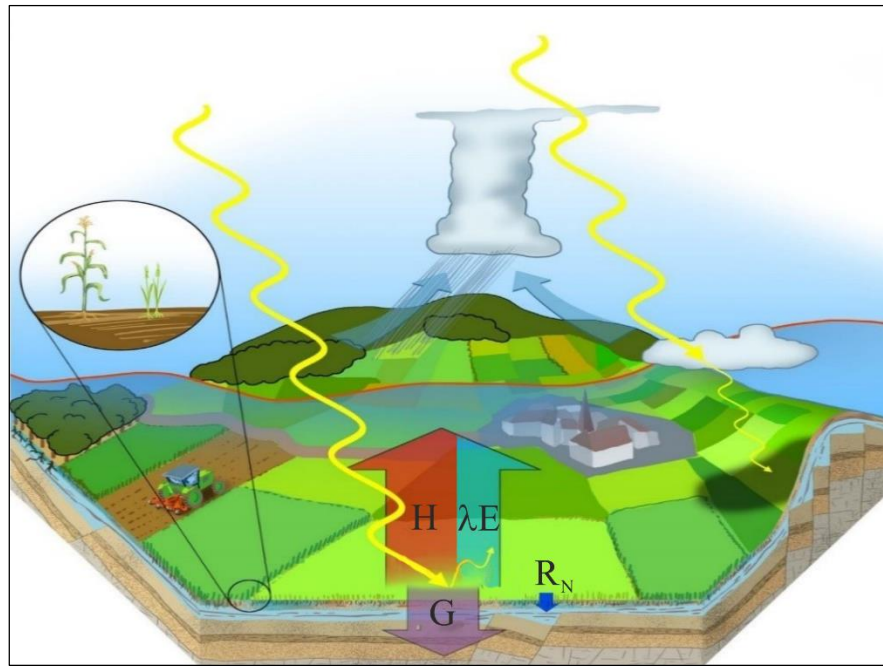


Figure 2. Schematic representation of the SVA system (Wulfmeyer et al., 2015a)

These fluxes are highly variable in both time and space. Some of these variations are caused by a location itself, since the solar radiation that impinges on the ground depends on the Sun's position in the sky. If a surface is oriented perpendicular to the Sun's rays, the direct solar radiation is at its highest. As the zenith angle between the surface and a Sun ray deviates from 90° , the Sun's radiation is spread over a larger area resulting in less radiation per unit area (e.g. Bonan, 2008). However, most of the flux variability is influenced by the land surface properties, which includes soil moisture and vegetation. This variability causes horizontal transport and convergence of heat and moisture in the PBL, and impacts on processes occurring at the PBL top. In fact, strong convergence of moisture is often a precondition for convection initiation (CI), and furthermore for precipitation occurrence (Wulfmeyer et al., 2014a), underlining the strong impact that the surface energy balance has on weather and climate (e.g. Betts, 2009).

The SVA system consists of a great variety of nonlinear interactions, composed of positive and negative feedback loops between the compartments and variables. This includes interactions between soil and vegetation properties and states, the induction and strength of mesoscale circulations, and the evolving surface energy balance. The term "feedback" refers to the fact that between most variables in the SVA system a two-way coupling exists, such as between sensible heat flux and PBL height (PBLH; van

Heerwaarden et al., 2009), or between soil moisture and precipitation (Seneviratne, 2010). A simplified example of such feedback loops are depicted in Figure 3.

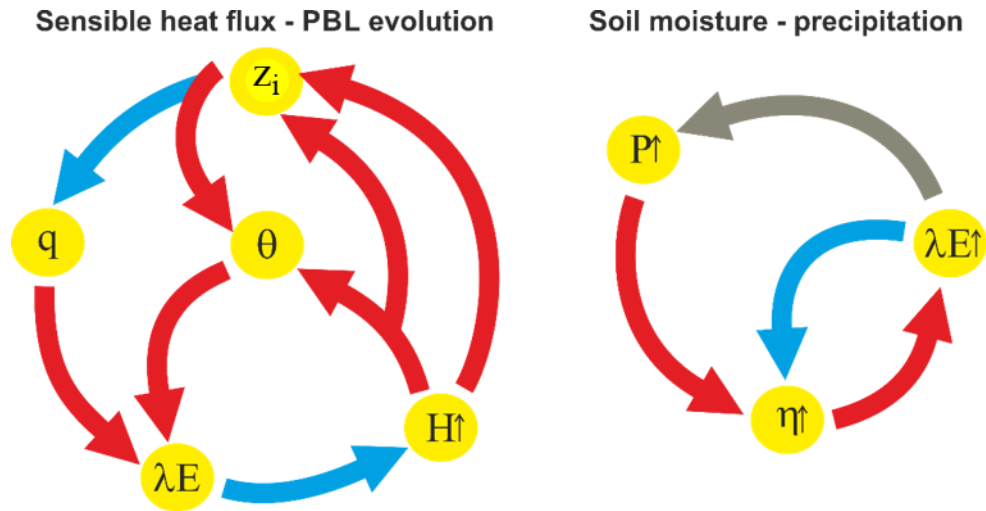


Figure 3. SVA feedback loops showing positive (red arrows) and negative (blue arrows) feedbacks of sensible heat flux (H) on PBL evolution (left), and of soil moisture η on latent heat flux (λE) and precipitation P (right). The grey arrow depicts an impact that can be both positive and negative. z_i is the PBLH, while θ and q are symbols for potential temperature and humidity, respectively. The black vertical upward arrows next to H , P , λE and η indicate an increase. Adapted from van Heerwaarden et al. (2009) and Seneviratne et al. (2010).

The left hand schematic in Figure 3 shows the impact of changing surface H on PBL evolution. An increase in surface H increases the PBL bulk potential temperature (θ) and subsequently PBLH (z_i) due to greater buoyant mixing. An increase in z_i will intensify the entrainment of warmer and drier air from the free atmosphere aloft. This will additionally increase θ and decrease q , and as a consequence, the moisture demands of the PBL will increase. This tends to increase λE at the land surface, and to decrease H . A more complicated, and still uncertain, feedback loop is between soil moisture (η) and precipitation (P), as shown in Figure 3 (right hand schematic). A clear positive feedback exists from P to η (Guillod et al., 2015), but the feedback between η and λE is less trivial, because an increase in η can have both positive and negative impacts on λE . Studies such as Koster et al. (2006), Seneviratne et al. (2006) and Teuling et al. (2009) show that the nature of this interaction depends on the climate regime and vegetation at the land surface. Significant positive feedbacks can be expected in transitional regions between wet and dry climates. In some regions, such as wet/radiation limited climates, this η - λE coupling tends to be insignificant (Seneviratne et al., 2010). The other link in this feedback chain

is the coupling between η and P , which seems to be the most complex and uncertain one in the SVA system (Findell and Eltahir, 2003a; Seneviratne et al., 2010; Gentine et al., 2013). Various studies indicate that precipitation is more likely to occur over wetter soils (e.g. Pal and Eltahir, 2001; Guo et al., 2006; Koster et al., 2006; Findell et al., 2011), whereas other studies show that more precipitation occurs over drier soils (e.g. Ek and Mahrt, 1994; Findell and Eltahir, 2003a; Ek and Holstag, 2004; Hohenegger et al., 2009; Taylor et al., 2012; Guillod et al., 2015).

The simulated interaction between all compartments and variables of the SVA system play a significant role in model performance from local to global scales, especially with respect to the representation of atmospheric temperature, humidity, clouds, circulation, and precipitation (Mahmood et al., 2013; Stéfanon et al., 2014). The SVA coupling strength in regional climate models (RCMs) is likely to be strongly dependent on model configuration (Prein et al., 2015; Knist et al., 2016). For instance, one study found that changing either the convection parameterization or model resolution, led to differences not only in the magnitude, but also in the sign of η - P coupling (Hohenegger et al., 2009). Moreover, the strength of land-atmosphere coupling varies both regionally and seasonally, and is expected to increase as the climate changes (Dirmeyer et al., 2012). Thus, relevant feedback mechanisms need to be accurately represented by RCMs, if projections of future climates are to be reliable (Prein et al., 2015), but to achieve this requires a greater understanding of the SVA system, especially its more uncertain interactions such as the coupling between soil moisture and precipitation.

1.3. Deep moist convection

Convection is a process which affects the atmosphere over various scales, ranging from local to global. It refers to an intensified vertical transport and mixing of atmospheric properties, which is often characterized by applying parcel theory. Therein, moist convection starts in a layer close to the surface, from which the parcel is lifted by a buoyant or mechanical mechanism. As an ascending parcel rises, it cools according to the dry adiabatic lapse rate. Once it reaches the lifting condensation level (LCL) the contained water vapour begins to saturate and the parcel then cools at a slower moist adiabatic rate. In favourable conditions, the parcel continues to rise and the water condenses into cloud-forming droplets. This happens within the PBL or close to the PBL

top and is referred to as shallow convection, which was mentioned in the previous section. During condensation, latent heat is released which warms the parcel. Under certain conditions, this increases the parcel's buoyancy enough to support upward acceleration of the parcel. If the displaced parcel then reaches the level of free convection (LFC) it becomes positively buoyant and continues to rise freely until the equilibrium level is reached (EL). At the EL the parcel becomes neutrally buoyant and the ascent is stalled. This process is referred to as DMC, where the parcel penetrates above 500 hPa. This may result in severe weather events such as thunderstorms accompanied with large hail and stormy winds.

One of the most difficult aspects of DMC to treat in the models is the CI, since it depends upon numerous processes, occurring from micro to synoptic scales (Trier, 2003). A precondition for DMC is atmospheric instability. A conditionally unstable layer in the atmosphere is necessary for DMC to occur – a layer where the atmospheric lapse rate lies between the dry and moist adiabatic lapse rate. This rapid cooling of the surrounding environment means that the parcel is more likely to reach the LFC and become positively buoyant.

A stable layer often exists between the surface and LFC, which is necessary for a parcel to overcome in order to become positively buoyant. This can happen also if the layer is broken down through heating, moistening or a lifting mechanism. The energy necessary to lift the parcel to its LFC through the stable layer is known as convection inhibition (CIN). On a thermodynamic diagram it represents the negative area with linear coordinates in temperature and logarithmic coordinates in pressure, which can be calculated as buoyancy (B) integrated over an area between the surface (sfc) and the LFC following the equation

$$CIN = - \int_{sfc}^{LFC} B dz = g \int_{sfc}^{LFC} \frac{\theta_v'}{\overline{\theta_v}} \quad (1)$$

B is related to the virtual potential temperature perturbation θ_v' relative to the environmental virtual potential temperature $\overline{\theta_v}$ and multiplied by the gravitational acceleration g . When DMC occurs, a useful measure for its intensity is the convective potential energy (CAPE) that represents the vertically integrated positive buoyancy between LFC and EL, and can be calculated following the equation

$$CAPE = \int_{LFC}^{EL} B dz = g \int_{LFC}^{EL} \frac{\theta_v'}{\theta_v} \quad (2)$$

CAPE is a potential energy available for the parcel to ascent above the LFC, and represents a necessary but not sufficient condition for CI. Likelihood for DMC to occur is higher when CIN is low enough to allow sufficient CAPE to be released. CIN is considered small when $< 10 \text{ Jkg}^{-1}$ and high when $> 50 \text{ Jkg}^{-1}$, while high CAPE is $> 2500 \text{ Jkg}^{-1}$ and small values are $< 1000 \text{ Jkg}^{-1}$ (Branch, 2014).

Phenomena which tend to reduce CIN, and allow CAPE to be released, occur over varying scales. In absent or weak synoptic forcing, CI is mostly controlled by processes at the land surface and in the PBL. One process is differential heating at the land surface, caused by inhomogeneities and variations in soil moisture. For instance, wet surfaces in clear-sky weather conditions allows for a larger λE from the land surface. This tends to increase PBL humidity and consequently enhances CAPE and probability for DMC to occur, although the complex feedbacks from TM^3 still apply. It is necessary to mention that DMC occurrence over wet or dry soils strongly depends on the strength of the inversion layer at the PBL top (CIN), and on the free atmospheric stratification aloft (Khodayar, 2009; Gentine et al., 2013). Therefore in cases where a strong inversion layer exists, the likelihood of DMC occurring is greater over dry than over wet surfaces. In the case of dry soils, even though lower λE occurs, a higher H will lead to stronger mixing in the PBL which can erode the strong capping inversion (CIN), and initiate DMC more easily. The coupling between the land surface and moist convection is likely to be insignificant only when (1) the atmosphere is too dry or stable, which would tend to suppress DMC altogether, or (2) the atmosphere is very moist and unstable, because convection is very likely to occur over any surface in any case (Findell and Eltahir, 2003).

The time of CI onset is sensitive to the characteristics of the residual layer and the depth of the nocturnal boundary layer (Ek and Mahrt, 1994; Findell and Eltahir, 2003a). For CI, it is necessary for the nocturnal boundary layer to diminish and that the CBL overtakes the residual layer. Only then can the CBL thermals reach the LCL. Whether clouds will form or not depends on the inversion depth, as mentioned before, and on the amount of low level moisture. Entrainment processes at the PBL top reduce the potential for DMC since typically drier and warmer air from the free troposphere aloft is entrained into the PBL. Nevertheless, if there is sufficient moisture in the PBL, moist convection can still

be initiated. Thus, conditions for CI are highly sensitive to temporal and spatial moisture inhomogeneities within the PBL (Khodayar, 2009, Wulfmeyer et al., 2014a).

Differential heating due to spatial inhomogeneities of the Earth's surface may induce local convergence zones along which local lifting and convection triggering may occur without the need for an additional lifting mechanism. These inhomogeneities include effects of orography, land/water boundaries, and variations in land cover and soil moisture, which strongly regulate the surface fluxes and consequently the PBL evolution. The variation in surface fluxes may cause temperature and moisture inhomogeneities in the PBL, form the convergence zones and induce upward motions, during which enough CAPE can be released and convection initiated (Khodayar, 2009, Wulfmeyer et al., 2014a).

1.4. Motivation

High resolution climate scenarios for various regions have been provided via integration of multiple RCM simulations (Kotlarski et al., 2014). However, still to date, regional projections of climate change exhibit high variability and significant biases, especially with respect to precipitation (Warrach-Sagi et al., 2013; Kotlarski et al., 2014). This is partly related to incorrect boundary conditions of the global models (e.g. Bruyère et al., 2013; Kotlarski et al., 2014), as well as to shortcomings of the model physics (e.g. Prein et al., 2015).

Therefore, to advance the accuracy of RCMs, it is necessary to improve the model representation of atmospheric processes such as convection and turbulent mixing. The vertical and horizontal resolutions of RCMs (typically > 10 km) are too coarse to resolve these processes explicitly, and therefore such models require parameterization strategies, a method of replacing such complex and small-scale phenomena with simplified representations. However, parameterization schemes can vary substantially both in their approach and/or in complexity. Such schemes very often include numerous assumptions, which give rise to uncertainties within a model simulation. Therefore, to understand the model performance and to recognise those uncertainties, it is of great importance to understand how the physics schemes operate within the model.

One of the most critical sub-grid schemes used in RCMs is the parameterization of deep convection. It is commonly thought that a decrease in model grid increment to convection permitting (CP) scale (< 4 km) will lead to more accurate results and a reduction in biases (e.g. Kotlarski et al., 2014). Results from some recent studies such as e.g. Hohenegger et al. (2009), Bauer et al. (2011), Kendon et al. (2012), Warrach-Sagi et al. (2013) support this hypothesis. These improvements are likely to be primarily due to the explicit handling of deep convection, and also on the improved representation of orography and land surface structure. Furthermore, an increase in model resolution down to ~ 1 -4 km requires an adaptation of certain schemes, because certain parameterizations that work well on coarser scales might be unsuitable at CP resolutions. This is particularly true for turbulent parameterization schemes (e.g. Kleczek et al., 2014; Cohen et al., 2015; Prein et al., 2015; Milovac et al., 2016).

The processes in the SVA system are mostly small-scale phenomena, which can influence larger scale circulations (e.g. Tribbia and Baumhefer 2004). Representation of these relations in the models are therefore a key factor affecting accuracy. Various research strategies have been proposed to accurately represent the water and energy exchange processes between the soil, vegetation and atmosphere (e.g. Ek and Holtslag, 2004; Seneviratne et al., 2010; Santanello et al., 2013). Particularly important is the consideration of the structural evolution of the PBL, humidity profiles, moisture advection, mesoscale circulations, CI (Sherwood et al., 2010), as well as the formation of clouds and precipitation.

In models such as WRF, representation of CI and precipitation are influenced by the land surface through the PBL schemes, which parameterize the turbulent transport of heat, moisture and momentum in the atmosphere. The lower boundary conditions for the PBL schemes are the surface turbulent fluxes, simulated by the LSM. Thus a strong linkage exists between the PBL schemes and LSMs. Many studies have been focused on WRF sensitivity to PBL schemes (e.g. Hu et al., 2010, 2013; Shin and Hong, 2011; Xie et al., 2012, 2013; Coniglio et al., 2013; García-Díez et al., 2013). On the other hand, there are not so many studies that have been investigated the model sensitivity to LSMs, especially with respect to representation of SVA feedback processes. Misenis and Zhang (2010) in their 5-day simulations found that WRF is more sensitive to the selection of LSM than to the PBL schemes, for standard meteorological predictions (i.e. 2 m temperature, 2 m relative humidity, wind speed and wind direction). This was primarily due to large

differences in simulated surface fluxes in the three LSMs used in the study. In their comprehensive analysis of WRF's sensitivity on CP scale to LSM, microphysics, radiation and PBL parameterizations over the Iberian Peninsula, Borge et al. (2008) showed that the model representation of the PBLH and the PBL evolution is particularly influenced by the LSMs and PBL schemes. Therefore, by investigating the LSM-PBL parameterization linkage in WRF could lead to a better understanding of accuracy and variability in results, and SVA processes.

The main issue impeding progress in investigating and understanding feedback processes between the land surface and the atmosphere is a lack of observations - crucial for such studies. Available measurements of key variables such as soil moisture and evapotranspiration lack spatial and temporal continuity (e.g. Seneviratne and Stöckli, 2008; Findell and Eltahir, 2003a). Furthermore, measurements should not be constrained to the ground since land surface fluxes and PBL water vapour both interact with entrainment fluxes. The lack of high-resolution temperature and water-vapour profiling, which are a prerequisite to improve our understanding of SVA feedback loops and PBL processes, is currently a strong weakness within observing systems (Wulfmeyer et al., 2015a). In the past, entrainment fluxes have been measured mainly in-situ by aircrafts (Lenschow et al., 1994), which is a rather expensive method. Another method is turbulence profiling with ground-based lidar systems such as Doppler lidar (DL) for wind measurements, temperature rotational Raman lidar (TRRL) (Radlach et al., 2008), and either differential absorption lidar (WVDIAL; Wagner et al., 2013) or Raman lidar for water-vapour (Turner et al., 2002). These lidar systems are capable of profiling higher-order turbulent moments of vertical wind and turbulent kinetic energy (TKE) dissipation rate (e.g., Wulfmeyer and Janjić, 2005; Ansmann et al., 2010; Lenschow et al., 2012), temperature (Behrendt et al., 2013) and water vapour (e.g. Wulfmeyer, 1999a; Wulfmeyer et al., 2010; Muppa et al., 2016) in the CBL. Furthermore, combinations of these remote sensing systems are applied for profiling of the latent heat flux, as well as stability indices (Wulfmeyer, 1999b, Corsmeier et al., 2011). The combination of 3D scanning WVDIAL and TRRL has the potential to measure fields of surface and entrainment fluxes simultaneously by the application of sophisticated scan strategies (Wulfmeyer et al., 2015a). High-resolution scans in the surface layer allow for studying the two-dimensional structure of the fluxes through the application of the Monin-Obukhov (MO) similarity theory (Cooper et al., 2007; Wulfmeyer et al., 2014b). In

Germany, a corresponding synergy of scanning lidar systems was deployed during field campaigns such as COPS in summer 2007 (Wulfmeyer et al., 2008; Wulfmeyer et al., 2011; Behrendt et al., 2013), the TransRegio (TR) 32 (Simmer et al., 2015) FLUXPAT campaign in autumn 2009 (Behrendt et al., 2009), the High Definition Clouds and Precipitation [HD(CP)²] Observational Prototype Experiment (HOPE) in spring 2013 (Hammann et al. 2015), and the Surface Atmosphere Boundary Layer Exchange (SABLE) campaign (Wulfmeyer et al., 2015b). The high resolution data sets collected during these campaigns represent a valuable tool for detailed studies of convection and PBL evolution. There is also potential to develop new strategies for model validation and for investigation of sub-grid parameterizations relating to SVA feedbacks and turbulent fluxes.

1.4. Aims and objectives

One of the objectives of the first phase of the RU 1695 P1 project was to develop and verify a WRF-RCM on the CP scale including an advanced representation of SVA feedback processes, prior to supplementing it by a crop and a multi-agent model, with the emphasis on water and energy cycling between the land surface and the atmosphere. For that, it is necessary to assess WRF's representation of CBL processes, especially when different combinations of PBL and LSM parameterization schemes are used. By doing this in synergy with unique profile measurements, the knowledge of key physical processes in the SVA system can be greatly improved, and potential areas for improvement within parameterization schemes and possible solutions can be identified.

In order to achieve these aims, an extensive investigation is conducted using WRF. The model representation of land-surface and PBL processes and feedbacks has been accessed under dry and convective weather conditions to investigate the model sensitivity to different parameterizations. For that, an ensemble of six simulations using various combinations of land surface and PBL model physics schemes has been set up. From these simulations, two case studies are examined – a dry and a convective case – with unique comparisons of humidity profiles against high resolution profile measurements with the WVDIAL. At the same time, the simulated coupling between land surface and the atmosphere is analysed and quantified, and the sensitivity of key processes to model physics within WRF is investigated, in respect to SVA feedbacks.

Five questions are used to summarise the aims of this thesis, and provide a basis for later conclusions:

- 1) How sensitive are the CP WRF simulations of PBL processes and DMC to the PBL parameterization in temperate climate conditions?
- 2) To what extent do LSM physics influence simulated atmospheric processes, especially PBL evolution, entrainment, convection and precipitation?
- 3) What coupling effects exist between the land surface and PBL model physics and are they dependent on location and weather conditions?
- 4) To what extent the WVDIAL measurements can be used for the assessment of actual and modelled PBL evolution at the CP scale?
- 5) What LSMs and PBL parameterizations show the most promising results at the CP scale?

The dissertation is structured as follows. Descriptions of the WRF model chain and physics schemes are presented in section 2. In section 3, the dry case study is introduced, and the results given and discussed, followed by the convective case study in section 4. Finally, general conclusions and an outlook are given in sections 5 and 6.

2. Experimental setup and methodology

An ensemble consisting of 6 simulations for the sensitivity studies represented in this thesis have been executed with the WRF model. The simulations differed in selected PBL scheme and LSM. Basics about the WRF model and the differences among each of the simulations are given in the following subsection. In the last two subsections the selected LSMs and PBL schemes are introduced, with special emphasis on the differences among them.

2.1. The WRF model

WRF is a numerical atmospheric model based on Euler nonhydrostatic equations, which are fully compressible and conservative for scalar variables (Skamarock et al. 2008). Equations are solved numerically with the least-squares method on the Arakawa C staggered grid. The vertical coordinate is a terrain-following, dry hydrostatic-pressure coordinate with the top of the model at constant pressure surface (Skamarock et al. 2008). WRF can be applied over different scales ranging from global circulation (e.g. Zhang et al., 2012) down to large-eddy simulations (LES; e.g. Talbot et al., 2012), where the main energy-producing scales of 3D atmospheric turbulence are resolved explicitly on the computational grid. Primarily, the model has been used for NWP and climate simulations, with the horizontal resolution ranging from 1 to 50 km (e.g. Mirocha et al., 2014; Milovac et al., 2016).

WRF includes a selection of physics parameterization schemes for longwave and shortwave radiation, surface-layer, PBL and microphysics, and is coupled with a chosen LSM which can vary in complexity. In case of non-convection-permitting simulations where the horizontal grid spacing exceeds 4 km and deep convection processes are not resolved explicitly by the model, several choices of convection parameterizations are available. They were developed and applied as stand-alone models (forced e.g. with weather data) or coupled to hydrologic and atmospheric models. Coupled with WRF, a LSM interacts directly and indirectly with all the other WRF parameterization schemes. Water and energy fluxes calculated in a LSM are provided to a PBL parameterization scheme as lower boundary conditions, usually through a surface layer scheme. The PBL scheme calculates the sub-grid scale vertical turbulent fluxes in the whole atmospheric

column, i.e. it is not limited only to the PBL. Atmospheric tendencies of temperature, moisture with clouds, and horizontal momentum are obtained from the PBL scheme directly.

Strongest SVA feedbacks such as between soil moisture and precipitation may be expected in regions where atmosphere is not as dry as in desert areas, or as moist as in areas with tropical climate conditions (Findell and Eltahir, 2003a, Koster et al., 2006, Guillod et al., 2015). Therefore temperate climate conditions are favourable for so called transitional regions which are marked as areas where feedback of the soil moisture state on the atmospheric processes exists (Findell and Eltahir, 2003b; Knist et al., 2016). To investigate SVA feedbacks for this work, the study area is located in Europe, centred in Germany, where climate conditions are characterised as temperate and maritime, with greater seasonal variations in temperature which result in moderate warm summers and cold wet winters. Central and southern part of the country is in a transitional region having both maritime and continental influences. According to the aforementioned, the model domain was chosen to cover most of central and south Germany (Figure 4).

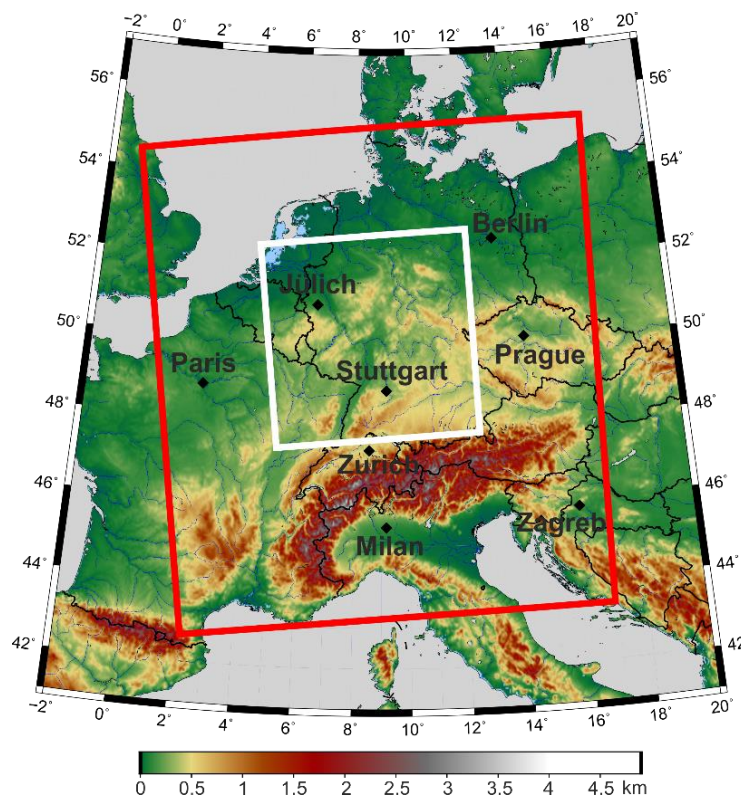


Figure 4. The outer within the red boundaries and the inner domain in the white boundaries for the WRF simulations along with the orography field (in m ASL).

All simulations were carried out with the WRF model version 3.5.1. The resolution of the inner domain was set to 2 km (Figure 4). The outer domain, with 6-km resolution, was chosen as an intermediate step to downscale the coarse European Centre for Medium Range Weather Forecasts (ECMWF) operational analyses data (on a 0.125 x 0.125 degree grid). It incorporates the whole of Germany and the impact of elevated ranges in the closest neighbouring areas. The mountain range of Alps and the Massif Central in southern France were included in order to capture the major synoptic forcing that influences the local weather in western and south-western Germany. The inner domain with 270 x 270 grid cells was nested into this domain covering most of Germany. The model simulations were performed on a vertical grid consisting of 89 full pressure levels, with 20 levels within the first 2200 m, and the lowest σ level set to ~ 5 m.

The WRF model was set up with the following physics parameterizations: Morrison 2 moment scheme (Morrison et al., 2005) for microphysics and the rapid radiative transfer model for global circulation models (RRTMG) for both the longwave and shortwave radiation. The Kain-Fritsch scheme (Kain, 2004) was selected for convection parameterization in the outer domain.

Table 1. The WRF experiments with the selected PBL schemes, surface layer schemes, and LSMs.

Experiment	PBL scheme	Surface layer scheme	LSM
ACM2	ACM2	Revised MM5	NOAH
MYJ	MYJ	Eta similarity	NOAH
MYNN	MYNN 2.5	Revised MM5	NOAH
YSU	YSU	Revised MM5	NOAH
MYNN-MP	MYNN 2.5	Revised MM5	NOAH-MP
YSU-MP	YSU	Revised MM5	NOAH-MP

With this configuration, a total of six numerical experiments were conducted with the Asymmetric Convective Model version 2 (ACM2; Pleim, 2007), Mellor-Yamada-Janjić (MYJ; Mellor and Yamada, 1982; Janjić, 2002), Mellor-Yamada-Nakanishi-Niino (MYNN; Nakanishi and Niino, 2009) and Yonsei University (YSU; Hong et al., 2006) PBL schemes, in combination with the NOAH and NOAH-MP LSMs (Table 1). The LSMs and PBL schemes are introduced in sections 2.1.1 and 2.1.2, respectively.

MYNN and ACM2 have the possibility to run with multiple surface layer parameterizations. In order to minimize the impact of the surface layer parameterization in this sensitivity study, the revised MM5 scheme (Jiménez et al., 2012) was selected in the model runs with MYNN, ACM2 and YSU PBL. This was not possible for the simulations with MYJ, since the choice of the surface layer scheme is constrained to the Eta similarity scheme only, when running the model with MYJ (e.g. Janjić, 2002).

The land cover map in the WRF model is based on data from the Moderate Resolution Imaging Spectroradiometer (MODIS), and they are classified according to the International Geosphere-Biosphere Programme (IGSP) land cover classification, in 1 km data resolution. The original soil texture data in WRF, which is at the 5' resolution for Europe, is too coarse for studying SVA feedbacks on CP scales (Warrach-Sagi et al., 2008; Sanchez et al., 2009; Guillod et al., 2013), therefore it was replaced with new 1-km soil texture maps for Europe (Milovac et al., 2014a) based on the Harmonized World Soil Database (HWSD), and for Germany based on the German Soil Overview Map (BÜK 1000; Milovac et al., 2014b).

Since 2007 the ECMWF model is coupled to the hydrologically extended multi-level LSM HTESSEL, which results in a more realistic representation of the soil state than with the previous TESSEL LSM (Balsamo et al., 2009). The ECMWF operational analysis fields on a 0.125 x 0.125 degree grid are available on 6 hourly basis. Tests of initialization and operation of WRF with ECMWF operational analyses (ECMWF-analysis) of soil moisture and temperature fields showed that NOAH and NOAH-MP can spin up within a few weeks for this temperate climate region. Further, the deep soil is weakly coupled to the land surface and therefore its state does not contribute as much to the PBL evolution in short-term simulations (e.g. Angevine et al., 2014). Therefore, in order to get an equilibrated land surface state, the soil spin up run was set to run from 1 June 2009 to 21 August 2009 (Figure 5), with the soil moisture and soil temperature initialized with ECMWF-analysis data obtained from ECMWF Data Server. The initialization was done once at the start of the soil spin up run, on 1 June 2009 at 0 UTC.

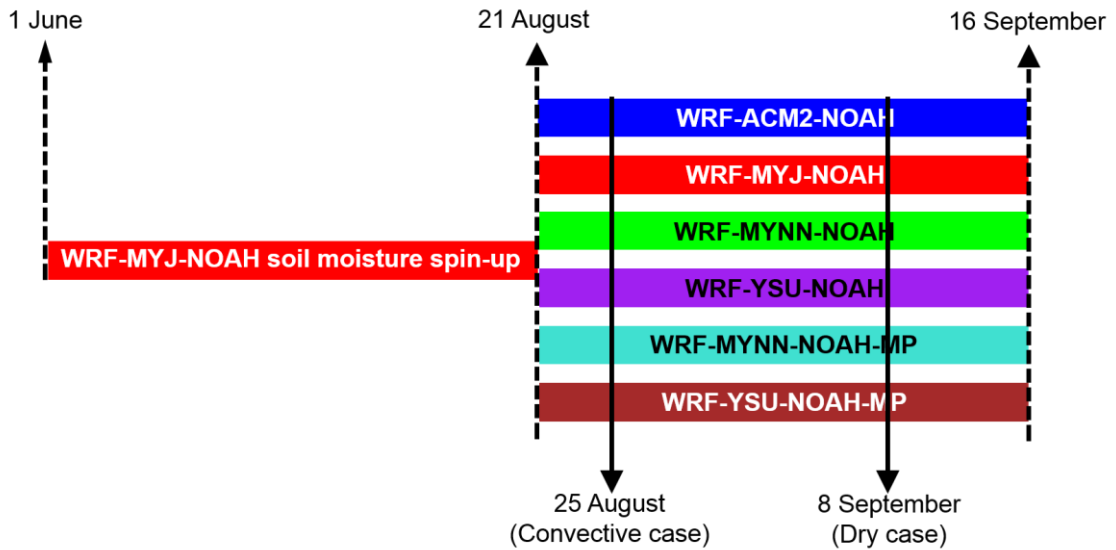


Figure 5. Schematic representation of the preformed WRF simulations in the corresponding time frames, with denoted dates of the case studies.

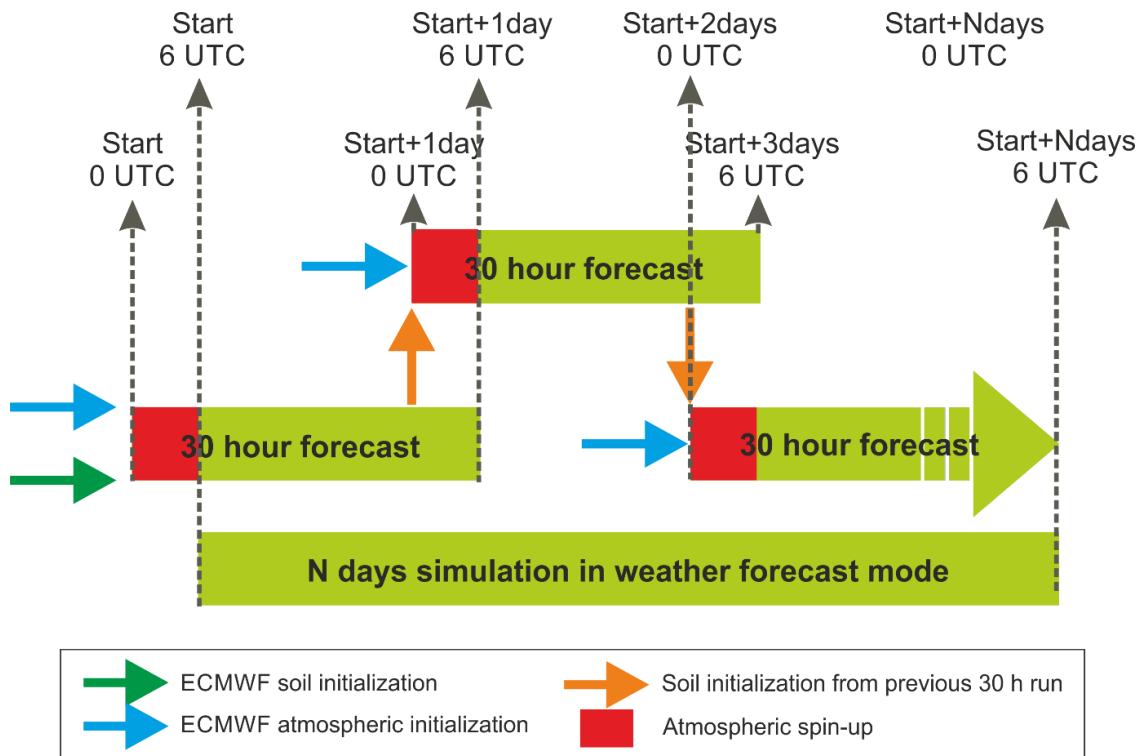


Figure 6. Schematic representation of the “weather forecast mode”. Start denotes the start date and N is the number of simulated days.

All experimental simulations started on 21 August 2009 at 0 UTC and were set to run in cycles of 30 hours in so called “weather forecast mode” (e.g. Williams et al., 2013). Each successive cycle started every next day from 0 UTC. At the start of each cycle, atmospheric conditions, as well as the lateral boundary conditions for the outer domain (6 km) were initialized by the ECMWF-analysis as well. The first 6 hours from the each cycle run were discarded from the analysis due to the atmospheric spin up. The soil moisture and soil temperature were once initialized from the soil spin up run on 21 August 2009, and then evolved freely. The principle of “weather forecast mode” is demonstrated in Figure 6.

2.2. Land surface models

Among the selection of four LSMs available in WRF, two LSMs coupled with WRF are analysed in this study: the extensively used NOAH (Chen and Dudhia, 2001a, 2001b), and the more sophisticated and more recent NOAH-MP (Niu et al., 2011). Short descriptions of the schemes in order to highlight the major discrepancies, are given in the next two subsections.

2.2.1. NOAH land surface model

The NOAH LSM (Chen and Dudhia, 2001a, 2001b; Ek et al., 2003) is a single column model with four soil layers of thicknesses of 0.1, 0.3, 0.6 and 1 m, a fractional vegetation, and a snow layer. A diffusive form of the vertical Richard’s equation for soil moisture and the thermal diffusion equation are used calculating soil moisture and soil temperature within a soil column for both unfrozen and frozen soils. The fluxes and the skin temperature at the land surface are derived by solving the energy balance closure formulated as,

$$(1 - \alpha)SW \downarrow + LW \downarrow - LW \uparrow = R_n = H + \lambda E + G \quad (3)$$

with α being the surface albedo, SW and LW are shortwave and longwave net radiations, respectively. The arrows $\downarrow \uparrow$ stand for downward and upward, R_n is the net surface radiation flux, H the sensible heat flux, λE the latent heat flux (the latent heat of vaporization λ multiplied with the actual evapotranspiration E), and G is the ground heat flux. A significant role in computing the energy fluxes and closing the energy balance in

Eq. (3) has the surface skin temperature (T_{skin}). The calculation of T_{skin} in NOAH is determined by using a single linearized surface energy balance equation over the combined ground/vegetated surface following Mahrt and Ek (1984). The fluxes are calculated separately over the vegetation canopy and the bare ground. Therefore, the net flux is a sum of the fluxes over the canopy and bare ground, weighted by the vegetation fraction (F_{veg}).

H is calculated as follows,

$$H = \rho C_p C_h u (T_{skin} - T) \quad (4)$$

where ρ is air density, C_p is specific heat capacity of moist air, C_h the surface exchange coefficient for heat, and u is the wind speed at the reference height. G is related to the temperature gradient between the surface skin (denoted as skin) and midpoint of the first soil layer (denoted as s1) written as,

$$G = K_h(\eta) \frac{T_{skin} - T_{s1}}{\Delta z} \quad (5)$$

with κ_h being the thermal conductivity, η soil moisture fraction, T_{s1} the temperature at the midpoint of the first soil layer, and dz is the soil thickness between the levels skin and $s1$. The calculation of λE is based on the potential evapotranspiration (E_p). The calculation of E_p follows the Penman-based energy balance approach based on Mahrt and Ek (1984) which includes a stability-dependent aerodynamic resistance formulated as,

$$\lambda E_p = \frac{\Delta(R_n - G) + \rho \lambda C_q u (q_{sat} - q)}{1 + \Delta} \quad (6)$$

wherein Δ is the saturated vapour pressure curve, C_q is the exchange coefficient for moisture (which is assumed to be equal to that of heat, C_h), q_{sat} and q are the saturated and specific humidity, respectively. The actual evapotranspiration is calculated as the sum of direct evaporation from the bare soil surface, evaporation of water intercepted by vegetation cover, and transpiration of plants. All the three variables are a function of the λE_p . The key controlling variable for the canopy transpiration is the stomatal resistance (e.g. van der Velde et al., 2009; Ingwersen et al., 2011; Branch et al., 2014), which is calculated using a Jarvis-type formulation (Jarvis, 1976). The Jarvis approach is dependent on meteorological parameters such as radiation, humidity and temperature.

2.2.2. *NOAH MP land surface model*

Since WRF version 3.4 released in 2012, a new NOAH-MP LSM can be coupled with WRF. NOAH-MP is an extended version of NOAH, with an internal suite of physics parameterizations and a modified energy balance (Niu et al., 2011, Yang et al., 2011). The switchable physical parameterizations include a separated vegetation canopy, dynamic leaf phenology, radiation transfer through the vegetation canopy, the multilayer snowpack topography based runoff, as well as groundwater table calculations. In addition, alongside the Jarvis scheme for stomatal resistance included with NOAH, NOAH-MP offers the Ball-Berry scheme (Ball and Berry, 1987), an approach which links stomatal resistance to leaf photosynthesis.

NOAH-MP applies an advanced method to calculate the energy balance at the land surface, Eq. (3). To represent the surface heterogeneity, NOAH-MP uses the “semi-tile” sub-grid method, and is one of the major advances compared to the “tile” approach deployed in NOAH. In the “semi-tile” approach, shortwave radiation is computed over an entire grid cell, considering gaps between the canopy to compute fractions of sunlit and shaded leaves and their absorbed solar radiation. Net longwave radiation and surface turbulent fluxes are calculated separately over a vegetated and bare soil as in the “tile” approach. This “semi-tile” approach is designed to avoid overlapping of too many shadows whenever the vegetation is present and the sun is not overhead, which occurs with the conventional “tile” approach used in NOAH (Niu et al., 2011). Also there is a modification in the “tile” approach used in NOAH-MP. Different to NOAH, the fluxes over the vegetated tile are calculated not only over the canopy, but also within the canopy (i.e. between the ground and the canopy top). Therefore, the net atmospheric exchange from a whole vegetated grid cell is a weighted sum of all the canopy fluxes (above and underneath the canopy), and the fluxes from the bare ground. Furthermore, the simple linearized method for solving the energy balance in NOAH is replaced with an iterative method in NOAH-MP. The iteration is used to solve the unknown skin temperatures within each tile, and the accordingly the fluxes are updated in each iteration step. The iteration process is stopped when the energy balance is achieved, or when the number of iterations reaches some prescribed value (e.g. Nielson et al., 2013).

There is also a structural difference in the communication chain between the LSM, and the surface layer PBL schemes, when WRF is coupled with NOAH-MP (WRF-NOAH-

MP) and not with NOAH (WRF-NOAH). In WRF-NOAH the exchange coefficients for momentum (C_m) and the scalar variables (C_h, C_q) are calculated within the surface layer scheme, whilst in WRF-NOAH-MP there is no direct information exchange between NOAH-MP and the surface layer scheme over land surfaces. This means that in WRF-NOAH-MP over land surfaces the calculation of the surface exchange coefficients and the corresponding surface layer diagnostics (i.e. 2 m temperature and humidity, 10 m wind) are calculated directly in NOAH-MP, while the coupled surface layer scheme operates only over water-surfaces (e.g. Nielsen et al., 2013).

Table 2. Complete configuration of NOAH-MP as deployed in this study.

NOAH-MP OPTIONS	CHOSEN OPTION	SHORT DESCRIPTION
Dynamic vegetation model (dveg)	Off	Leaf area index (LAI) from table; vegetation fraction (FVEG) calculated
Stomatal resistance (SR) (opt_crs)	Ball-Berry scheme	Accounts for photosynthesis
Surface layer drag coefficient (opt_sfc)	Original Noah	Version used in Noah (Chen et al., 1997)
Soil moisture factor for SR (opt_btr)	Community Land Model (CLM)	A function of the matric potential
Runoff and groundwater (opt_run)	Original surface and subsurface runoff	Free drainage
Supercooled liquid water (opt_frz)	No iteration	General form of the freezing-point depression equation
Soil permeability (opt_inf)	Non-linear effect, less permeable	Uses only the liquid water volume to calculate hydraulic properties
Radiative transfer (opt_rad)	Modified two-stream	Probability of gap between canopy equals to (1-FVEG)
Ground surface albedo (opt_alb)	Biosphere – Atmosphere Transfer Scheme (BATS)	Snow albedo accounts for fresh snow, snow age, grain size growth, etc.
Precipitation – snow or rain (opt_snf)	Snow when surface temperature (T_{sfc}) < freezing temperature (T_{frz})	When $T_{sfc} < T_{frz}$ snow, otherwise rainfall.
Soil temp. lower boundary condition (opt_tbot)	Bottom temperature (T_{bot}) at 8m from input file	Read T_{bot} at Z_{bot} from wrfinput file
Snow/soil temp. time scheme (opt_stc)	Fully-implicit	Same as used in Noah

NOAH-MP coupled to WRF 3.5.1 offers 12 additional options for key land-atmosphere interaction processes, such as options for surface water infiltration and runoff, and groundwater transfer and storage including water table depth to an unconfined aquifer. Horizontal and vertical vegetation density can be prescribed or predicted using prognostic photosynthesis and dynamic vegetation models that allocate carbon to vegetation (leaf,

stem, wood and root) and soil carbon pools (Niu et al. 2011). Table 2 lists the selected settings for NOAH-MP applied for this case study.

Aside from calculation of the energy balance closure and the semi-tile approach, major difference between NOAH-MP and NOAH relates to the Ball-Berry-photosynthesis. Furthermore, the bottom temperature at 8 m from the input file is used as the soil temperature lower boundary condition, and snow/soil temperature time scheme is chosen to be the fully-implicit. Rather than applying the NOAH-MP default setting, switches related to calculation of surface layer drag coefficients, runoff and ground water, and surface albedo have been selected to suit the study area according to offline NOAH-MP experiments applied for Germany (Warrach-Sagi 2013, personal communication; Gayler et al., 2014; Ingwersen et al., 2015;). Furthermore, test simulations were performed prior to the simulations for this study. All available options for calculation of soil moisture factor for stomatal resistance (2 options) and dynamic vegetation model (4 options) were tested. The simulations were compared with measurements of meteorological variables and radiosonde vertical profiles in SW Germany, as well as with NOAH simulations. The tests showed that the WRF model was numerically stable with the soil moisture factor based on the Community Land Model (CLM), which was not the case with the model configured with the other Noah based option. Dynamic vegetation model was set to be switched off since the simulations in this study were run for the short-term period (less than a month) in which strong variations in vegetation dynamics are not expected, and the option in which vegetation fraction (FVEG) was calculated showed better agreement with the available measurements in the test simulations (plots not shown, beyond the scope of this thesis).

2.3. Planetary Boundary Layer schemes

Variety of techniques are used for parameterization of turbulent processes in the PBL in the NWP models and RCMs. The two most important characteristics by which the PBL schemes can be categorised are the order of the turbulence closure and whether local or nonlocal approach is deployed (e.g. Cohen et al., 2015). The system of equations used to represent the turbulent mixing consists of equation of motion, thermodynamic and continuity equations, in which all the variables are decomposed into mean and perturbed components. The perturbations represent turbulent moments from the mean state, and

they are unknowns of the system. The number of the unknown terms in the system is always higher than the number of known terms. Consequently, a closure technique in which each unknown term is empirically related to the known terms needs to be applied. The order of closure is related to the order of the turbulent moment that are parameterized. For example, if, for example, the N^{th} moments are parameterized, the scheme uses the $(N-1)^{\text{th}}$ order closure technique. The order of closure technique may be also a non-integer value. For example, 1.5 order closure technique denotes that an additional prognostic equation for some, but not all second order moments in the turbulent system of equations is applied. In this closure technique, certain third order moments and remaining unknown second order moments are parameterized. The local and nonlocal approaches differ in the depth over which these turbulent moments affect variables at a specified height in the PBL. If the impact of only from adjacent levels is considered, this refers to the local approach. The nonlocal approach accounts for the impact from multiple levels within the PBL, and includes the mixing of the largest eddies which may extend from the land surface to the PBL top.

The WRF simulations analysed in this study are configured with two local schemes that use the 1.5 order closure technique, one nonlocal scheme with the first order technique and one nonlocal scheme that combines also the local approach. Short description of these 4 schemes is given in the following 2 subsections.

2.3.1. *The local approach: MYJ and MYNN*

MYJ and MYNN are the 1.5 order parameterization schemes, which means that they use an additional prognostic equation to calculate wind variances. In these schemes, the second order equation for TKE is used, which is given by

$$\frac{\partial TKE}{\partial t} = \frac{\partial}{\partial z} \left[\overline{w' \left(TKE + \frac{p}{p_0} \right)} \right] - \overline{u'w'} \frac{\partial \bar{u}}{\partial z} - \overline{v'w'} \frac{\partial \bar{v}}{\partial z} - \frac{g}{\theta_0} \overline{w'\theta'_v} - \varepsilon, \quad (7)$$

where p is pressure, p_0 is the surface pressure, θ_v is the virtual potential temperature, and ε is the dissipation rate of TKE. The other second order turbulent moments are diagnosed by applying the mixing length theory proposed by Prandtl (Prandtl, 1942).

Both schemes use the Mellor-Yamada scheme (Mellor and Yamada, 1982) as their baseline. MYNN treats consistently condensation physics in the PBL by including liquid-

water potential temperature and total water content as prognostic thermodynamic variables and allowing for partial condensation in a model grid to assure proper interaction with microphysics and radiation (Nakanishi and Niino, 2009).

Both aforementioned schemes relate the turbulent fluxes of any adiabatically conserved quantity to gradients of their mean values at adjacent levels only (i.e. local approach) as

$$\overline{w'\psi'} = -K_\psi \frac{\partial \bar{\psi}}{\partial z} \quad (8)$$

where w' represents the vertical velocity fluctuation, ψ' is the fluctuation of an adiabatically conserved variable (momentum m , heat h or moisture q). The overbars denote averaged values. $K_\psi (\equiv l S_\psi \sqrt{2TKE})$ is the eddy diffusivity specified as a function of TKE , a stability function S_ψ , and the mixing length scale l .

Table 3. Parameterizations of the mixing length scale (l) as deployed in MYNN and MYJ. l_s is l in the surface layer, l_t is the turbulent length scale, and l_b is l related to the buoyancy force, κ is the von Karman constant, L is the MO length scale and w_c is a velocity scale, N is the Brunt-Väisälä frequency, z is the height of a model level, and z_i is the PBLH.

MYJ	MYNN
$l = \frac{\kappa z}{1 + \kappa z / \lambda_t}; \quad z \leq z_i$	$\frac{1}{l} = \frac{1}{l_s} + \frac{1}{l_t} + \frac{1}{l_b}$
$\lambda_t = 0.25 \frac{\int_0^{z_i} \sqrt{2TKE} dz}{\int_0^{z_i} \sqrt{2TKE} dz}$	$l_s = \begin{cases} \kappa z / 3.7; & z / L \geq 1 \\ \kappa z (1 + 2.7 z / L)^{-1}; & 0 \leq z / L \leq 1 \\ \kappa z (1 - 100 z / L)^{0.2}; & z / L < 0 \end{cases}$
$l = 0.23 \Delta z; \quad z > z_i$	$l_t = 0.23 \frac{\int_0^\infty \sqrt{2TKE} dz}{\int_0^\infty \sqrt{2TKE} dz}$
	$l_b = \begin{cases} \sqrt{2TKE} / N; & \partial \theta_v / \partial z > 0, z / L \geq 0 \\ \left[1 + 5(w_c / l_t N)^{1/2} \right] \sqrt{2TKE} / N; & \partial \theta_v / \partial z > 0, z / L < 0 \\ \infty; & \partial \theta_v / \partial z \leq 0 \end{cases}$

The two local schemes use slightly different parameterizations for the mixing length scale l (Table 3). In MYJ, l is parameterized with the most common formulation suggested by Blackadar (1962), which is applied for both the stable PBL and the CBL. In MYNN, l is controlled by the smallest among the three mixing length scales: l_s in the surface layer, turbulent length scale l_t dependent on the PBLH, and the length scale l_b related to the buoyancy force, which is effective only in the stable PBL.

In the MYJ scheme the TKE method is used to diagnose the PBLH. The method calculates the PBLH as the height at which TKE decreases to its critical value, which is prescribed to 0.1 Jkg^{-1} in the scheme. MYNN diagnoses the PBLH combining the TKE method (h_{TKE}), and the θ - increase method (h_θ) as described in e.g. Seibert (2000) and Nielsen-Gammon et al. (2008). In the θ - increase method, the PBLH is defined as the height where the potential temperature (θ) exceeds the minimum potential temperature within the PBL by some threshold amount (e.g. 1.5 K). The weighting factor w_f ($\equiv 0.5(\tan z_i(z_i\theta - 200\text{m})/400\text{m}) + 0.5$) is used to control a contribution of the TKE method versus the θ -increase method:

$$z_i = z_{i(TKE)}(1 - w_f) + z_{i(\theta)}w_f \quad (9)$$

In MYNN, the critical TKE is not prescribed as in MYJ, but calculated as the maximum TKE within the first 500 m of the PBL divided by 20. The upper and lower boundaries are set to $0.25 \text{ m}^2\text{s}^{-2}$ and $0.025 \text{ m}^2\text{s}^{-2}$, respectively.

2.3.2. The nonlocal approach: YSU and ACM2

YSU and ACM2 are both the 1st order schemes since they do not use any additional prognostic equation for higher order moments. In the YSU scheme the second order moments are parameterized as

$$\overline{w'\psi'} = -K_\psi \left(\frac{\partial \bar{\psi}}{\partial z} - \gamma_\psi \right) + (\overline{w'\psi'})_{z_i} \left(\frac{z}{z_i} \right)^3 \quad (10)$$

where γ_ψ is a correction to the local gradient, z_i is the diagnosed PBLH, and the last term on the right hand side represents the parameterization of the entrainment flux (see Table 4). The eddy diffusivity for momentum (K_m) is a function of the mixed layer velocity scale w_s , the model level height z and z_i . Eddy diffusivity for heat and moisture is calculated from K_m by using the Prandtl number (Table 4). By adding the counter gradient

correction term γ_ψ to the local gradient, YSU accounts for the contribution of large eddies to the total mixing, which makes this scheme nonlocal.

Table 4. Parameterizations used in YSU and ACM2: $z_s = \min(z, 0.1z_i)$ for unstable and $z_s = z$ for stable conditions. w_s is the turbulent velocity scale, w_{s0} is w_s at $z = 0.5h$, $\overline{(w'\psi')}_0$ is the surface flux. w_e is the entrainment rate at the inversion layer, and $\Delta\psi|_{z_i}$ is the jump of the variable ψ at the inversion layer. Φ is a nondimensional profile function, κ is the von Karman constant, subscripts m and h stand for momentum and scalar variables (heat and moisture), respectively. Detailed parameterizations can be found in Hong et al. (2006) and Pleim (2007).

	YSU		ACM2
Eddy diffusivities	$K_m(z) = \kappa w_s z (1 - z/z_i)^2$ $K_h(z) = K_m / \text{Pr}$	Eddy diffusivities	$K_m(z) = \kappa \frac{u_*}{\phi_m(z_s/L)} z (1 - z/z_i)^2$ $K_h(z) = \kappa \frac{u_*}{\phi_h(z_s/L)} z (1 - z/z_i)^2$
Countergr. term	$\gamma_\psi = 6.8 \frac{\overline{(w'\psi')}_0}{w_{s0} z_i}$	Control. parameter	$f_{cv} = \left[1 + \frac{\kappa^{-2/3}}{0.72} \left(-\frac{z_i}{L} \right)^{-1/3} \right]^{-1}$
Entrain. flux	$\overline{(w'\psi')}_{z_i} = w_e \Delta\psi _{z_i}; w_e = \frac{\overline{(w'\theta_v')}_{z_i}}{\Delta\theta_v _{z_i}}$	Up. conv. mix. rate	$Mu = \frac{K_\psi z_{(1+1/2)}}{\Delta z_{1+1/2} (z_i - z_{1+1/2})}$

The entrainment fluxes of heat, moisture and momentum are explicitly treated in YSU. They are represented as a function of the entrainment rate at the inversion layer (w_e) and the jump of each variable at the inversion layer (see Table 4). w_e is proportional to the buoyancy flux at the inversion layer, which is calculated as -0.15 times the surface buoyancy flux (see Hong et al., 2006). This new feature in the YSU scheme has been shown to be the most critical step toward an improved representation of the CBL mixing. Hong et al. (2006) showed that the YSU scheme with the explicit treatment of the entrainment fluxes accounted for increased boundary layer mixing in the thermally induced free convection regime and decreased mixing in the mechanically induced convection regime, which was a well-known problem with its predecessor, the Medium Range Forecast (MRF) PBL scheme (Hong and Pan, 1996). Furthermore, YSU reproduced a more realistic CI and convective inhibition, which led to an improved representation of the PBL due to the explicit treatment of the entrainment fluxes.

In ACM2, described by Pleim (2007), total mixing is split between local and nonlocal components. In discrete form, vertical turbulent fluxes for momentum, heat or moisture (ψ) are parameterized as

$$\begin{aligned} \overline{w'\psi'}_{l+1/2} = & -f_{cv}Mu \left(z_l - z_{l+\frac{1}{2}} \right) (\psi_1 - \psi_l) \\ & - (1 - f_{cv}) \left[K_{\psi(l+1/2)} \frac{\Delta\overline{\psi}_{l+1}}{\Delta z_{l+1/2}} + K_{\psi(l-1/2)} \frac{\Delta\overline{\psi}_l}{\Delta z_{l-1/2}} \right] \end{aligned} \quad (11)$$

where subscript l denotes an index of the staggered layers (i.e. at the centre of a grid cell), while the regular layers are represented with $l+1/2$ and $l-1/2$ indices. z_l and Δz_l depict the height and thickness of a layer l , respectively. A weighting factor f_{cv} is the key parameter that controls the degree of local versus nonlocal mixing (see Table 4). Under stable and neutral conditions, the overall mixing is only affected by the local transport ($f_{cv}=0$), whilst in unstable situations the total mixing is dominated by the nonlocal components. The first term on the right hand side of Eq. (11) represents the nonlocal part of mixing, with Mu standing for the upward convective mixing rate. Mu is a function of eddy diffusivity K_ψ as displayed in Table 4. The last term on the right hand side of Eq. (11) represents the local part of the mixing. Eddy diffusivity K_ψ is defined as a function of friction velocity u^* , z , z_i , and the nondimensional profile function Φ_ψ formulated similar as in Holtslag and Boville (1993). The expression for calculating K_ψ used in ACM2 is depicted in Table 4 as well.

PBLH is diagnosed with the bulk Richardson number method, which defines PBLH as the height where the bulk Richardson number (Ri_b) reaches a critical value (Ri_{bcr}).

In stable conditions, YSU calculates Ri_b at height z using the formulation

$$Ri_b(z) = \frac{g[\theta_v(z) - \theta_v(z_1)]z}{\theta_v(z_1)[u(z)^2 + v(z)^2]} \quad (12)$$

with θ_v standing for the virtual potential temperature and z_1 is the height of the lowest model level. u and v denote the horizontal wind components. In unstable conditions $\theta_v(z_1)$ in Eq. (12) is replaced with θ_s , which is defined as θ_v near the surface. It is calculated as a function of θ_v at the lowest model level and the virtual potential temperature excess near the surface (for more details see Hong et al., 2006). The value of Ri_{bcr} is set to 0.25 in stable conditions and to 0 in unstable environments.

ACM2 uses a similar formulation as Eq. (12) to calculate the bulk Richardson number in stable conditions. The only difference is that it accounts for the bulk wind shear between a model level and the lowest model level, instead of the values at the each model level as given in Eq.(12). In unstable conditions z_i is diagnosed as the height above the level of neutral buoyancy, and therefore the Richardson method is applied over the interfacial layer only. Therefore, first the top of the CBL (z_i) is estimated as the height where the $\theta_v(z_i) = \theta_s$, with θ_s being formulated as in YSU. Then, Ri_b for the interfacial layer is calculated using the expression

$$Ri_b(z) = \frac{g[\theta_v(z) - \theta_s](z - z_i)}{\overline{\theta}_v\{[u(z) - u(z_i)]^2 + [v(z) - v(z_i)]^2\}} \quad (13)$$

where $\overline{\theta}_v = [\theta_v(z) + \theta_v(z_i)]/2$ and $z \geq z_i$. Ri_{bc} is set to 0.25 in both stable and unstable cases. Within the nonlocal PBL schemes, the PBLH is a mixing height scale. Therefore, the sensitivity of such schemes to the PBLH diagnostics is very high, which represents a major drawback for the nonlocal parameterizations.

3. Dry case study

The methods and results presented in this chapter are based on the published article by: Milovac, J., K. Warrach-Sagi, A. Behrendt, F. Späth, J. Ingwersen, and V. Wulfmeyer (2016), Investigation of PBL schemes combining the WRF model simulations with scanning water vapour differential absorption lidar measurements, *J. Geophys. Res. Atmos.*, 121, 624–649, doi:10.1002/2015JD023927.

The influence of the model configuration on representation of the PBL features, such as PBL evolution, moisture and temperature profiles and the PBLH during dry weather conditions is analysed and compared with the WVDIAL measurements. The coupling strength between the land surface and atmosphere is investigated via intercomparisons of the simulated mixing diagrams. The measurements are introduced in chapter 3.1, while the study site is described in 3.2. The results are given in 3.4, and discussed in section 3.5.

3.1. Study area and weather conditions

The study site is located in western Germany, near the village of Inden and the Jülich Research Centre (Figure 2). During the field campaign TR 32 FLUXPAT (funded by the German Science Foundation) in September 2009, worldwide the first scanning WVDIAL measurements were taken at the site (50°51'20.55'' N, 6°22'4.91'' E, 105 m above sea level; Behrendt et al., 2009). The WVDIAL moisture gradients, in combination with variances of the data, facilitate the identification of turbulent structures and allows for unambiguous identification of e.g. PBLH and the moist residual layer during morning and evening transition periods. The measurements were performed over an agriculturally dominated area in a relatively flat terrain within the River Ruhr catchment. However, apart from sugar beet, the fields were harvested in September 2009. An open-pit mine is located in the West, and the village of Inden in the North. Soil texture at the study site is primarily silty loam.

On 8 September 2009 during the day the weather in central Europe was controlled by a high pressure system with its centre over Lithuania. During the whole day the weather at the study site was similar across most of Europe, cloudless and dry with weak synoptic

forcing. Minimum 2 m temperature measured in the area was about 15°C, while the maximum was between 28 and 30°C. The environmental air was rather dry, with relative humidity at 2 m height between 35 and 55% during the day. The 2 m dew point temperature close to the ground measured with radiosonde at 16 UTC was 12.8°C. Most of the day it was calm with weak winds. Until late afternoon, winds were southerly, south-westerly direction with up to 5 ms⁻¹ speed at elevations ranging from 30 to 360 m. After 17:30 UTC the wind speeds increased up to ~ 5-9 ms⁻¹. At night time the winds turned to an easterly and north-easterly direction. Wind data were obtained from sodar measurements performed at the study site on 8 September 2009 (Drüe, personal communication 2014).

3.2. Measurements

The WVDIAL is a scanning system, capable of performing 3-dimensional observations of humidity with the highest spatial/temporal resolution of all existing water-vapour remote sensing systems (Behrendt et al., 2009; Wagner et al., 2013; Späth et al., 2016). Absolute humidity is measured with a spatial and temporal resolution of 15 to 300 m and 0.5 to 10 s, respectively. The maximum range is several km during day and night and can be adapted to the PBL evolution to capture the whole depth of the PBL. Validation studies confirmed the high accuracy of the WVDIAL instrument (Bhawar et al., 2011; Muppa et al., 2016). Combining range-resolved measurements with scanning capability, different scan patterns (e.g. range-height indicator or plane-polar indicator scans) can be performed with the WVDIAL. The instrument allows for different types of volume scan patterns to be realized automatically. These properties allow for studying the temporal and spatial structure of the water vapour field in detail.

Figure 7 shows the range-height indicator scan of the absolute humidity field measured on 8 September 2009 at 6 time steps between 8:48 and 17:52 UTC. The scan speed was 0.1°s⁻¹. An integration time of 10 s was used for each profile resulting in an angular resolution of 1°. Each of the scans took 24 minutes to complete. The complex structure of the humidity field and its typical development in the course of the day is revealed: several horizontal layers are seen in addition to turbulent structures close to the ground which extend to the full height of the CBL of ~ 2 km in the afternoon.

In the morning hours (Figure 7a, b, c) a CBL started to evolve, which is visible from the strong increase in humidity close to the land surface. High humidity content above the evolving CBL corresponds to the residual layer from the day before. At about 10 UTC (Figure 7d) the evolving CBL overtook the residual layer. In the afternoon, the CBL was well mixed and about 1.6 km high (Figure 7e), with humidity content lower than on the previous scan. Also, the interfacial layer with entrainment of drier air from aloft can be revealed at about 1.6 and up to 2 km. In Figure 7f collapsing of the CBL started, but higher humidity content and a clear boundary at the ~ 1.2 km height indicate presence of the relatively strong residual layer (up to 1.2 km) remained from the daytime.

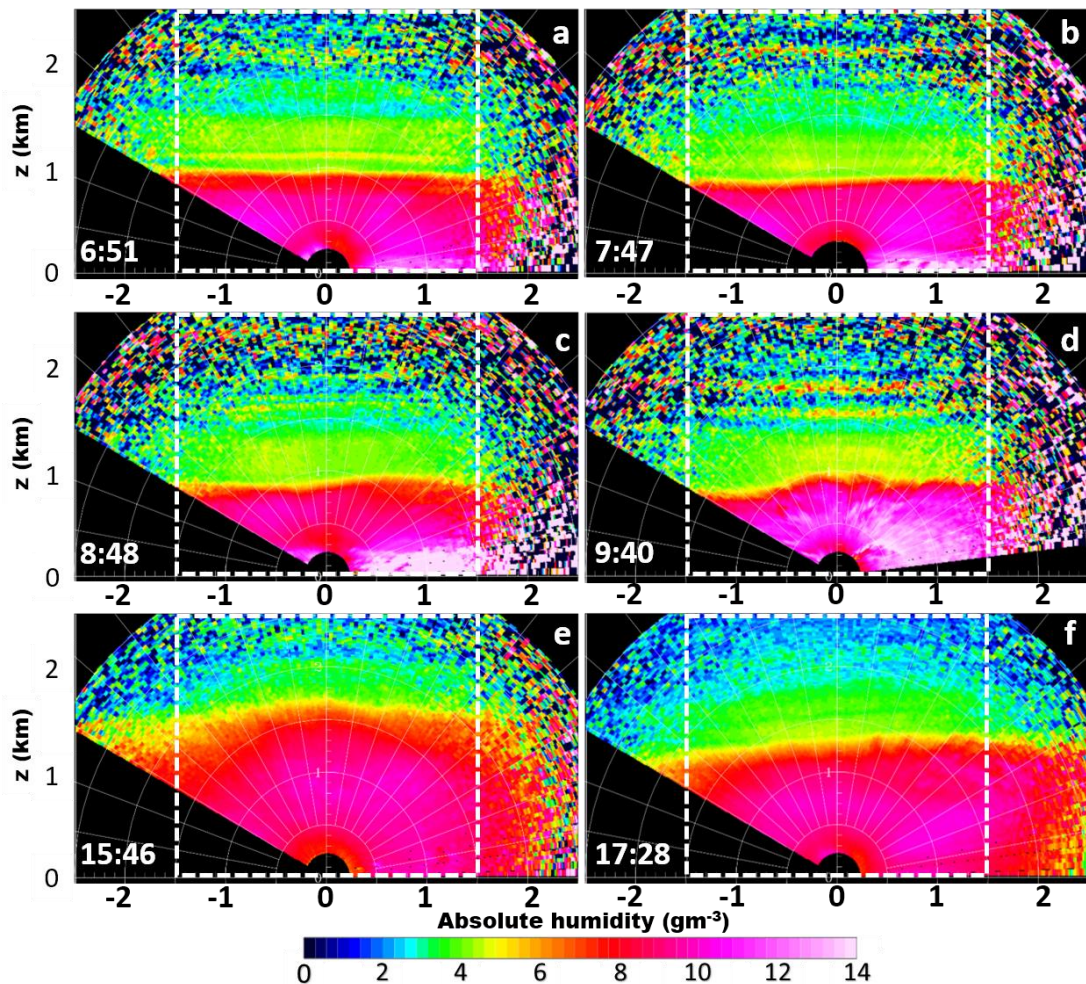


Figure 7. The WVDIAL scans of absolute humidity on 8 September 2009. The starting time of the each scan in UTC is denoted in the lower left corner of the corresponding panel. The duration of the each scan was approximately 24 minutes. White rectangles on the scans denote the area (3 km in horizontal and 2.5 km in vertical direction) over which the measured data were averaged to obtain the absolute humidity profiles.

The vertical profiles of absolute humidity used for validation in this study were obtained by averaging the scanning data over a range of 3 km, 1.5 km in each horizontal direction from the WVDIAL site (white dashed rectangle in Figure 7). As humidity within the CBL is highly variable, the averaging scheme of the WVDIAL scans yields data which are more representative for comparisons with the model output and provide lower sampling errors than e.g. radiosonde profiles, which sample the atmosphere only along its path at certain times. The profiles are given in chapter 3.4.1 along with the model simulations and the results are discussed in chapter 3.5.

3.3. Methodology - the mixing diagram

The mixing diagram approach, introduced by Betts (1992) and extensively used by Santanello et al. (2009; 2011; 2013) is applied for intercomparison of the PBL schemes and LSMs to analyse and quantify SVA feedback (Figure 8).

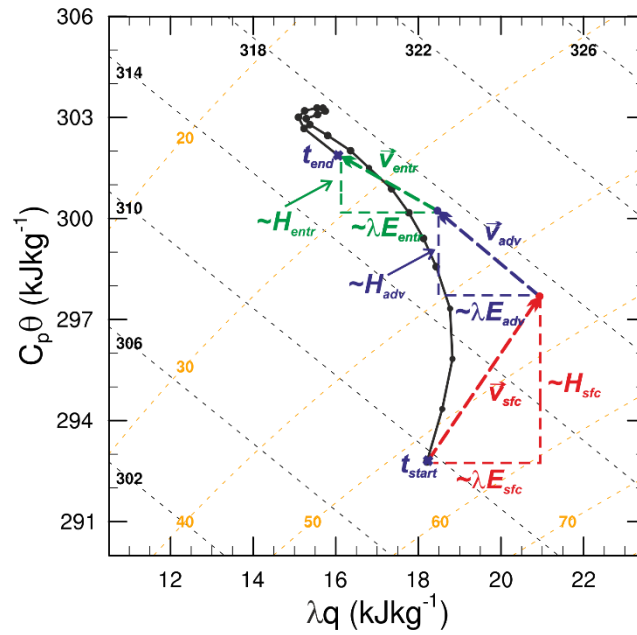


Figure 8. The mixing diagram - an example of diurnal coevolution of $C_p\theta$ vs. λq from 7 to 17 UTC, with vectors (dashed lines with arrows) and their components (horizontal and vertical dashed lines) that contribute to the PBL total flux.

In this approach the diurnal evolution of the two conservative variables, 2-m θ and q , is related to the change of heat and moisture at the land surface and within the CBL. To

relate the diurnal change of these two conservative variables to the heat and moisture budgets, they need to be represented in the energy field. In the mixing diagram it is done by multiplying θ with C_p and q with λ , whereupon the changes of heat and moisture in the CBL over some time interval Δt can be considered as vectors in this λq - $C_p\theta$ diagram, as denoted in Figure 8.

In cases when horizontal advection of the mean scalars can be neglected, the local change of a conserved variable (potential temperature θ or humidity q) in the CBL over time interval (Δt) is the sum of the effects from the surface and in the interfacial layer:

$$C_p \frac{\Delta\theta}{\Delta t} = \frac{\overline{H_{sfc}} - \overline{H_{entr}}}{\rho_m \bar{z}_i} \quad (14)$$

The subscripts *sfc* and *entr* denote the surface and entrainment, respectively. ρ_m is the mean air density in the CBL. Overbars mark the averaged values over time period Δt . From Eq. (14) the x component of the surface vector (\mathbf{V}_{sfc} , red vector in Figure 8) can be calculated as

$$C_p \Delta\theta_{sfc} = \frac{\overline{H_{sfc}} \Delta t}{\rho_m \bar{z}_i} \quad (15)$$

The similar principle is valid also for calculating the y component of \mathbf{V}_{sfc} ($\lambda \Delta q$), only with θ being replaced with q , H with λE and C_p with λ .

To obtain bulk information about feedbacks during a day between heat and moisture on the one hand and the PBL evolution on the other hand, the daytime mean approach and the stepwise (i.e. hourly) integration approach can be used. It has been shown that the more sensitive approach is the daily mean (Santanello et al., 2009), which is also deployed in this sensitivity study. The x and y components of the entrainment vector (\mathbf{V}_{entr} , green vector in Figure 8) correspond to mean sensible and latent heat fluxes at the interfacial layer, respectively. These can be obtained using simple vector algebra (e.g. the mean entrainment heat flux can be calculated from a residual vector that connects \mathbf{V}_{sfc} and the final values of λq and $C_p\theta$ at t_{end}).

An advection term in the budget equation for scalar variables in the PBL is often not negligible. Moreover, it is shown that, together with the entrainment term, it is one of the main constraining factors for closing the budget equation (e.g. Santanello et al., 2005). The mixing diagram approach also allows incorporating an impact of horizontal

advection of mean values by adding an advection vector (\mathbf{V}_{adv} , blue vector in Figure 8) on the diagram. The x component of this vector can be calculated using:

$$C_p \Delta \theta_{adv} = C_p \Delta t \left[\langle \bar{u} \frac{\partial \bar{\theta}}{\partial x} \rangle + \langle \bar{v} \frac{\partial \bar{\theta}}{\partial y} \rangle \right] \quad (16)$$

with u and v standing for x and y wind components, and overbars denoting time averages. Angle brackets stand for averaged values within the CBL column. By replacing C_p with λ and θ with q in Eq. (16), the y component of \mathbf{V}_{adv} can be calculated. \mathbf{V}_{adv} is then added to \mathbf{V}_{sfc} . A new residual vector that connects \mathbf{V}_{adv} with the final values of λq and $C_p \theta$ at t_{end} represents the modified entrainment flux (see Figure 8).

The mixing diagram approach is a useful technique to diagnose the degree of coupling between the land surface and atmosphere on diurnal time scales. From the diagram it is possible to diagnose total mean fluxes of heat and moisture during a day within the PBL, as well as the contribution of the land surface and entrainment mean fluxes to the total mean flux. Negative/positive values of the mean sensible heat flux at the interfacial layer denote mean entrainment of cold/hot air from the free atmosphere, whilst negative/positive latent heat flux stands for the influx of dry/moist air through the interfacial layer. Using the aforementioned information obtained from the mixing diagrams, the mean Bowen ratio at the interfacial layer can be easily calculated. All details about vector representation of energy budgets and mixing diagrams are available in Santanello et al. (2009; 2011; 2013).

3.4. Results

In the section 3.4.1 the WVDIAL humidity profiles have been compared with the six WRF simulations for the first time ever in order to analyse the sensitivity of the model performance to PBL schemes and LSMs. In section 3.4.2 the simulated temperature profiles are compared with the radiosonde measurements executed at 16 UTC at the study site. A quantity that describes the ability of a PBL scheme to depict profiles of thermodynamic variables is PBLH (e.g. Coniglio et al., 2013). In subsection 3.4.3 the PBLH calculated from the simulations with two techniques are compared with the PBLH from WVDIAL absolute humidity profiles, which was estimated as the height with the highest moisture gradient (e.g. Seibert, 2000; Seidel et al., 2010, Pal et al., 2010). The

sensitivity of the WRF model to the PBL schemes and LSMs in simulating the local SVA coupling on a diurnal time scale is represented using the mixing diagram approach as described in the previous section. The results are presented in section 3.4.4.

3.4.1. Absolute humidity profiles

The high-resolution WVDIAL measurements, in combination with variances of the data, facilitate the identification of turbulent structures and allows for unambiguous identification of e.g. PBLH and the moist residual layer during morning and evening transition periods. On 8 September 2009, these measurements were available from 7 to 10 UTC at an hourly scale, and in the afternoon at 16 and 18 UTC. The residual layer from the previous day, with a strong inversion layer at ~ 900 m is visible at 7 and 8 UTC (black dotted lines in Figure 9 and Figure 10). The PBL started to evolve slowly at the beginning of the day (from 7 to 9 UTC), and at 10 UTC it merged with the residual layer and reached the inversion layer. The PBL was well mixed (almost constant humidity profile) at 16 UTC, but already in the decay phase, whilst at 18 UTC an abrupt collapse of the PBL was observed. The measurements are compared with the absolute humidity profiles simulated with the six WRF simulations in the following two sections.

a) Sensitivity to the PBL parameterizations

Figure 9 displays the sensitivity of WRF to the PBL schemes in simulating the absolute humidity profiles in comparison with the WVDIAL measurements. The LSM selected for this comparison is NOAH.

The discrepancies between the simulations and the measurements are ranging up to 2 gm^{-3} , being the highest at the start of the PBL evolution and at the time of the PBL collapse. The comparisons of the profiles show that all of the schemes fail to reproduce the residual layer and the strong morning inversion observed at ~ 900 m (Figure 9a, b, c). The PBLH in the CBL can be estimated from vertical humidity profiles as the height where the highest moisture gradient occurs (e.g. Seibert, 2000).

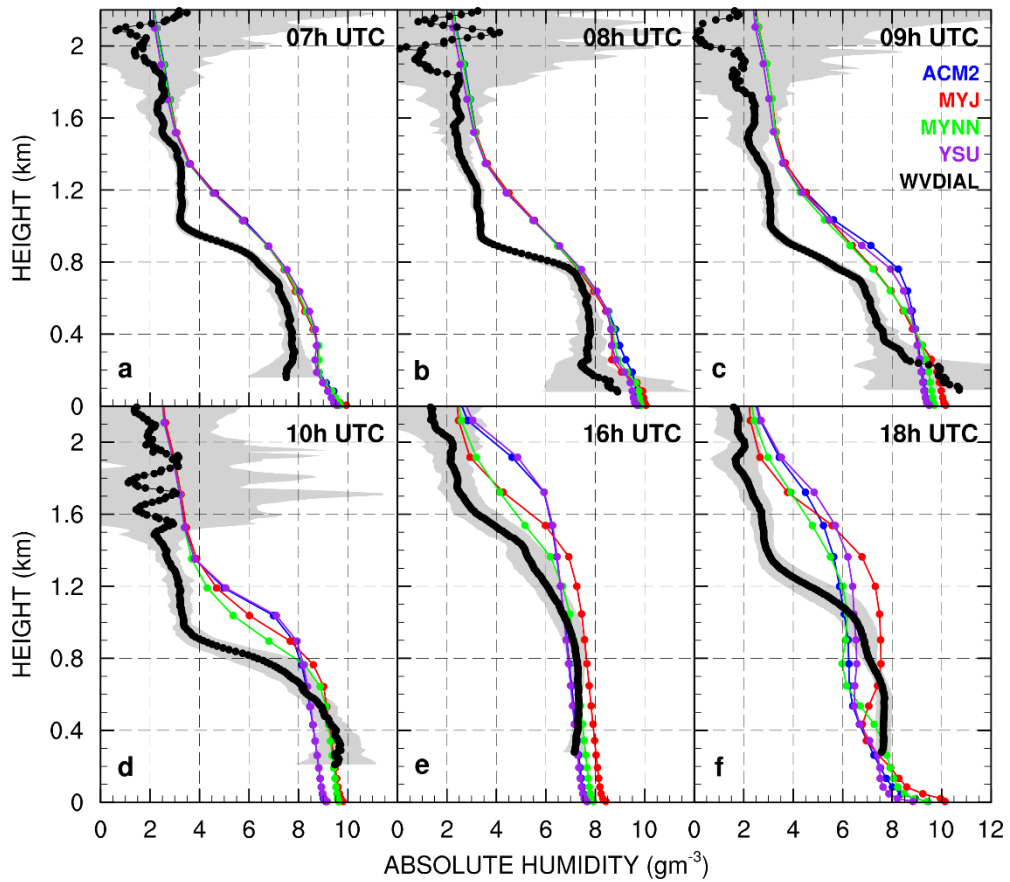


Figure 9. Comparisons of the measured absolute humidity profiles (black dots) with the profiles simulated with WRF configured with the four PBL schemes (ACM2 in blue, MYJ in red, MYNN in green and YSU in purple) and the Noah LSM. Shaded grey areas correspond to the standard deviation of the scans due to averaging.

At 7 am the simulated profiles are very similar. They start to diverge from the surface as the CBL evolves, and deviate at 8 UTC in the lowest 500 m (Figure 9b). The observed humidity gradient between 100 and 250 m is stronger than the simulated. However, with the two local schemes (MYJ and MYNN) the gradient is closer to the observation than with the nonlocal schemes. From 9 UTC onwards, all the PBL schemes result in a higher CBL compared with the measurements. The observed humidity in the lowest 400 m has increased, showing a gradient of 3 gm^{-3} between 100 and 400m height (Figure 9c). This is not simulated by the PBL schemes, which only show a decrease of the gradient and an increase in humidity between 400 and 1000 m height. At 10 UTC (Figure 9d) the residual layer vanished and the morning CBL is developed below 800 m. The PBL schemes show a less intense gradient. In the non-local schemes the highest gradient is 200 m above the local schemes' gradient. Therefore, the highest CBL is obtained with the nonlocal ACM2 and YSU schemes, which is up to 400 m higher than observed (Figure 9d, e).

Furthermore, the nonlocal schemes also account for the fastest growth of the PBL in the morning hours (Figure 9b, c). Slower evolution and a shallower, but still too high CBL was simulated with the local MYJ and MYNN schemes. At 16 UTC (Figure 9e), when the CBL was fully developed, the shallowest CBL was obtained with the MYNN scheme. Nevertheless, the humidity gradient of 5 gm^{-3} per 600 m is only simulated by the local MYJ scheme, though the overall humidity is 1 gm^{-3} larger than observed, and the PBLH is for about 250 m higher. Figure 9f shows that the two nonlocal schemes simulate a strong transition, while in MYNN the transition is less pronounced, and MYJ miss to reproduce it completely. The simulated reduction of the inversion layer from 16 to 18 UTC is much more gradual for all the PBL schemes than observed, which resulted in a too high residual layer that formed after the PBL collapse (Figure 9f). ACM2, YSU and MYNN simulate a significant drying in the upper PBL from 16 to 18 UTC, which is not the case with MYJ. Drying of the CBL can be related to advection and entrainment of dry air from the free atmosphere, both parameterized differently in the schemes.

The difference between the profiles obtained with the two nonlocal schemes is almost negligible, while the profiles with the local schemes show significant differences in representing PBL evolution. The largest differences appear when the CBL is well mixed, and during its collapse. MYJ simulates the CBL with higher moisture, stronger inversion and the thinner interfacial layer than MYNN.

b) Sensitivity to the LSMs

Figure 10 shows the WRF sensitivity to LSMs. The WVDIAL measurements of absolute humidity profiles are compared with the NOAH-MP and NOAH simulations, coupled with MYNN and YSU.

The discrepancies between the simulations evolve during the morning hours and result in a different CBL evolution (Figure 10a, b, c). At 10 UTC (Figure 10d) the CBL is drier with NOAH-MP than with NOAH. In the afternoon, the CBL was well mixed (Figure 10e) and a significant sensitivity of WRF to the coupled LSM is not only apparent close to the ground, but it extends up to the CBL top and the lower free troposphere. In the case of NOAH-MP, the CBL is significantly drier (between ~ 0.5 and $\sim 1.5 \text{ gm}^{-3}$). At 16 UTC the PBLH is slightly higher ($\sim 100\text{m}$), and humidity gradients in the interfacial layer are marginally lower with NOAH-MP than with NOAH (Figure 10e).

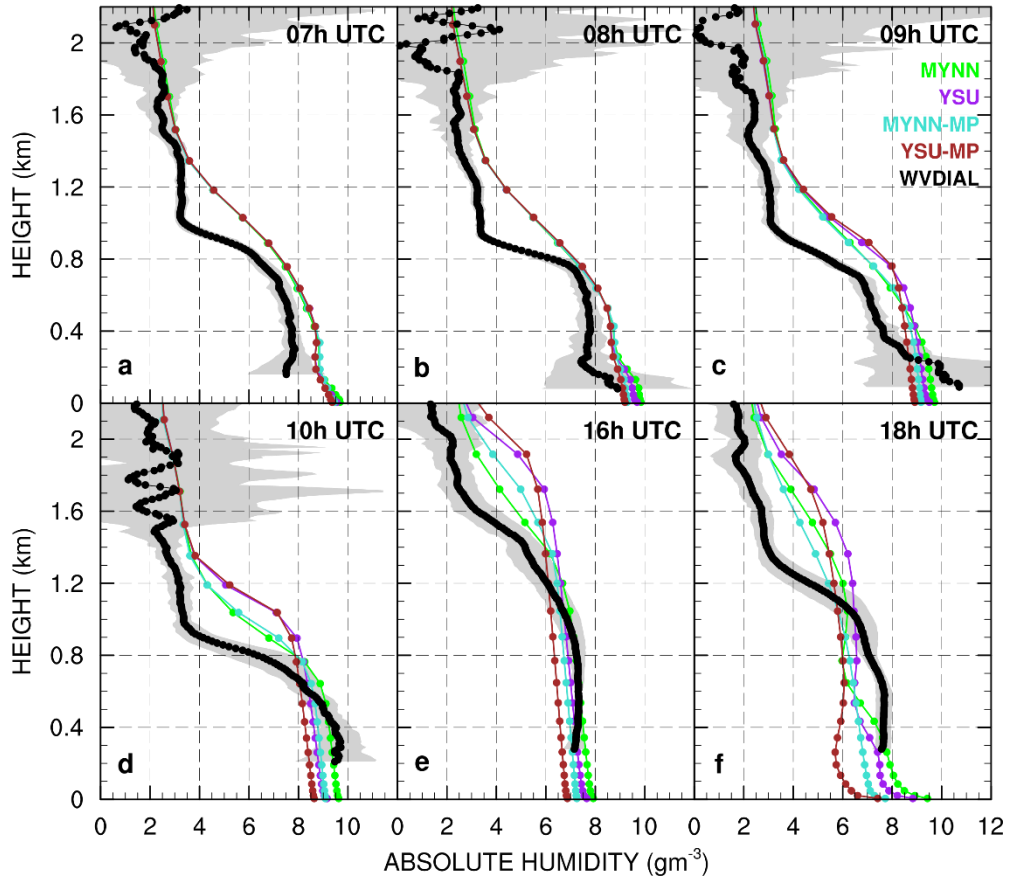


Figure 10. Comparisons of the WVDIAL absolute humidity profiles with the profiles simulated with WRF configured with the two PBL schemes (MYNN and YSU) and the two LSMs (NOAH and NOAH-MP). Turquoise lines show MYNN with NOAH-MP and brown YSU with NOAH-MP. Remaining colours as in Figure 9.

At 18 UTC, just after the CBL collapsing, each profile deviates significantly one from another due to both, different LSMs and different PBL schemes. All in all, the results indicate that a different LSM causes different SVA feedback and that this affects entrainment processes at the interfacial layer, and thus impacts on the PBL structure.

3.4.2. Temperature profiles

At 16 UTC 8 September 2009 a radiosonde was launched from the study site. The temperature measurements are compared with the six simulations in a form of skew T -log p diagram (Figure 11a) to further investigate the CBL features. The Figure 11a shows that the measured capping inversion occurs at approximately 1400 m, which is about 200 lower than in WVDIAL. WRF in all six experiments has a significantly higher inversion layer (more than 400 m higher, depending on model configuration).

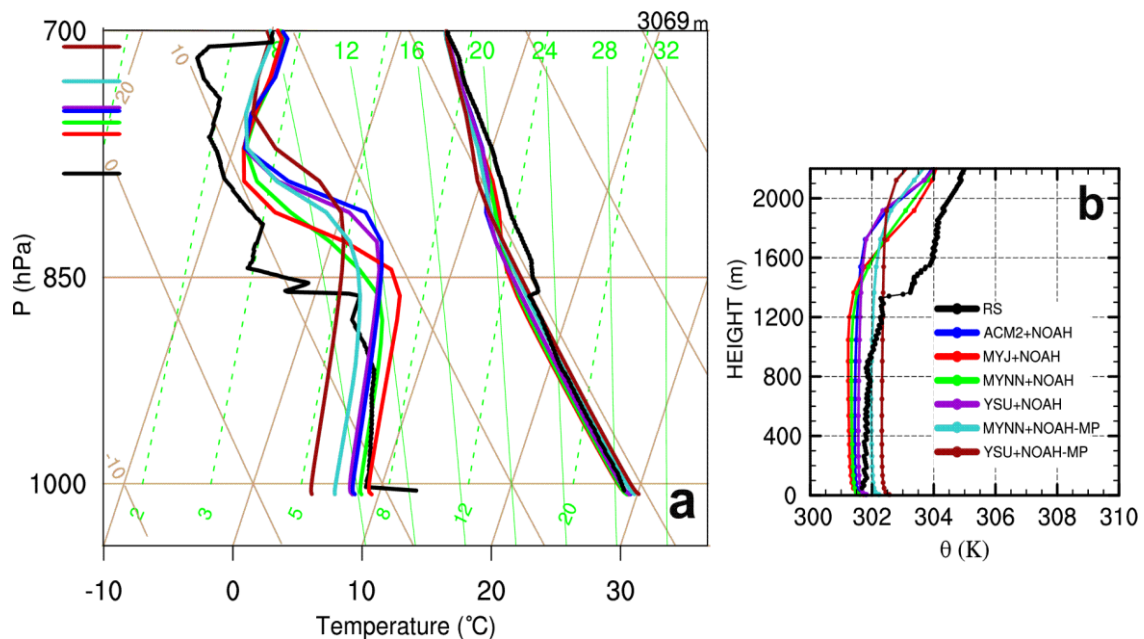


Figure 11. SkewT-logp diagram (a) showing dew point temperature (right profiles) and air temperature profiles (left profiles) at 16 UTC 8 September 2009 as simulated with the six WRF runs along with the radiosonde measurements. Lines perpendicular to the left vertical axis of the diagram are the LCL values in hPa as calculated from the simulations and the measurements. On (b) the potential temperature profiles valid at 16 UTC as simulated with the six model simulations and measured with the radiosonde. Colours of the lines depicted in the legend located in the lower right corner of the (b), with RS standing for radiosonde measurements.

Dew point temperature shows a higher dependence on the selected PBL scheme and LSM. Stronger humidity gradients at the inversion are obtained with the nonlocal schemes. This results in a thinner inversion layer than with the local schemes. The most humid CBL and consequently the lowest PBLH is simulated by MYJ, which coincides with the results in section 3.4.1. Within the CBL the model is more sensitive to the LSM choice, while the height and thickness of the inversion layer is more sensitive to the PBL scheme. Comparing to the radiosonde measurements, all the schemes simulated the afternoon overshooting, especially the simulations with nonlocal schemes coupled with NOAH-MP. The inversion layer simulated with the local schemes is too thick, and the inversion is not as sharp as measured. This is especially the case with MYJ simulations. Comparing to the WVDIAL measurements (section 3.4.1), one can see that the radiosonde measured sharper inversion at 16 UTC (Figure 11a) than the WVDIAL (Figure 9e, Figure 10e), which smoothens the jump at the inversion due to averaging. This difference may be related to the data averaging scheme that was performed to obtain

the WVDIAL profiles which may smoothen the gradients, while the radiosonde measurements are a snapshot of the atmosphere along its path (see section 3.2).

The observed LCL height of 787 hPa at 16 UTC is overestimated by all simulations as well. The difference between local and nonlocal PBL schemes applied with NOAH becomes evident in the simulated LCL, which is lower with the local schemes (MYNN: 756 hPa, MYJ: 763 hPa) than with the nonlocal schemes (YSU: 747 hPa, ACM2: 749 hPa). The LCL height is increased by 18 hPa for YSU and 17 hPa for MYNN when applying NOAH-MP.

Potential temperature profiles at 16 UTC depicted in Figure 11b indicate that the profiles simulated with the local PBL schemes are slightly stable, especially with MYJ. The observed unstable profiles are simulated with the nonlocal PBL schemes. The stability of the CBL is not influenced by the LSMs in this case study. The bulk difference between the simulated temperatures within the CBL is less than 1 K, but nevertheless, the profiles show that the CBL was slightly warmer with the local schemes, as well as with the NOAH-MP. NOAH-MP slightly increased the PBLH relative to NOAH, but all six simulations strongly overestimate the PBLH (> 400 m) compared with the radiosonde measurements. This indicate that too much mixing is produced with all the PBL schemes analysed in this study.

3.4.3. Planetary boundary layer height

Each PBL scheme deployed uses a different formulation to diagnose the PBLH (see section 2.3), and therefore comparisons of the model diagnostics with the measurements would lead to inconsistent conclusions (e.g. LeMone et al, 2013). To avoid this, we chose two criteria to calculate the simulated PBLH. A common method to calculate the top of the CBL defines the PBLH as the height where the virtual potential temperature lapse rate exceeds some threshold value (e.g. Seibert et al., 2000). We chose the threshold value to be 2 Kkm^{-1} , as suggested by LeMone et al. (2013). The second criteria applied is the bulk Richardson method as used in YSU, with Ri_{bcr} set to 0.25 (e.g. Hong et al. 2006; Jeričević and Grisogono, 2006). At 7 and 18 UTC it was not possible to estimate PBLH since the PBL was shallower than the lowest level at which the WVDIAL measurements were performed.

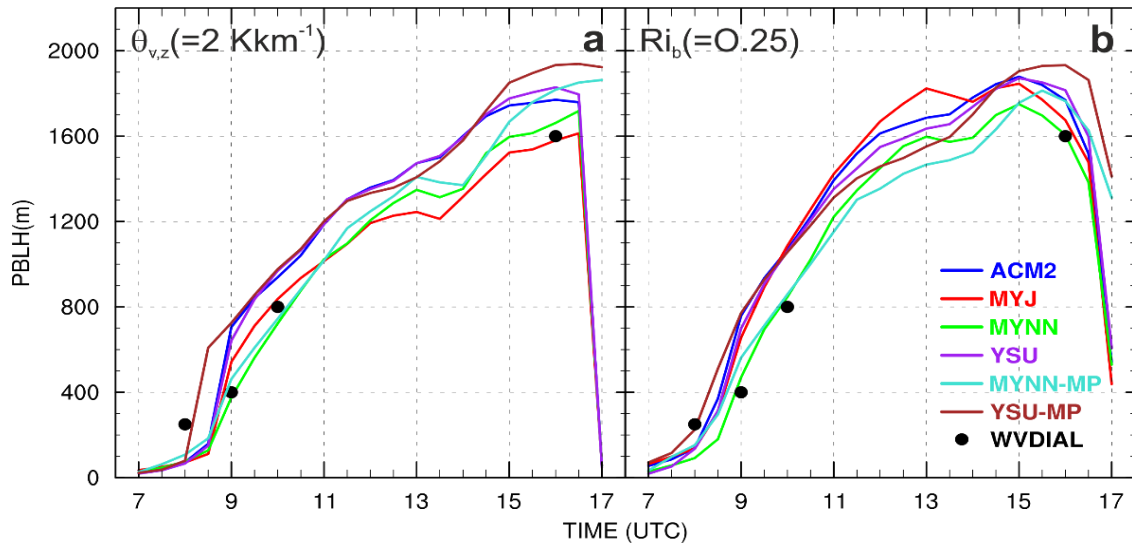


Figure 12. Temporal change of PBLH from WRF compared with the PBLH estimates obtained from the WVDIAL measurements (black dots) on 8 September 2009 between 7 and 17 UTC. The PBLH from the model is calculated using the virtual potential lapse rate method (panel a) and the bulk Richardson method (panel b).

Figure 12a shows the comparisons of the PBLH obtained from the simulations using the virtual temperature lapse rate method. The maximum difference between the PBL schemes is ~ 300 m. The nonlocal schemes exhibit a more rapid evolution of the PBL than the local schemes, which is in agreement with similar studies (e.g. Moeng and Sullivan, 1994; Shin and Hong, 2011; Xie et al., 2013; Coniglio et al., 2013). There is no significant difference in the results between the two nonlocal schemes, ACM2 and YSU, whereas the PBLH is higher with MYNN than with MYJ most of the day. Only in the morning, the evolution of the PBL is slightly faster with MYJ than with MYNN. From the time when the CBL is fully mixed (i.e. at 11 UTC) the PBLH is higher with MYNN ($\sim +100$ m) than with MYJ. Comparing the results with the measurements, the PBLH obtained with the local schemes fits better than with the nonlocal schemes, especially in the morning. The PBL evolution as simulated with the both nonlocal schemes is too fast when comparing with the measurements.

The PBLH obtained with NOAH-MP is similar or up to ~ 100 m higher than with NOAH. Using YSU, the start of the PBL evolution occurs 30 minutes earlier in NOAH-MP than with NOAH. The highest difference between the two LSMs occurs at the time of the PBL collapse. NOAH-MP postpones the occurrence of the PBL decay for at least 30 minutes. Furthermore, the increase in the PBLH just before the collapse obtained with MYNN and NOAH-MP is not realistic.

The PBLH maximum occurrence in all cases is in the late afternoon (here at or after 16 UTC). This is not typical for the PBL evolution on clear sky weather conditions (e.g. Stull, 1988; Seibert et al., 2000; Zhang et al., 2014). Therefore, we applied the bulk Richardson method to calculate the PBLH from the model as well. The results displayed in Figure 12b show that PBLH maximum obtained with this method occurs earlier than with the virtual potential lapse rate method (at ~ 15 UTC with NOAH and 15:30 UTC with NOAH-MP), which seems to be more realistic for a dry CBL. The highest difference between the two methods are obtained at midday and in the early afternoon, ranging from 300 to 500 m. The most notable difference in the results between the two methods deployed is obtained with MYJ. The PBLH in the CBL is significantly increased with MYJ when the bulk Richardson method was used. This indicates that the impact of wind shear on the PBL evolution, accounted for in the bulk Richardson method, might be higher in the MYJ simulations than in the other simulations. Furthermore, with NOAH-MP the PBL collapsing occurs later than with NOAH as well. The delay of the collapse might also be related to wind shear at the top and bottom of the PBL (e.g. Pino et al., 2006; Goulart et al., 2010; Darbieu et al., 2015), but the investigation of the wind shear driven PBLs is beyond the scope of this thesis. With this method, results obtained with MYNN and NOAH are fitting best with the measurements, which is consistent with the previous results (see section 3.4.1) and studies such as e.g. Coniglio et al. (2013) and Huang et al. (2013).

3.4.4. *Land-atmosphere coupling*

The results in sections 3.4.1, 3.4.2 and 3.4.3 demonstrate the strength of the land surface influence on the PBL evolution. In this section we applied the mixing diagram approach to quantify the simulated influence of land surface processes, advection and entrainment on the PBL evolution. The method is applied on a diurnal time-scale at the model grid point closest to the study site. Heat and moisture advection necessary to obtain \mathbf{V}_{adv} [right hand side of Eq. (16)] is calculated at the model grid point as well. The values denoted in the diagram represent mean advection of heat (x component of \mathbf{V}_{adv}) and moisture (y component of \mathbf{V}_{adv}) in the CBL over a time period Δt (here 10 hours).

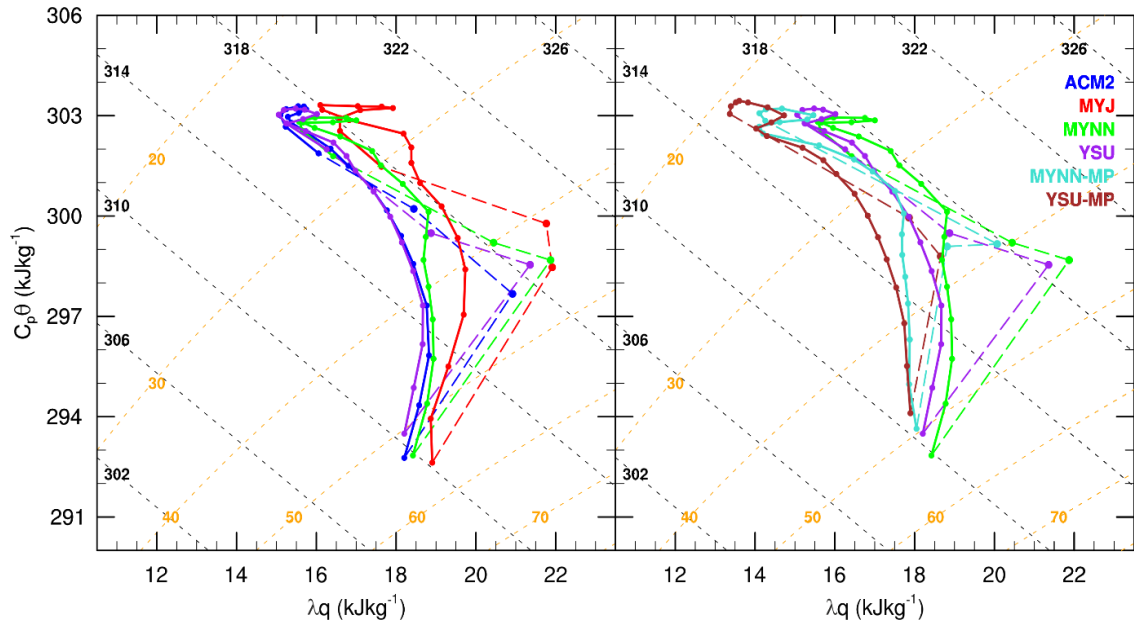


Figure 13. Mixing diagrams for 8 September 2009 between 7 and 17 UTC. The simulated coevolutions of moisture content λq and heat content $C_p\theta$ are in solid lines, while dashed lines stand for vectors corresponding to the surface (\mathbf{V}_{sfc}), advected (\mathbf{V}_{adv}) and entrainment (\mathbf{V}_{entr}) fluxes. The simulations with the 4 PBL schemes coupled with NOAH are on panel (a), and on (b) are the simulations with MYNN and YSU in combination with NOAH and NOAH-MP. Colours of the lines correspond to the experiments as denoted in the legend in the upper right corner of panel (b). Overlaid are lines of constant θ_e (in K; black dashed) and RH (in %; orange dashed).

The mixing diagram depicted in Figure 13 demonstrates the sensitivity of WRF to the four PBL schemes, all with NOAH, in representing the temporal change of heat and moisture during a 10-hour period (from 7 UTC until 17 UTC) on 8 September 2009. Differences between the simulations are small, with low variability of humidity content in the lower PBL during the day. Slightly faster drying of the lower CBL was simulated with ACM2 and YSU than with the local PBL schemes, indicating higher mixing properties with the nonlocal schemes. The highest moisture in the CBL was accounted with MYJ.

Sensitivity of WRF to the LSMs (NOAH and NOAH-MP) together with its sensitivity to the PBL schemes (MYNN and YSU) is shown in Figure 13b. The curves demonstrate the higher sensitivity of the model to the LSMs than to the PBL schemes. The CBL simulated with NOAH-MP is drier and slightly warmer than the one simulated with NOAH. Lines of constant relative humidity (RH) are overlaid on the mixing diagrams. There is no significant difference in the RH during the day between the simulations. All configurations simulated the change of about 20% in RH during the 10 hour period. However, up to 5 % lower values of RH are accounted with the nonlocal PBL schemes

(Figure 13a) as well as with the NOAH-MP runs (Figure 13b). Moist static energy, which is defined as a sum of sensible heat, geopotential and latent heat, is proportional to equipotential temperatures (θ_e). Therefore, an increase in θ_e means a buildup in moist static energy, which implies an increase in potential for a convection occurrence. Therefore, θ_e is a useful measure of the potential for low-level heat and moisture impact on cloud development and precipitation (e.g. Santanello et al., 2011). Lines of constant θ_e are overlaid on the mixing diagrams as well. This allows for simple quantification of the moist static energy during the day for the each simulation. With ACM2, YSU and MYNN (Figure 13a) WRF simulated an increase of θ_e by approximately 6 K during the day, while about 8 K was simulated with MYJ. This indicates that slightly higher potential for cloud development was simulated with MYJ. Comparing an impact of the LSM on the θ_e change, NOAH-MP decreases the value for about 2 K, i.e NOAH-MP reduces the potential for cloud development with both, MYNN and YSU. The overall change of θ_e depends on surface evaporation, the PBL evolution, advection and the processes at the entrainment. These processes can be quantified from the mixing diagrams and the results for this case study are summarized in Table 5. One of the derived variables from the mixing diagram is the mean entrainment Bowen ratio (β_{entr}). The values of β_{entr} indicate that the mean entrainment of warm air is slightly higher than the mean entrainment of dry air for all the PBL schemes deployed, since $\beta_{entr} < -1$. The values of ratios between the mean latent heat flux at the entrainment and that at the land surface ($A_{\lambda E}$) indicate that the highest mean entrainment of dry air (negative values) was acquired by the nonlocal schemes, while the lowest values were obtained with MYJ scheme.

In case of the local PBL schemes advected fluxes can be neglected due to the low ratios (< 0.1) between the mean advected fluxes and the sum of the mean surface and entrainment fluxes ($AD_{\lambda E}$ for latent heat, and AD_H for sensible heat). Simulations with the nonlocal schemes simulated significant impact of the mean advected fluxes to the mean total fluxes, with the values of around 0.3 for the case of latent heat flux.

The differences between the values derived from the mixing diagrams are significantly higher when comparing the results from the two LSMs to those obtained from the four PBL schemes. The significantly higher Bowen ratio at the land surface (β_{sfc}) calculated with NOAH-MP implies that less energy is partitioned into latent heat compared to NOAH. Since the radiation scheme used in all the simulations is the same, the R_n should not vary significantly between the schemes. Therefore, to close the energy balance at the

land surface in Eq. (3), the residual latent heat flux went to H or/and G . This significant difference in β_{sfc} between the LSMs is due to difference in evaporative physics of the LSMs. In section 3.5.2 this has been discussed more in detail.

Table 5. The diagnostics extracted from the mixing diagram at Figure 13: Mean ratio between sensible and latent heat flux at the interfacial layer (β_{entr}), the mean ratios of the fluxes of latent ($A_{\lambda E}$) and sensible heat (A_H) at the land surface to those at the interfacial layer are also diagnosed from the mixing diagrams, the mean quantified impact of moisture ($AD_{\lambda E}$) and heat (AD_H) horizontal advection. Only the mean surface Bowen ratio (β_{surf}) is calculated from the model output. All the mean variables are values averaged over 10-hour period (from 7 UTC to 17 UTC) on 8 September 2009 for the six experiments.

Experiment	β_{sfc}	β_{entr}	$A_{\lambda E}$	A_H	$AD_{\lambda E}$	AD_H
ACM2	1.86	-1.55	-1.24	0.91	-0.29	0.18
MYJ	1.89	-1.18	-1.30	0.72	0.01	0.09
MYNN	1.67	-1.09	-1.45	0.84	-0.07	0.04
YSU	1.64	-1.54	-1.08	0.90	-0.32	0.07
MYNN-MP	6.42	-0.78	-8.48	1.02	0.15	0.02
YSU-MP	5.70	-0.86	-7.79	1.15	-0.05	0.08

The absolute value of the Bowen ratio at the entrainment ($|\beta_{entr}|$) is < 1 , while from NOAH simulation it is > 1 . Since negative values for $A_{\lambda E}$ indicate a mean influx of dry air from the free atmosphere in the PBL, this suggests that NOAH-MP exhibits a higher entrainment of dry air than NOAH. Since less moisture comes from the land surface and much more dry air is entrained in the PBL ($A_{\lambda E}$ with NOAH-MP is 5 times $A_{\lambda E}$ with NOAH, see Table 5), the PBL is drier in NOAH-MP than in NOAH. This explains the results displayed in section 3.4.1, where the difference obtained in humidity profiles between NOAH and NOAH-MP is up to 20%. Furthermore, comparing only the size and the slope of \mathbf{V}_{entr} vs \mathbf{V}_{sfc} for NOAH-MP and NOAH in the diagram, it can be seen that the drying effect of the free atmosphere (entrainment processes) has a stronger impact on PBL evolution than the moistening from land surface, in all simulations, especially when coupled with NOAH-MP.

Quantified impacts of the mean advected fluxes ($AD_{\lambda E}$ and AD_H) in the experiments with NOAH-MP do not exceed 0.1 significantly. Therefore, the impact of horizontal advection to the mean total flux, and subsequently to the PBL evolution at the study site simulated

with NOAA-MP is negligible, which can be also confirmed with the size of the \mathbf{V}_{adv} vectors.

3.5. Discussion

On 8 September 2009 between 7 and 9 UTC the simulated temporal change in absolute humidity within the PBL with the six experiments is not higher than 0.5 gm^{-3} , while the measured changes are ranging up to 3 gm^{-3} . Moistening of the PBL that was measured during the PBL growth can be explained by enhanced evaporation after the sunrise due to evaporation from the bare ground where the WVDIAL was located, and transpired water from the surrounding field of sugar beet that was within the 3 km range of the performed measurements (see section 3.1). Higher standard deviation of the measurements within the lower CBL in the morning hours (Figure 9a, b, c and Figure 10a, b, c) confirms the higher variability in humidity field within the range of averaging (white dashed rectangles in Figure 9). A small change in humidity during the PBL evolution simulated by the model in this study with all the six experiments, indicates that the evaporative fraction simulated by the model is lower than in reality. This can be related to the land surface heterogeneity, which is not captured by the model. The model categorizes the grid cell, which corresponds to the study site, as a cropland. In reality this was an open-pit mine surrounded by the agricultural landscapes, where most of the field were harvested apart from the one covered with sugar beet (see section 3.1). Categorization of the landscapes and phenological changes, which are recognized by the WRF model via green vegetation fraction (F_{veg}), determine the vegetation parameters such as leaf area index (LAI), albedo, roughness, emissivity, etc. These parameters are read from lookup tables in the LSMs. Therefore, model errors in F_{veg} or in land use will affect the results in the model representation of the fluxes at the land surface significantly (e.g. Nielsen et al., 2013).

3.5.1. Sensitivity to the PBL schemes

Results of the simulations differing in the PBL schemes have shown that the highest differences occur between the local and the nonlocal approach. The behaviour of the nonlocal schemes is very similar with respect to humidity and temperature profile

evolution, while among the two local schemes a spread among the results more pronounced.

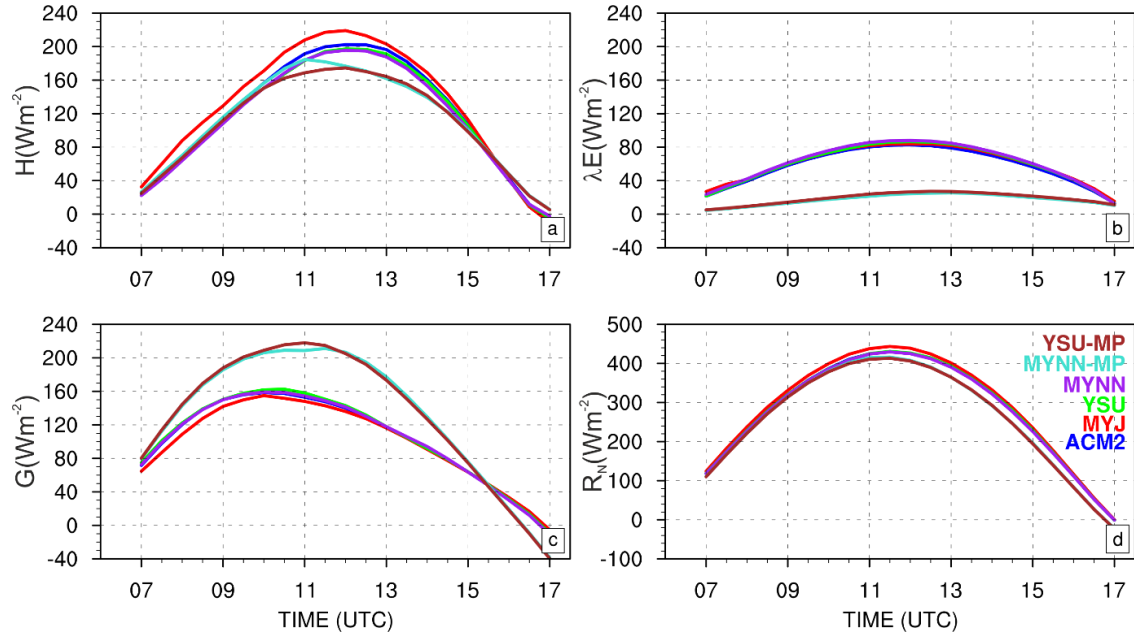


Figure 14. Simulations of the temporal change of (a) sensible heat flux (H), (b) latent heat flux (λE), (c) ground heat flux (G), and (d) net radiation flux (R_n) on 8 September 2009 from 7 to 17 UTC.

Figure 14 depicts simulations of the daytime temporal change of radiative and surface fluxes over a 10 hour period on 8 September 2009. H simulated with ACM2 is up to 10 Wm^{-2} higher than with YSU (Figure 14a), while λE is similar for both schemes (Figure 14b). This leads to a higher β_{sfc} , which implicates the stronger buoyancy force in the CBL simulated with ACM2. All the aforementioned points lead to the stronger mixing associated with ACM2 compared to YSU, which support the higher entrainment. This corresponds to the diagnosed values from the mixing diagrams (Table 5) which show that the similar or marginally higher mean entrainment of free tropospheric air into the CBL is simulated with ACM2. Even through these two schemes use different parameterizations of turbulent fluxes, the difference in the results for this dry case is negligible. This marginally higher mixing in the CBL can be related to the estimation of the PBLH, to which the nonlocal scheme are very sensitive. For this case WRF simulates a deeper CBL with ACM2 than with YSU, which adds a value to the aforementioned and corresponds to the results obtained by Xie et al. (2013).

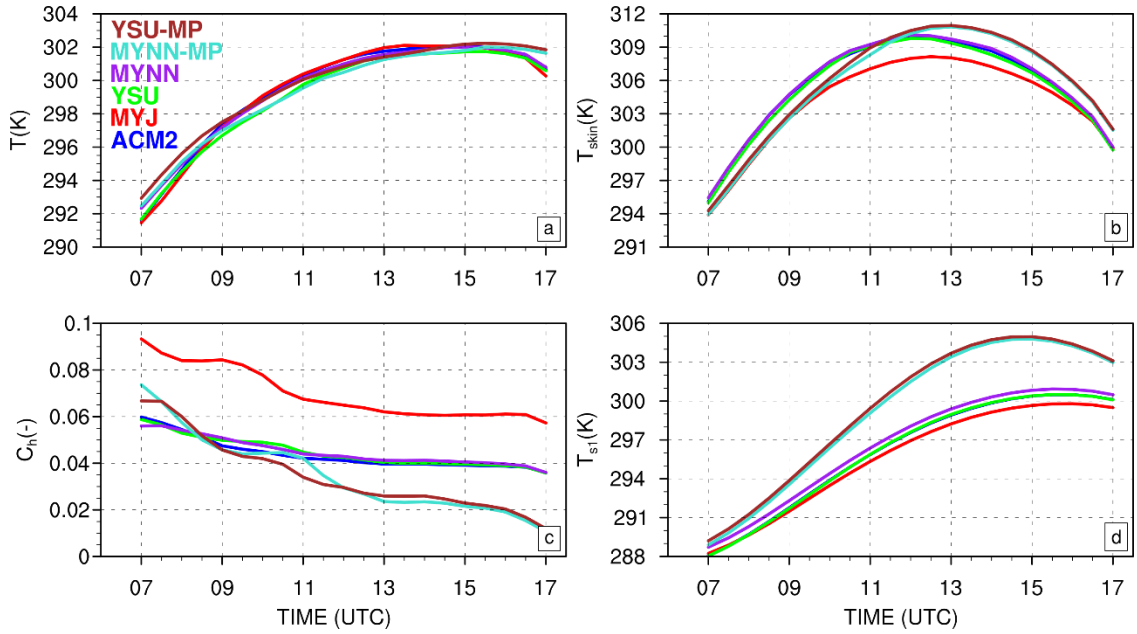


Figure 15. Simulations of the temporal change of (a) the temperature at the first model level (T), (b) the surface temperature (T_{skin}), (c) the surface exchange coefficient for heat and moisture divided by the friction velocity (C_h) and (d) the temperature in the first soil layer (T_{s1}) on 8 September 2009 from 7 to 17 UTC.

On the other hand, among the local schemes higher discrepancies can be seen in simulating the PBL evolution. One of the reasons is the fact that the WRF configuration with MYJ is fixed with respect to the surface layer scheme and needs to be coupled to the Eta similarity surface layer scheme, and MYNN with the revised MM5 surface layer scheme. This resulted in significantly higher values of C_h (Figure 15d) with MYJ (also obtained by Xie et al., 2013) and slightly lower T_{skin} . Therefore, up to $\sim 35 \text{ Wm}^{-2}$ higher H is obtained with MYJ, whereas values for λE are similar (Figure 14a, b).

This leads to a higher β_{sfc} with MYJ, which implies a stronger surface heating and consequently a greater generation of buoyant turbulence. This is visible from the faster PBL evolution in the morning hours with MYJ relative to MYNN (Figure 12a). But later in the afternoon growth of the PBL is constrained and the PBL with MYNN becomes higher. This is primarily related to the parameterization of the variables that mix heat and moisture within the PBL, such as l and K_h , and control TKE . Since turbulent fluxes of heat and moisture are proportional to K_h and consequently to l (see Eq. (8) and whole section 2.3.1), the higher l and TKE values would lead to stronger mixing of heat and moisture within the PBL. MYNN accounts for higher values for both l and TKE in the

afternoon (Figure 16 depicts an example profile for l and TKE valid at 16 UTC), and therefore the afternoon PBL evolves deeper with MYNN than with MYJ. Since in the MYNN PBL scheme the l and accordingly TKE is not constrained by the PBLH, like it is the case in the MYJ, it can be expected that the entrainment fluxes will be more realistic with the MYNN scheme than with MYJ. The mean entrainment of warm air from the free atmosphere is higher with MYNN, which was derived from the mixing diagrams (Table 5). This contributes to the higher PBLH with the MYNN scheme relative to MYJ.

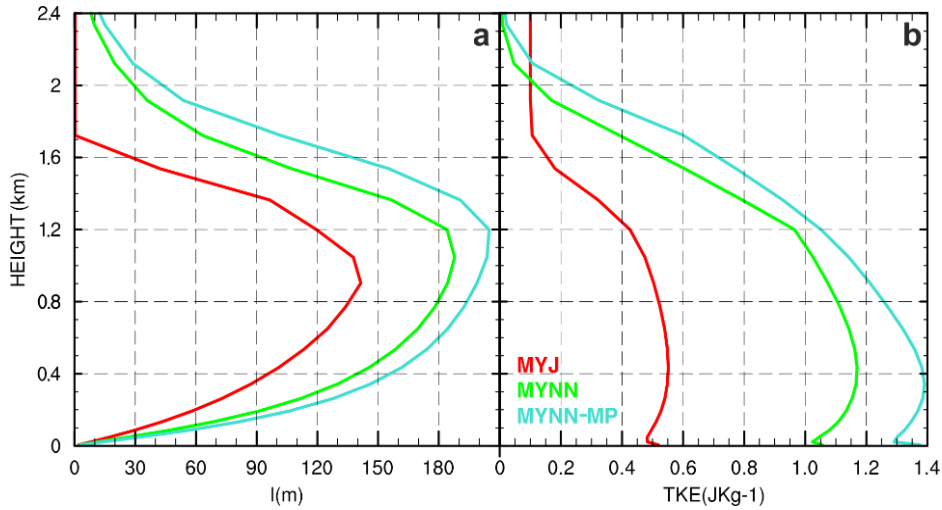


Figure 16. Vertical profiles of (a) the mixing length scale (l), and (b) TKE on 8 September 2009 at 16 UTC as simulated with WRF configured with the local MYN and MYNN schemes.

3.5.2. Sensitivity to the LSM

This case study shows a high sensitivity of WRF to the LSM choice in representing the PBL features and its evolution. NOAH-MP in its configuration for the model domain accounts for significantly lower λE (Figure 14b) and slightly lower H at the surface (Figure 14a) which corresponds to significantly higher β_{sfc} in the mixing diagram when compared to NOAH (see Table 5). The difference in H is related to the lower difference between T (Figure 15a) and T_{skin} (Figure 15b) in Eq. (4) as well as to the lower C_h obtained with NOAH-MP (Figure 15d). The high difference in λE is related also to the lower C_h (since in NOAH and NOAH-MP C_h is equal to C_q) used for the calculation of λE [Eq. (6)], but mostly to the different evaporative physics since soil moisture with NOAH-MP is marginally higher for this case than with NOAH (not shown). Furthermore, the

structural changes in communication between the LSM and PBL when the model is coupled to NOAH-MP is direct over land surfaces, and it does not go through the surface layer scheme like it is the case in WRF-NOAH (section 2.2.2). This may also contribute to this significant difference in the results, since in such a way WRF-NOAH-MP include more feedback between the deep soil and the land surface, which impact the evaporative physics close to the ground. The difference in R_n between NOAH and NOAH-MP is small, up to 20 Wm^{-2} (Figure 14d). This is due the difference in T_{skin} between NOAH and NOAH-MP (Figure 15b), since T_{skin} affects upward longwave radiation from Eq. (3). Furthermore, the residual energy from the difference in λE goes mostly into the ground as G (Figure 14c). G over vegetated and bare soil in both LSMs is calculated as in Eq. (5). The temperature gradient between the surface and the first soil layer ($T_{skin} - T_{s1}$) is lower with NOAH-MP than in NOAH (Figure 18d), which would result in a higher G if all the other variables in Eq. (5) would be equivalent for both LSMs. This leads to a conclusion that the significantly higher values of G obtained with NOAH-MP are predominantly due to the different method used for calculating the surface soil thermal conductivity κ_h , which is adjusted to the advanced “semi-tile” approach in NOAH-MP for calculating the energy balance at the land surface. This refers to the exponential decrease of κ_h with vegetation cover which is used in NOAH (Chen and Dudhia, 2001a), but in NOAH-MP it is removed. The difference in λE obtained here might also be due to an option in NOAH-MP related to calculation of the soil moisture factor, which is a function of matric potential in NOAH-MP, and in NOAH it is related to soil moisture η . Higher values for T_{skin} with NOAH-MP relative to NOAH is also partly related to the κ_h , which is used in the thermal diffusion equation (e.g. Chen and Dudhia, 2001a), but primarily to the technique used for its calculation. The iterative method in NOAH-MP that calculates T_{skin} over vegetated and bare ground separately is more physically consistent than the simple linearized approach in NOAH which yielded to a better agreement with observations in Niu et al. (2011). In this study higher T_{skin} was obtained with NOAH-MP than with NOAH as well.

The study shows that the higher β_{sfc} also affects the mixing features that are calculated in the PBL schemes. From the humidity profiles represented in section 4.1.2, we can conclude that the spread in the results between the simulations is due to the PBL switches in the morning hours, while in the afternoon the spread is wider and affected more by the land surface exchange, i.e. β_{sfc} . Higher mixing was simulated when the schemes were

coupled with NOAH-MP. The MYNN scheme, for example, accounts for higher l and TKE when is coupled with NOAH-MP than with NOAH (Figure 16), and this results in higher K_h and therefore in higher fluxes.

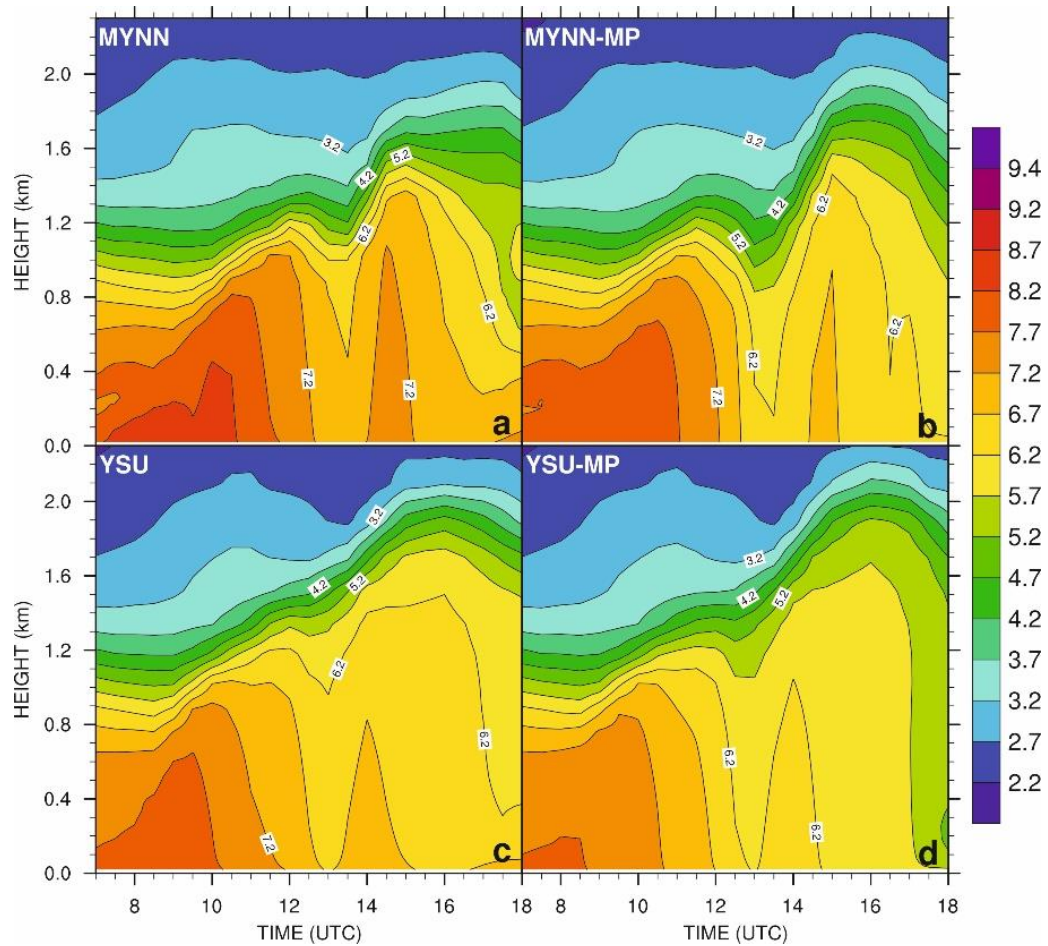


Figure 17. Temporal change of mixing ratio vertical profiles q in gkg^{-1} from 7 to 18 UTC on 8 September 2009 at the study site, as simulated with WRF configured with MYNN and NOAH (a), YSU and NOAH (b), MYNN and NOAH-MP (c), and YSU and NOAH-MP (d).

Figure 17 depicts a temporal change of the mixing ratio profiles between 7 and 18 UTC on 8 September 2009 at the study site for MYNN and YSU in combination with NOAH and NOAH-MP. The figure displays that drying in the whole CBL during the afternoon hours is more abrupt with NOAH-MP (Figure 17c, d) than with NOAH (Figure 17a, b). This can be also seen from the mixing diagram (Figure 13b), especially between 11 and 14 UTC. In the afternoon the $\lambda q/C_p\theta$ line in the mixing diagram is more sharply curved than in the morning, which indicates that the higher and more abrupt drying with

NOAH-MP is related mostly to the entrainment fluxes. In the morning, surface moisture and entrainment are more balanced, since the $\lambda q/C_p\theta$ line is less curved. This leads to a conclusion that the influence of the land surface is getting stronger toward midday, when the CBL is fully mixed, and extends all the way up to the interfacial layer. The latter demonstrates the strong sensitivity of the PBL schemes to the lower boundary conditions.

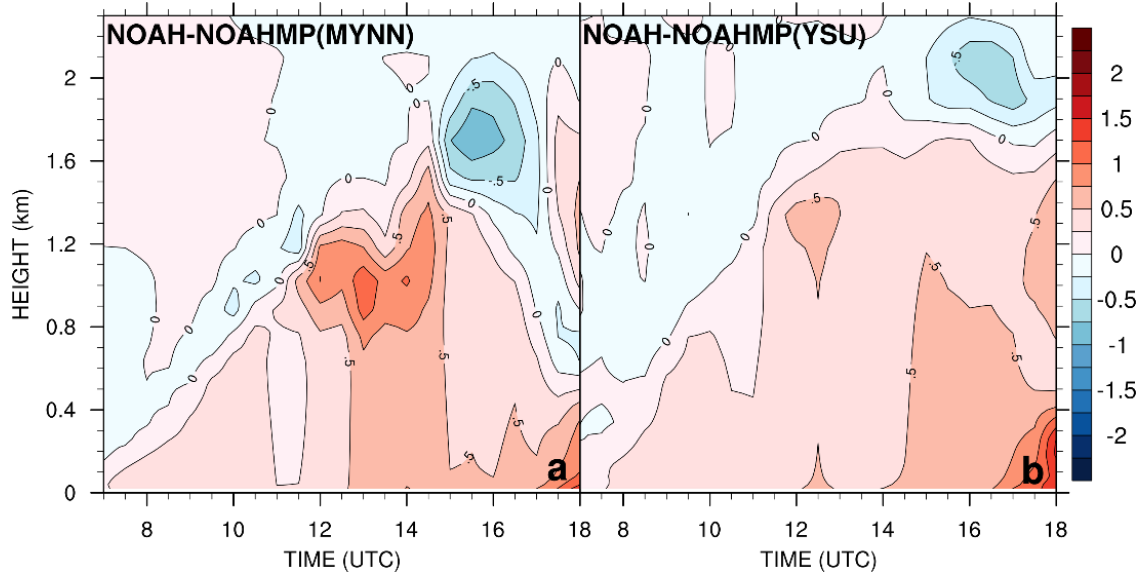


Figure 18. Temporal change of the difference between the NOAH and NOAH-MP mixing ratio profiles in gkg^{-1} for the simulations with MYNN (e) and YSU (f) PBL schemes.

The highest difference in β_{sfc} between NOAH and NOAH-MP is around midday (Figure 14) and Figure 18 shows that the highest difference between the humidity profiles obtained with these two LSMs range up to 1.4 gkg^{-1} and occurs 11 and 14 UTC in the upper part of the CBL. This can be explained with the fact that an increase in β_{sfc} (e.g. higher surface heating) supports stronger turbulent mixing caused mostly by buoyancy. Turbulence caused by wind shear is a main mechanism of mixing in the PBL in absence of radiative heating of the land surface (i.e. in the night and early morning), and less influenced by the ground. Therefore the stronger impact of the PBL schemes on the results is apparent in the morning. While at midday and in the afternoon, the mixing is strongly related to β_{sfc} and therefore the higher β_{sfc} will give the stronger mixing caused by buoyancy up to the CBL top and stronger entrainment of air from the free atmosphere. This corresponds to the values for $A_{\lambda E}$ and A_H (Table 5) diagnosed from the mixing diagram (Figure 13b).

Due to the higher difference in PBL humidity evolution between NOAH and NOAH-MP, from Figure 18 it can be concluded that WRF coupled with MYNN is more sensitive to the LSM choice than WRF with YSU. All the aforementioned implies that land surface processes are highly influential on mixing properties within the PBL and also processes at the interfacial layer in dry weather conditions. Furthermore, the variability in moisture profiles and lower atmospheric conditions among the experiments suggest a strong impact of the model configuration on the simulations of cloud formation and precipitation.

4. Convective case study

In this section the WRF sensitivity to PBL and LSM parameterizations in representing CI and precipitation is assessed using the six experiments (Table 1). The chosen date for the analysis is 25 August 2009, when strong convective precipitation was observed in southwest Germany. More details about the studied location and weather conditions are given in section 4.1. The dry-case analysis that was based on the results at the single point, in this case study is extended to the spatial intercomparisons between the simulations over a wider area. Results are introduced in section 4.3 and discussed in section 4.4.

4.1. Study area

The study area is located in southwest Germany, between $\sim 48\text{-}50^\circ$ N and $\sim 8\text{-}11^\circ$ E (The red square in Figure 19). The boundary zone of the study area was carefully defined to allow a reasonable spatial margin from the edges of the inner domain, in order to exclude any possible distortions due to the lateral boundary forcing from the outer domain. A minimum of 23 grid cells (i.e. 46 km) was taken as the margin from the southern edge of the inner domain. Most of the area covers Swabian Alb (SA), only in its north and northwest part the Upper Rhine Plane is captured as well. It has been selected to include two study locations of the RU 1695 project, Kraichgau and Nellingen.

These sites were located in two regions with considerable differences in climate conditions. The first site ($48^\circ 55' 38''$ N, $8^\circ 42' 57''$ E, at 314 m above sea level) is situated north of the city Pforzheim in the hilly Kraichgau (KC) region. It is a fertile loess district covered with crops, with a mild climate where mean annual temperature is 9.3°C and mean annual precipitation is 777 mm. The second site ($48^\circ 31' 39''$ N, $9^\circ 43'$ E, at 690 m above sea level) is located close to a small village Nellingen in SA region. It is a mountainous plateau with colder and wetter climate. Mean annual temperature is 6.5°C and mean annual precipitation is 962 mm. The share of agricultural land from the total area is very similar in both regions, but in the KC region most of the agricultural land is converted into cropland, while in SA the share of grassland is nearly equal to the share of croplands (Gayler et al., 2014; Wizemann et al., 2015). Silty clay loam is the prevailing top soil texture in the SA region, while at the KC site it is silty loam (Wizemann et al.,

2015). On 25 August 2009 the KC site was cultivated with maize, while the field at the SA site was already harvested.

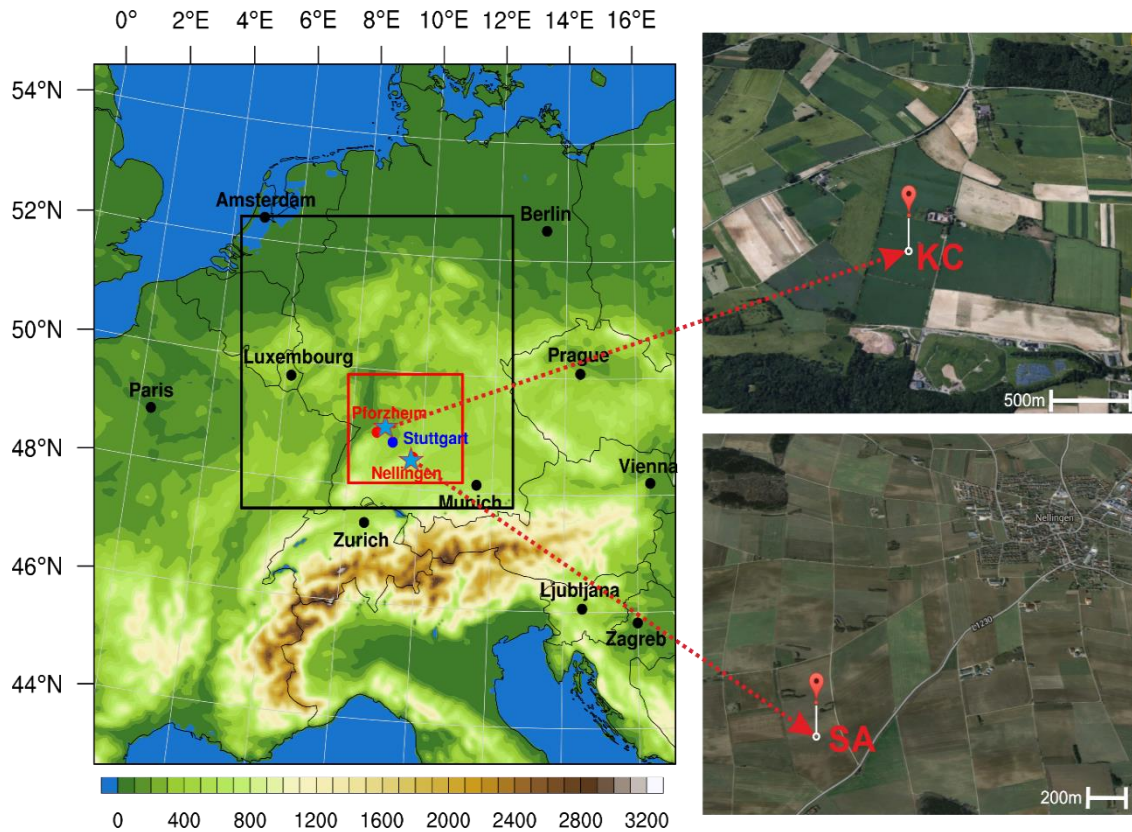


Figure 19. The model domains with the orography field (left panel), with the study area (the red square). The site locations are given in blue stars. More detailed with field management around the Kraichgau (KC) station (upper right panel) and the Swabian Alb (SA) station (bottom right panel).

4.2. Case description

The weather in most of Europe on 25 August 2009 was influenced by a high over eastern Europe and a North Atlantic low pressure system (Figure 20a). In the central Europe surrounded by these two systems, warm air in south and southwest airflows was moving northward. A frontal system on the edge of the North Atlantic low, was progressing slowly eastward (Figure 20b), bringing significantly cooler and more moist air over the heated surfaces, causing strong local instabilities. Already in the early morning rain, local showers and thunderstorms were observed in western Germany close to the border with Belgium and Netherlands.

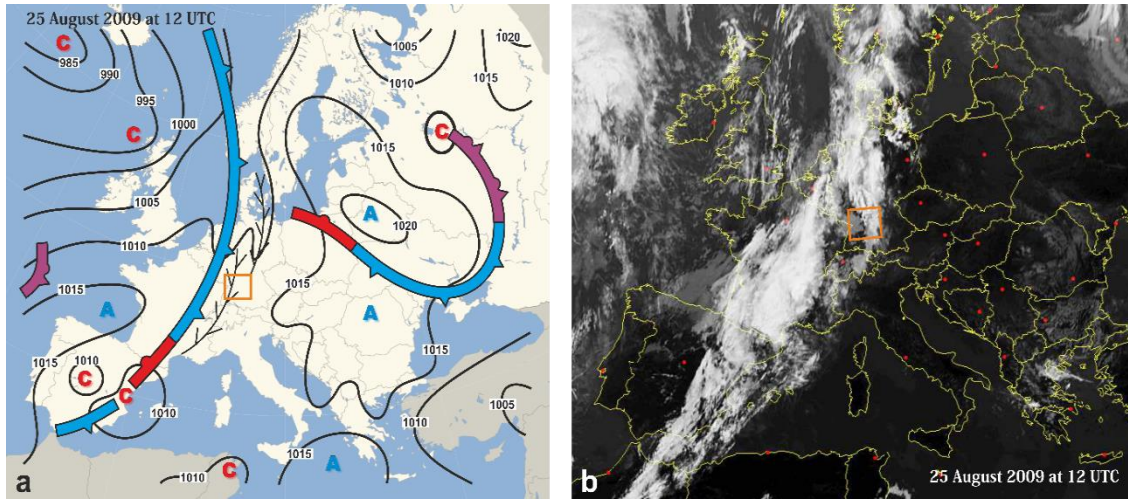


Figure 20. Synoptic weather map (a) and the satellite image of clouds over Europe (b) on 25 August 2009 at 12 UTC. The orange square show the location of the study area. The source – DWD¹/EUMETSAT².

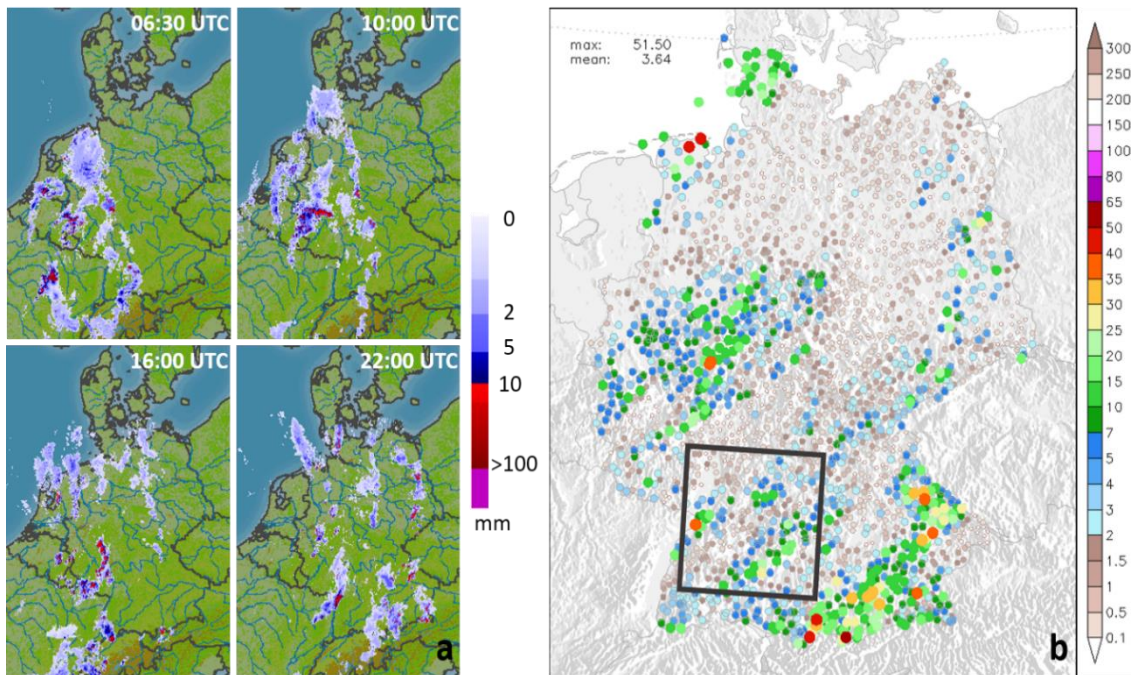


Figure 21. Radar images of rainfall at 6:30 UTC, 10 UTC, 16 UTC and 22 UTC (a), and the 24 hour precipitation on 25 August 2009 (b) as observed on the DWD weather stations. The black box shows the boundaries of the analysed domain. The source – DWD.

¹ Deutscher Wetterdienst – The German Meteorological Office

² European Organisation for the Exploitation of Meteorological Satellites

At midday local showers and thunderstorms were observed in southern Baden-Württemberg and western Bavaria (Figure 20b and Figure 21a). At places, heavy rain, high winds and hail were observed as well. In the afternoon, showers and thunderstorms were making slowly their headway further to the east, following the frontal system path. In the evening particularly affected regions were Sachsen-Anhalt, southern Brandenburg, Thuringia and Saxony, with strong showers and thunderstorms until midnight (Figure 21a).

The regions first covered with clouds and with earliest precipitation onset were W and NW Germany, having the maximum daily temperatures mostly ranging from 19 to 22°C. Central and SW Germany were measuring 23 to 28°C, while temperatures up to 32°C were observed in the eastern part of Germany, where the weather deterioration came later in the afternoon and early evening. The rainfall was observed on most of the DWD stations during the day (Figure 21b). A maximum 24 h accumulated precipitation of 51.5 mm was measured on the station in Garmisch-Partenkirchen located at the far south end of the country. Within the study area, denoted as the black square in Figure 21b, the maximum precipitation observed was 39 mm.

4.3. Results and discussion

Land surface inhomogeneities, convergence zones and PBL moisture have a strong influence on triggering and sustaining the DMC. Inhomogeneities in soil moisture, soil temperature and vegetation at the land surface control heat and moisture fluxes, which have a strong impact on the PBL evolution, cloud formation and precipitation. Water vapour in the PBL, necessary for cloud formation and CI, is advected by mesoscale or/and synoptic scale motions, and locally transported from underlying land surface by local mixing. Soil moisture inhomogeneities and vegetation influence lower atmospheric conditions with respect to heat and moisture, and consequently the formation of convergence zones (e.g. Klüpfel et al., 2012), which are preconditions for CI (e.g. Khodayar Pardo et al., 2009; Wulfmeyer et al., 2011; Klüpfel et al., 2012) and therefore precipitation (e.g. Findell and Eltahir, 2003a; Koster et al, 2006; Betts, 2009; Seneviratne et al., 2010).

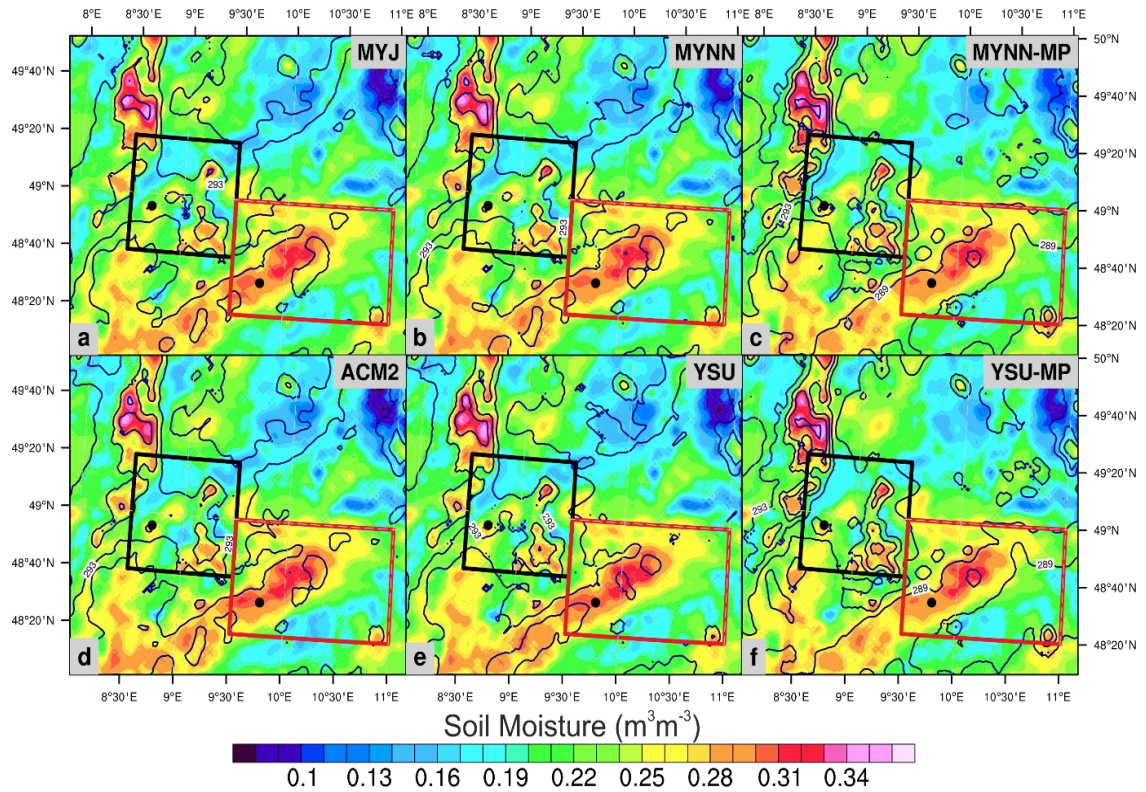


Figure 22. Horizontal distribution of soil moisture content in m^3m^{-3} (shaded) in the first 10 cm of soil on 25 August 2009 at 6 UTC as simulated with the 6 experiments. The overlaid lines denote soil temperature (K) in the same soil layer over the study area, with contour interval of 2 K. The black and red boxes denote boundaries of the R1 and R2 regions, respectively.

Figure 22 depicts the simulations of horizontal distribution of the initial soil moisture content in m^3m^{-3} at 6 UTC within the first 10 cm of the soil at the study area. A thorough analysis is executed over two selected regions R1 and R2. The regions are chosen to capture the two RU 1695 sites, and to include the most of the 24 h accumulated precipitation simulated on the selected date (Figure 24). The first region R1 (black box in Figure 22) is located between $8^{\circ}30'$ and $9^{\circ}30'$ E and $48^{\circ}40'$ and $49^{\circ}20'$ N. This region captures the KC site, and comprises 33×56 grid cells. The second region R2 (orange box in Figure 22) incorporates the hilly region of Swabian Alb together with the SA site. This region covers 34×39 grid cells and is located in the southwest part of the study area between $9^{\circ}30'$ and 11° E, and $48^{\circ}20'$ and 49° N.

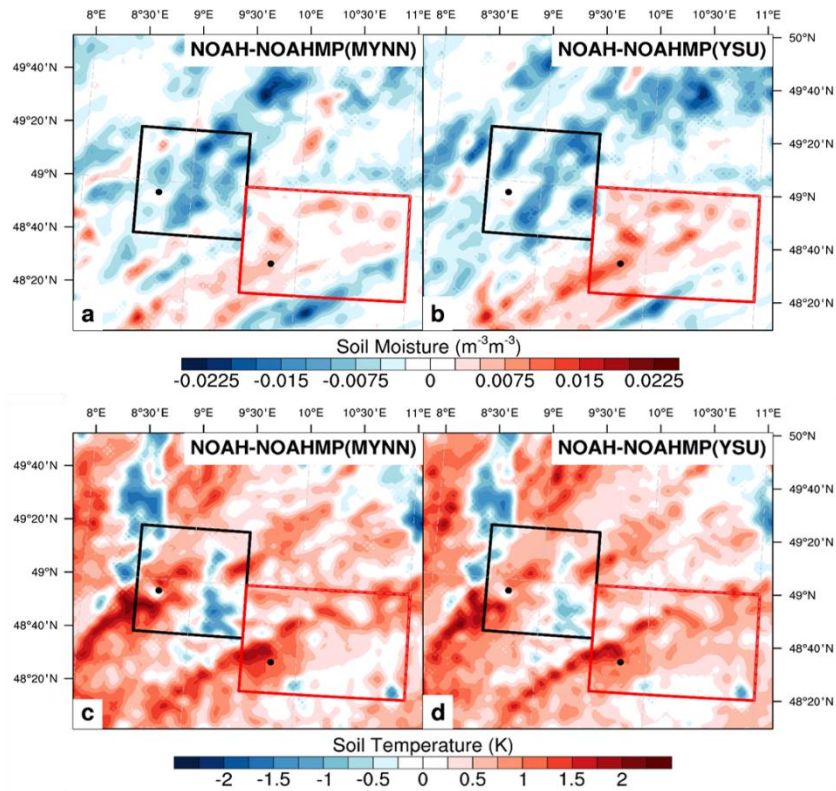


Figure 23. Differences in simulated soil moisture in the top soil layer in (m^3m^{-3}) between NOAH and NOAH-MP coupled with MYNN (a) and YSU (b); differences in simulated soil temperature in the top soil layer in (K) between NOAH and NOAH-MP coupled with MYNN (c) and YSU (d). The results are valid on 25 August 2009 at 6 UTC over the analysed area.

The difference in soil moisture between the two regions is apparent from Figure 22. Overall lower soil moisture is simulated in R1 relative to R2. There is no significant variability in soil moisture and soil temperature between the simulations due to different PBL schemes. Differences between the two LSM in the simulated soil moisture and soil temperature in the top soil layer is depicted on Figure 23. Soil moisture is higher in R1 and lower in R2 with NOAH-MP relative to NOAH, and the variability between the LSMs is up to $\sim 2\%$. In both regions mostly higher top soil temperature at 6 UTC is simulated with NOAH, and the maximum difference between the LSMs is 2 K.

In the following sections the six simulations (Table 1) of accumulated precipitation and cloud evolution, surface wind, temperature and moisture, as well as the PBL features, such as moisture and temperature profiles, are intercompared (sections 4.3.1 – 4.3.5). Land surface – atmosphere coupling in the model is assessed with the mixing diagram approach in section 4.3.6.

4.3.1. Accumulated precipitation

Observations of the rainfall suggest that a frontal system brought rain, local showers and thunderstorms at first in the western Germany, and later in the afternoon, as the front was moving slowly eastward, rainfall was observed more easterly, capturing the Swabian Alb area. This sequence of events was reproduced by the WRF simulations as well, but the strength and location of the rainfall vary with the selected parameterization.

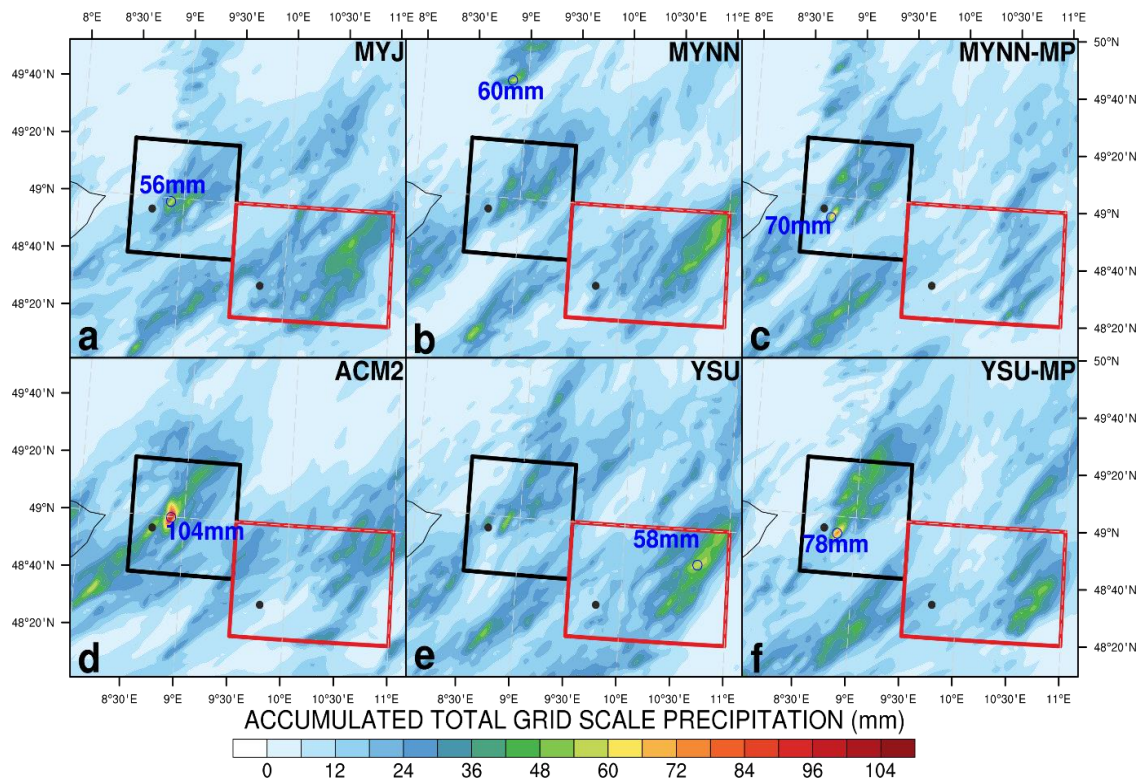


Figure 24. Accumulated rain in mm over 24 h period on 25 August 2009 within the study area as simulated with the 6 experiments. The simulated locations and amount of maximum precipitation are denoted in blue letters, and in black dots are locations of RU 1695 measurements sites. Boxes as in Figure 22.

The spatial representation of accumulated precipitation over 24 hour period, from 6 UTC 25 August to 6 UTC 26 August 2009 as simulated with the six experiments is displayed in Figure 24. Different patterns on the plot show that the choice of parameterizations influences significantly both the location and intensity of precipitation in the selected area. From the maximum rainfall denoted in blue numbers in Figure 24, it is apparent that the highest maximum of 104 mm is simulated with ACM2, which is almost 100% higher than the values simulated with the other three PBL schemes coupled with the NOAA

LSM (Figure 24a, b, d, e). The location and strength of the maximum rainfall is affected by the LSM choice as well. NOAH-MP increases the maximum for 10 mm when WRF is coupled with MYNN (Figure 24b, c), while with YSU-MP the maximum rainfall is 20 mm higher than with YSU (Figure 24e, f). Furthermore, in both cases the location of the maximum rainfall is shifted. This indicates ACM2 simulates the deepest convection among all the experiments, which will be shown in the following analysis. Overall, the location of the maximum rainfall is simulated in R1 with MYJ, ACM2, MYNN-MP and YSU-MP, while with YSU it is in R2. MYNN simulates the maximum outside of the both regions. Even though the simulated location and pattern of accumulated 24 h precipitation differ among the experiments, all 6 of them simulate enhanced rainfall rate in both regions. Therefore, these two regions are chosen for the analysis of the convection and precipitation.

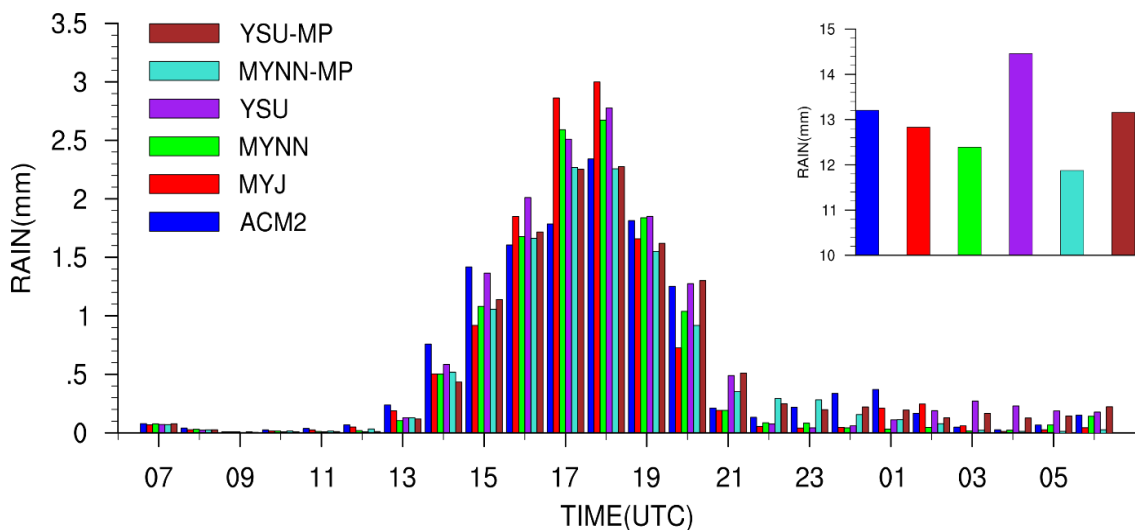


Figure 25. Hourly accumulated precipitation in mm on 25 August 2009 averaged over the study area. In the upper right corner the areal mean of the accumulated 24 h precipitation for the each experiment.

Figure 25 shows the hourly values of the accumulated precipitation averaged over the whole study area. All 6 experiments simulate the values over 0.5 mmh^{-1} are simulated between 14 and 20 UTC. The maximum hourly difference in precipitation between the experiments is $\sim 1.2 \text{ mmh}^{-1}$, which occurs between ACM2 and MYJ at 17 UTC. Overall higher precipitation rate per hour is simulated when the model was coupled with NOAH than with NOAH-MP. The accumulated 24 h precipitation averaged over the whole study

area (the upper right corner of Figure 25) shows the highest values with YSU and the lowest with MYNN-MP.

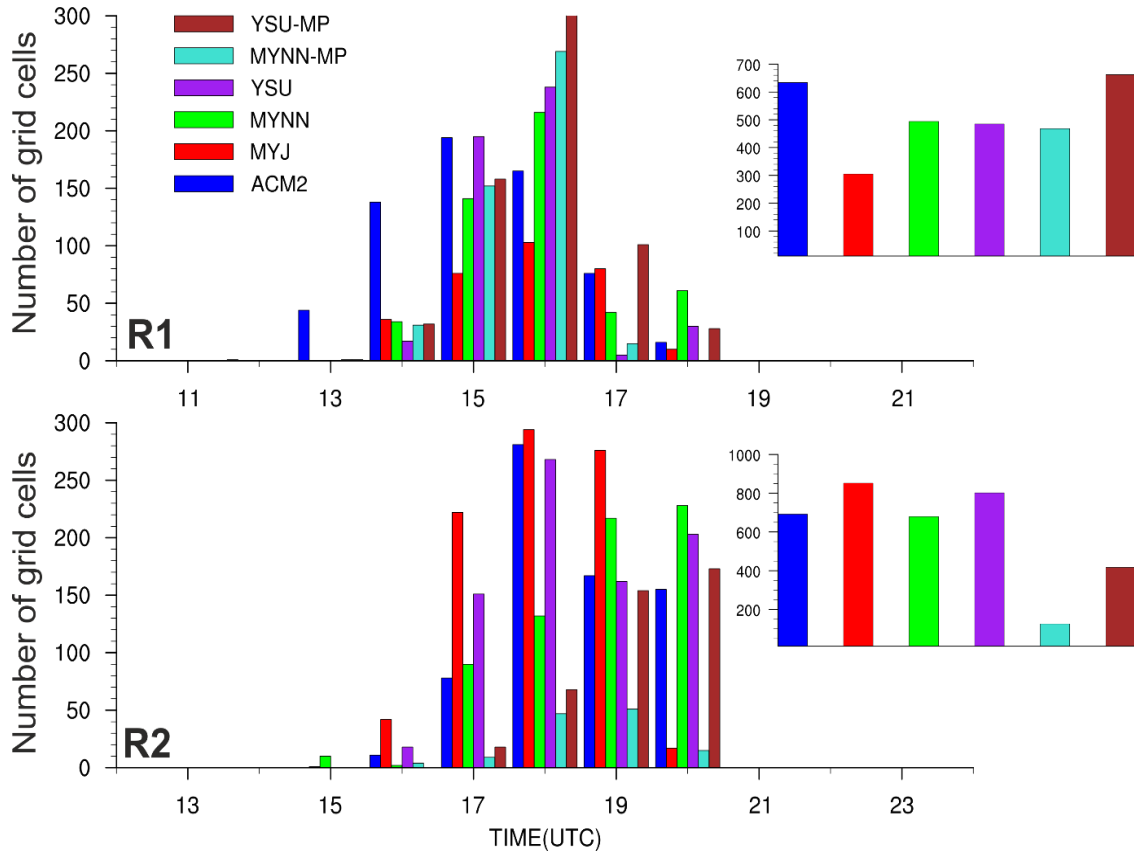


Figure 26. Number of grid cells with hourly precipitation $> 10 \text{ mmh}^{-1}$ on 25 August 2009 within R1 (a) and R2 (b). Total number of grid cells with hourly precipitation $> 10 \text{ mmh}^{-1}$ are placed in the upper right corner of the each panel.

To extract strong precipitation events, the number of grid cells with precipitation exceeding 10 mmh^{-1} over the two study regions is given in Figure 26. The results demonstrate that the highest number of strong precipitation events in the R1 region (Figure 26a) is simulated between 14 and 18 UTC. Only ACM2 simulates the strong precipitation onset one hour earlier. The highest spatial spread with strong precipitation events (evaluated with the number of grid cells with the hourly precipitation $\geq 10 \text{ mmh}^{-1}$) is simulated with YSU-MP and ACM2, while the least number of grid cells is simulated with MYJ. In this region, NOAH-MP does not have a strong influence on the results in the MYNN experiments, while when coupled with YSU, NOAH-MP increases the spread of the strong precipitation events significantly.

In the R2 region (Figure 26b) the difference between NOAH and NOAH-MP is higher than in R1. Strong precipitation events are simulated over substantially lower number of grid cells with NOAH-MP relative to NOAH. This may suggest that in this case, NOAH-MP decreases significantly the number of grid cells with simulated DMC occurrence over R2. The highest spatial spread of the strong precipitation events is simulated with MYJ. Most of the experiments simulate the strong precipitation from 16 to 20 UTC, with an exception of MYNN, which simulates the onset at 15 UTC.

The selected parameterization affects not only the location and pattern of precipitation, but also the time when the maximum occurs (Figure 27). The 2 hours difference among the experiments is simulated in R1, and 3 hours in R2. 5 experiments simulate stronger precipitation in R1, only MYJ gives the hourly maximum in R2. In R1 the strongest precipitation event of 47.2 mm is simulated with ACM2. Furthermore, in R1 the spatial spread between the locations with the maximum hourly rainfall is small among the simulations. In R2 most of the experiments simulate the strongest precipitation in the SE part of the region, only ACM2 and MYNN shift the location northward and north-eastward, respectively.

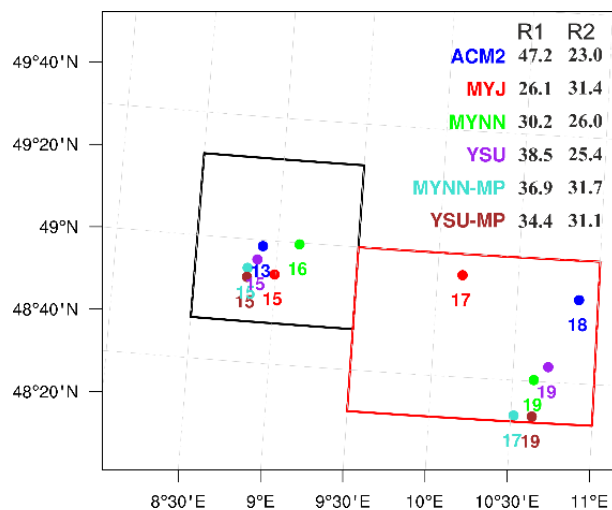


Figure 27. Locations of the maximum hourly precipitation on 25 August 2009 within R1 (black box) and R2 (red box), with the simulated time of occurrence in UTC hours, denoted in colours corresponding to the experiments. The amounts of the maximum precipitation for the both regions in mmh^{-1} are given in the upper right corner.

4.3.2. Clouds

Radiation at the top of the atmosphere (TOA) indicates whether clouds are present or not. Furthermore, the radiation values allow for differentiating shallow from deep convective clouds. Figure 28 shows deep convective clouds already present at 12 UTC with ACM2, MYJ, MYNN and MYNN-MP. On the other hand, the two YSU experiments simulate clouds in R1 one hour later (Figure 28e, f). The YSU-MP experiment simulates the convection initiated within the R1 region, while at the same time the figure suggests that with YSU clouds are mostly advected from the west. Consequently, the YSU-MP experiment simulates a significantly stronger isolated precipitation in R1 compare to YSU, which is evident from Figure 24e and Figure 24f, as well as in Figure 26a.

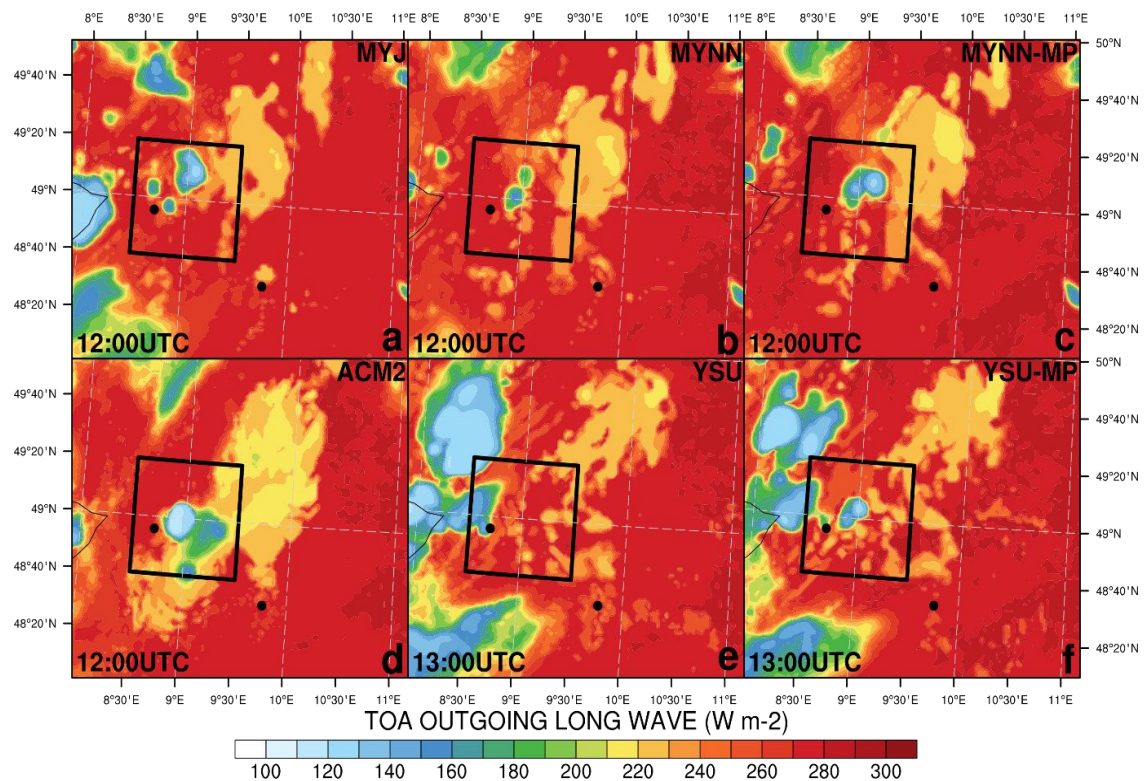


Figure 28. Radiation at the top of the atmosphere (Wm^{-2}) as simulated with the experiments on 25 August 2009 at the time denoted in the lower left corners of the each panel. The R1 region is enclosed with the black box. The experiment names are denoted in the upper right corners of the each panel.

The TOA radiation in R2 at 15 UTC for the later afternoon precipitation event as described in section 4.3.1 is depicted in Figure 29, with the black box denoting boundaries of R2. Simulated cloud patterns differ among the experiments here as well – most of the

experiments simulate more cumulus and stratocumulus like clouds in the NW part of R2, only ACM2 predicts more uniform altostratus and status like cloud. With MYJ and MYNN experiments the locations with low values or the TOA radiation at 15 UTC indicate that a deep convection was initiated within R2, which might be induced by orography within the region. This is not evident from the simulations of the remaining experiments, which suggests that the convective clouds are mostly advected into the region from the west.

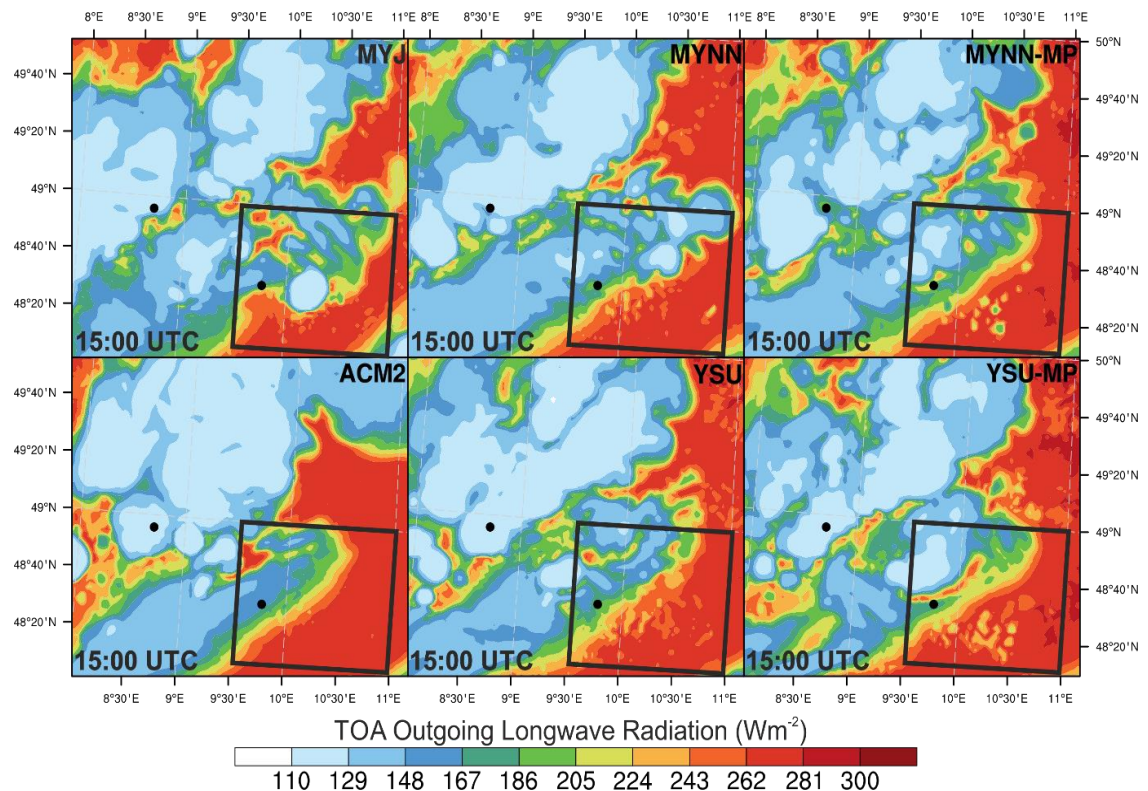


Figure 29. As in Figure 28 at 15 UTC, with R2 denoted in black boxes.

4.3.3. Atmospheric conditions in the lower PBL

The initiation of convection depends on the conditions close the land surface (e.g. Trier et al., 2003; Roundy et al, 2013). Particularly important for CI is low level moisture and temperature gradients, as well as wind convergence zones (Wulfmeyer et al., 2014a) if exist. A horizontal distribution of mixing ratio at the first model level at the time prior to the simulated precipitation onset in R1 (i.e. 11 UTC) is displayed in Figure 30.

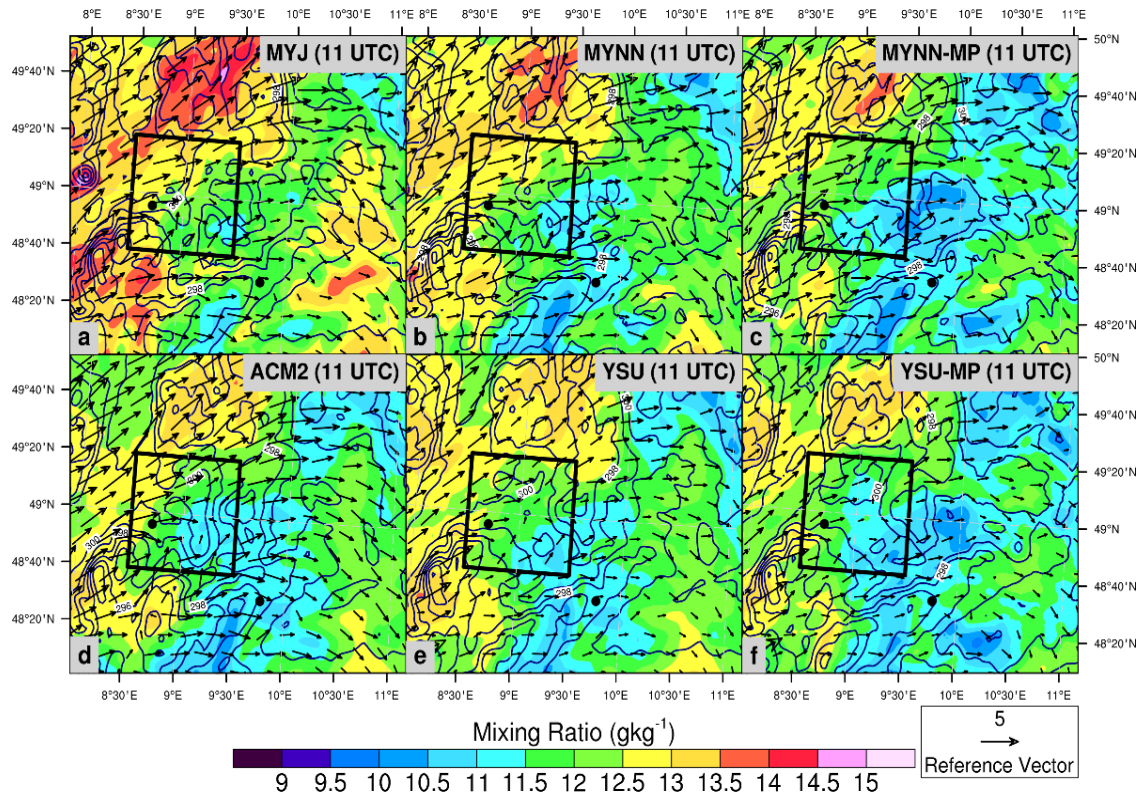


Figure 30. Horizontal distribution of mixing ratio in gkg^{-1} (shaded) with overlaid wind vectors (ms^{-1}) and temperature lines with contour interval of 2 K (navy blue lines) as simulated at the first model level on 25 August 2009 at 11 UTC.

The figure shows that all experiments account for increased moisture west from the R1 region. MYJ simulates highest moisture close to the ground (Figure 30a), with the difference rising up to $\sim 3 \text{ gkg}^{-1}$ relative to the remaining 5 experiments. ACM2, YSU and YSU-MP (i.e. the nonlocal experiments) simulate drier conditions close to the ground than the local experiments (i.e. MYJ, MYNN, MYNN-MP). In most of R1 drier conditions at the lowest model level are simulated with NOAH-MP relative NOAH. All simulations predict mostly weak to moderate SW horizontal wind.

Overlaid lines of temperature at the lowest model layer show the presence of strong temperature gradients SW from the R1 region simulated with all experiments, which indicates an intrusion of colder air in the SW flow. This coincides with the location of the cloud development with MYJ, YSU and YSU-MP showed in the previous section.

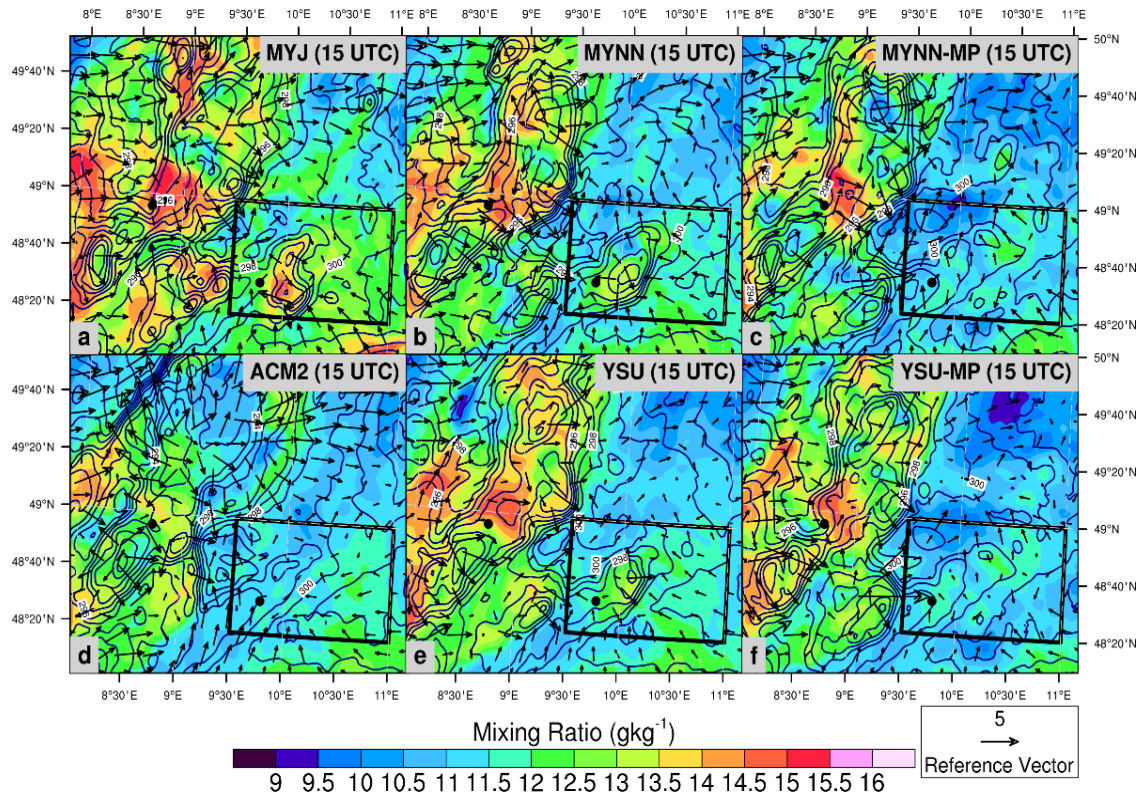


Figure 31. As in Figure 30 at 15 UTC, with R2 region denoted in the black boxes.

Figure 31 depicts moisture, temperature and wind simulations at the lowest model level at 15 UTC. Most of the experiments simulate higher moisture and lower temperatures in the western part of the whole study area, whilst the eastern part is less humid and warmer. In the R2 region (within the black box in Figure 31), MYJ simulates the highest moisture at the selected time step (Figure 31a), while the lowest part of the atmosphere is the driest with ACM2 among the NOAH experiments. This indicates that with ACM2 a stronger low level drying is simulated between 11 and 15 UTC when compared with the remaining NOAH experiments. When comparing the results of the two LSMs, NOAH-MP predicts drier conditions close to the ground than NOAH. The NOAH experiments simulate an influx of more moist air in the SE flow into the R2 region, and it is the strongest with MYJ. This is not as pronounced in the two NOAH-MP simulations. The simulated horizontal wind is stronger with the local experiments, especially with MYJ. Therefore, an influx of colder and more humid air from the west and southeast into R2 is the strongest with MYJ.

4.3.4. Vertical cross-sections

When the convection is initiated, the vertical wind component is typically increased, and moisture from the lower atmospheric levels starts to be transported upwards. Therefore strength of the convection and subsequently the amount of precipitation is strongly related to the updraft strength. The stronger the updraft, the moisture penetrates more easily deeper in the atmosphere, and consequently likelihood for the DMC to occur is higher. In the following two figures cross-sections of precipitable water with overlaid solid lines of vertical velocity are depicted to investigate cloud development and the depth of the resulting convection at times when the maximum hourly rainfall is simulated within the analysed R1 and R2 regions.

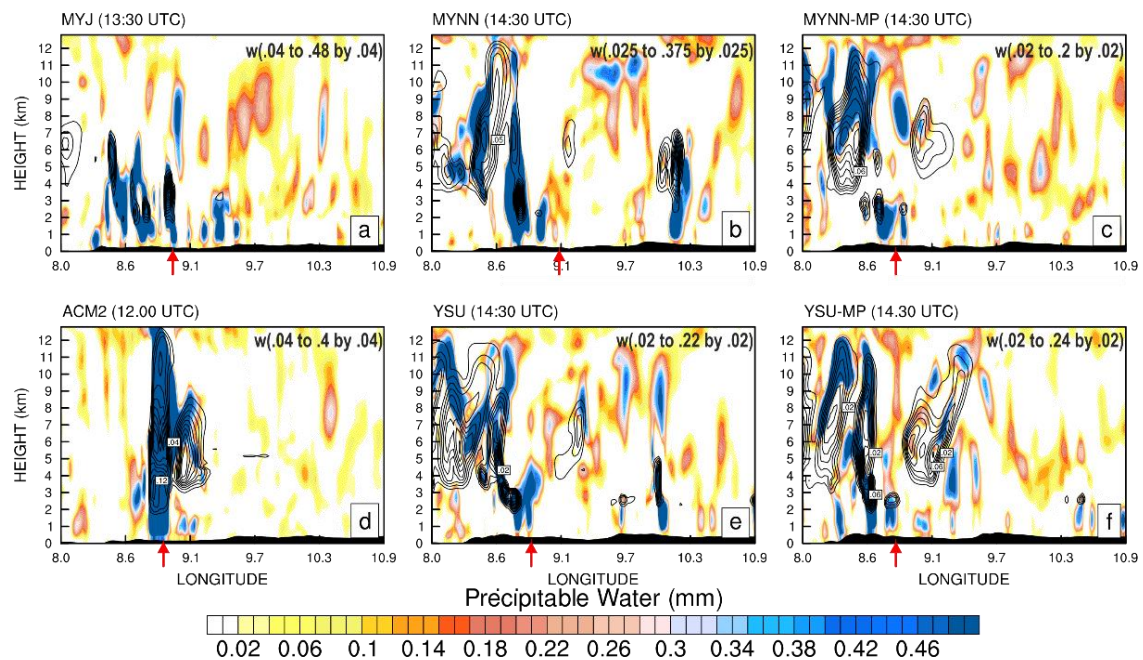


Figure 32. Vertical cross-sections of precipitable water in mm (shaded) and vertical wind velocity in ms^{-1} (solid black lines) on 25 August 2009 along the horizontal lines through the locations with the maximum hourly precipitation in R1 (shown in Figure 27 at times prior to the maximum precipitation event which is denoted in upper left corners of the panels). Red arrows denote the exact locations with the hourly maximums.

Figure 32 depicts the cross-sections along the horizontal lines through the locations with the maximum rainfall within R1 as denoted in Figure 27. It is immediately apparent that ACM2 transports the moisture to the highest atmospheric levels, which corresponds to the deepest convective clouds (Figure 32d) and the strongest updraft. Generally, the

nonlocal experiments simulate deeper convection within R1, while with the local schemes at the selected locations the convection is more shallow and patchy. With MYJ low level moisture is lifted up to ~ 5 km, which is the shallowest among the experiments. The updrafts are increased above the PBLH and the strongest are simulated with ACM2 and YSU-MP, which is close to the locations with the maximum rainfall (red arrows in Figure 32d, f).

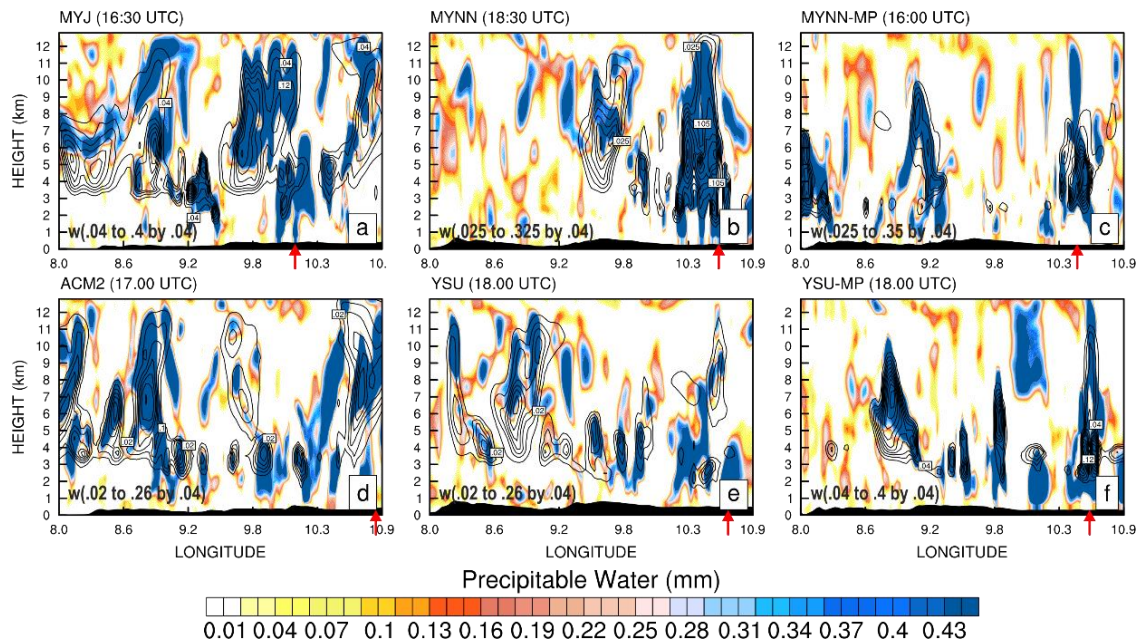


Figure 33. As in Figure 32, but along the horizontal lines through the locations with the maximum hourly precipitation in R2.

Figure 33 shows the cross-sections along the horizontal lines through the locations of maximum rainfall as simulated in R2 (right from 9.5°). In this region the maximum rainfall is simulated with MYJ. From Figure 33a it is evident that also here MYJ simulate more shallow clouds than e.g. the MYNN experiment for the selected event. ACM2 and YSU give more patchy convective activity within R2. Furthermore, less convective clouds are obtained with the NOAH-MP experiments when compared to NOAH. This corresponds to the smaller spread of strong precipitation events which is smaller with NOAH-MP than with NOAH as denote in Figure 26.

4.3.5. Vertical profiles

Temperature and humidity profiles are assessed via *SkewT-logp* diagrams, which show averaged profiles over the grid cells with simulated moderate to strong rainfall (Figure 34 and Figure 35). The threshold is set to 30 mm within 5 hour period for the analysed regions. The figures show the profiles at 6 UTC and at times prior to the strong rainfall onset. Morning profiles are important for the convection since they regulate the PBL response to the land surface fluxes, and therefore have a strong impact on the diurnal CBL evolution, which impacts CI and its characteristics (Ek and Mahrt, 1994; Findell and Eltahir, 2003a).

Within the R1 region, the T_v profiles in Figure 34a shows that the low atmosphere in the morning is colder with YSU-MP and warmer with ACM2. From the T_d profiles it is apparent that significantly drier atmospheric conditions between 1 and 3 km are simulated with ACM2 and MYNN experiments. With MYJ, YSU, MYNN-MP and YSU-MP a strong residual layer appears at heights between 0.5 and 1.2 km, and it is the driest with YSU. On the other hand, the residual layer is significantly weaker with ACM2 and MYNN. The characteristics of the residual layer are important for the CBL evolution, since it will be incorporated in the CBL afterwards, and it has an impact on the characteristic of the capping inversion that is about to be formed (e.g. Findell and Eltahir 2003a). These characteristics affect the strength of entrainment and the buildup of moist static energy within the CBL, which is a precondition for the DMC (Ek and Mahrt, 1994; Findell and Eltahir 2003a, Betts, 2009). Therefore, the simulated residual layer indicate that the inversion at the CBL top may be the weakest with ACM2 and MYNN, and higher entrainment can be expected. The afternoon profiles in Figure 34b indicate that the highest CBL at 11 UTC is simulated with ACM2, and the lowest with the local schemes. The most humid CBL is simulated with MYJ, and the driest with ACM2 and YSU. Significantly stronger moisture gradient at the top of the CBL is simulated with ACM2 relative to the remaining experiments, which can be related with the dry air entrainment. The NOAH-MP experiment decrease the PBLH when compared to NOAH, and predicts marginally less moisture within the CBL. The CAPE with YSU-MP is significantly decreased relative to YSU, while in the MYNN experiments the discrepancies in CAPE due to the LSM selection are not as pronounced.

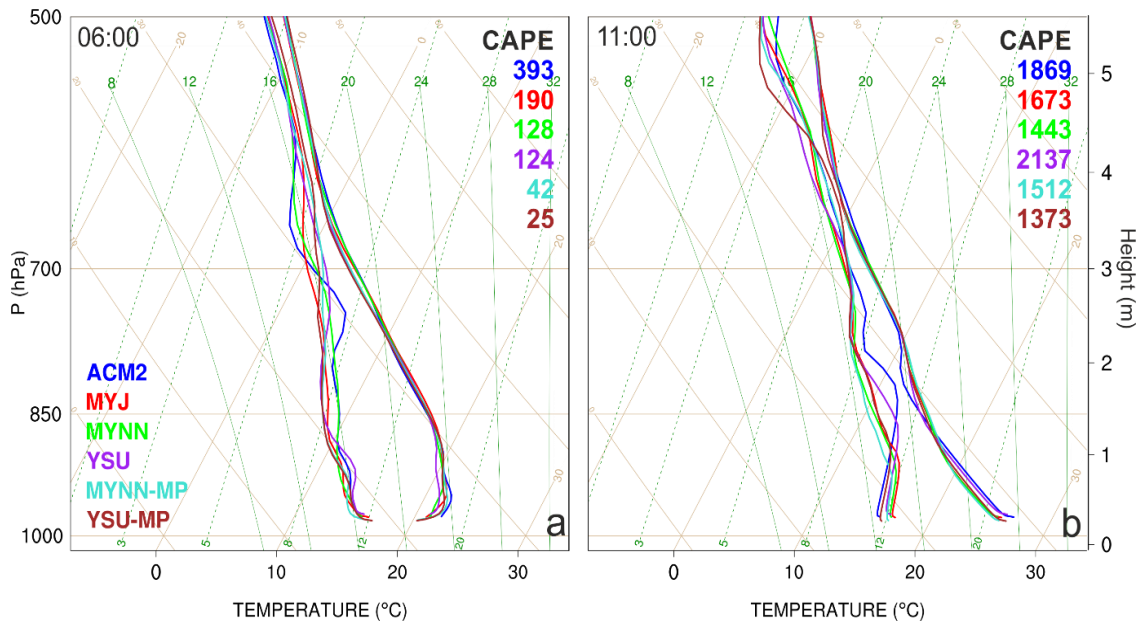


Figure 34. Simulated profiles of virtual (right profiles) and dew-point temperature (left profiles) in the SkewT – log p diagram on 25 August 2009 at 6 UTC (a) and 11 UTC (b). The obtained profiles are spatially averaged over the grid-cells with precipitation over 30 mm between 12 and 18 UTC. Averaged values of CAPE in (J) are given in the upper right corners. Colours of the profiles and CAPE values correspond to the experiments as denoted in the legend in the lower left corner of the panel (a).

In R2 very stable lower atmospheric conditions are simulated at 6 UTC (Figure 35a) with all experiments. Unlike in R1, the differences among the profiles in this region are small. The atmosphere is more humid in higher levels than in R1. Such profiles indicate favourable conditions for fog occurrence in this area. The afternoon profiles in Figure 35b indicate a strong surface heating and the PBLH over 2 km. Again, the deepest CBL is simulated with the nonlocal schemes. At the top of the CBL a strong drying is apparent with most of the schemes, only with YSU-MP this is less pronounced. The lowest CAPE is simulated with YSU and YSU-MP, while the highest values are obtained with ACM2. NOAH-MP when compared to NOAH, decreases CAPE for about 200 J when coupled with MYNN, while the value is higher when coupled with YSU.

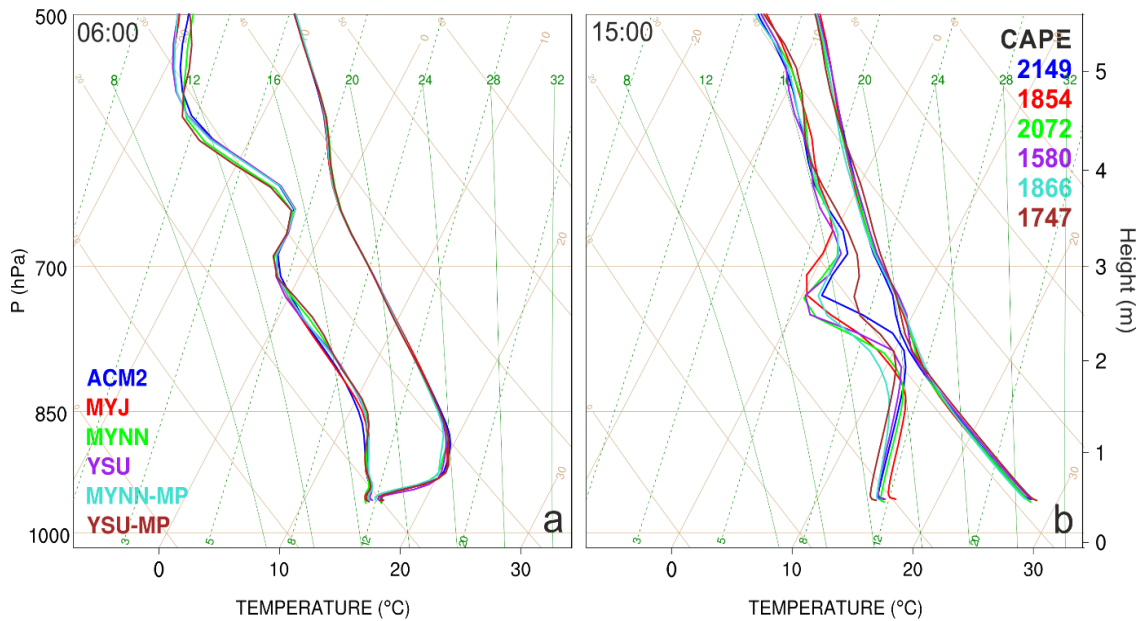


Figure 35. As in Figure 34 at 6 UTC (a) and 15 UTC (b) for the grid cells in the R2 region. CAPE for the morning sounding is not denoted since all the values equal to zero.

4.3.6. Land-atmosphere coupling

The land-atmosphere coupling strength in the R1 and R2 regions is assessed with the mixing diagram approach as in the dry case study. Unlike in the previous case, where the diagrams at the single point have been analysed, here in the convective case the mixing diagrams are plotted for the mean values over the two regions. Figure 36 demonstrates the coevolution of low atmospheric heat and moisture averaged over R1 (a) and R2 (b). The diagrams are plotted between 6 UTC and the time just before the CBL collapse, which mostly coincides with the simulated precipitation onset. For R1 it is taken to be 13:30 UTC, and 15 UTC for R2.

The behaviour of heat and moisture in the lower atmosphere within R1 (Figure 36a) among the NOAH experiments vary with the coupled PBL scheme. MYJ simulates overall the highest moisture and initially lower temperature in the lower atmosphere, while the driest lower atmospheric conditions are simulated with MYNN. ACM2 simulates stronger diurnal drying, and after 9 UTC it becomes the driest among the NOAH experiments. After 11:30 UTC ACM2 simulates a decrease in temperature for about 4 K. This time corresponds with the precipitation onset as showed in the previous results. A strong impact of LSMs is evident as well. With NOAH-MP the lower atmosphere is drier than with NOAH most of the given period, only in the morning hours

the behaviour is different. When coupled with MYNN, the two LSMs predicts very similar coevolution of heat and moisture between 6 and 7:30 UTC, while with YSU the difference is apparent: NOAH-MP simulates higher initial low atmospheric moisture and after 8 UTC strong drying occurs, which is not simulated with NOAH. From midday YSU-MP gives on average the driest conditions close to the ground.

According to the overlaid lines of RH, the difference among the simulations is not as pronounced. All the experiment give a change of about 15 % in RH between 6 and 12 UTC. After 12 UTC only ACM2 predicts a stronger increase in RH relative to the other 5 experiments, which is related to the earliest CI and precipitation onset as seen in the previous sections. On the other hand, the evolution of the mean lower atmospheric θ_e suggests the strongest buildup of moist static energy with MYJ. In the given period an increase in θ_e is for ~ 2 K higher than in all the other experiments. This suggests a stronger decrease in LFC and higher potential for cloud development with MYJ for this region.

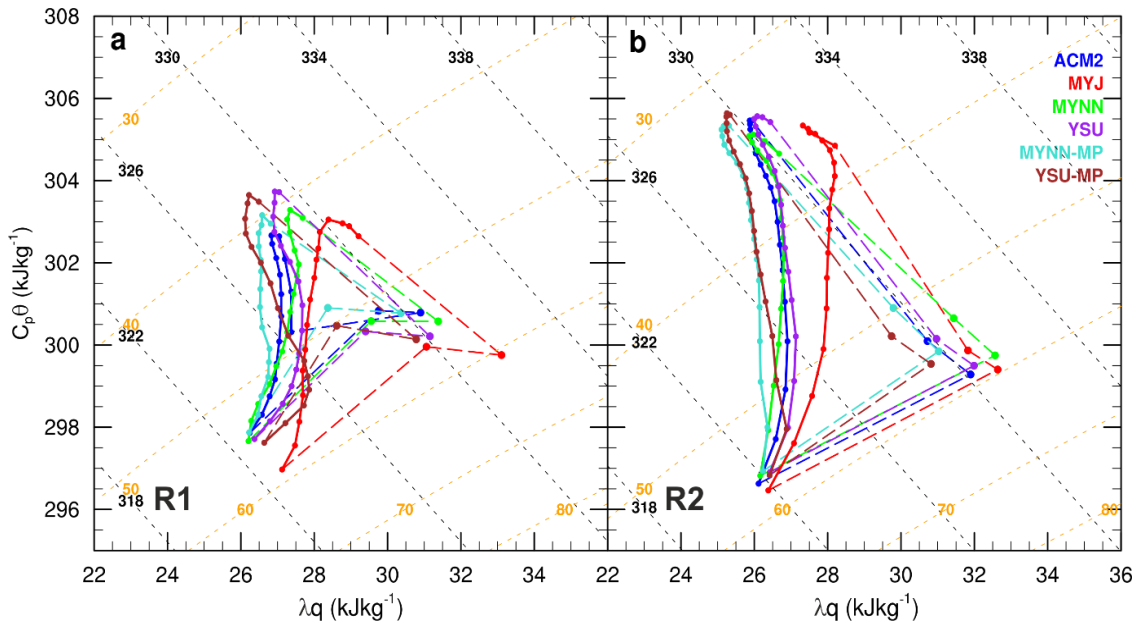


Figure 36. Mixing diagrams for 25 August 2009 averaged over R1 between 6 and 13:30 UTC (a) and over R2 between 6 and 15 UTC (b). The simulated coevolution of moisture λq and heat content $C_p\theta$ are in solid lines, while dashed lines stand for vectors corresponding to the surface (\mathbf{V}_{sf}), advected (\mathbf{V}_{adv}) and entrainment (\mathbf{V}_{entr}) fluxes. Colours of the lines correspond to the experiments as denoted in the legend in the upper right corner of the panel (b). Overlaid are lines of constant θ_e (in K; black dashed) and RH (in %; orange dashed).

The mixing diagram averaged over R2 in Figure 36b show a different behaviour relative to that in R1. It is apparent that all experiments simulate initially colder conditions than in R1, but with a stronger increase in temperature during the day. This is expected, since cloudless weather conditions were simulated in most of the region until the afternoon hours, which was not the case in R1. Furthermore, the variability in moisture conditions is small among ACM2, MYNN, MYNN-MP, YSU, and YSU-MP. Only with MYJ more pronounced drying is simulated between 6 and 12 UTC. The spread between results obtained with the NOAH experiments, which include MYNN, ACM2 and YSU is very small. The difference is more pronounced among the LSMs. Like in previous study, NOAH-MP is drier than NOAH here as well. The averaged values over R2 give a difference of $\sim 1 \text{ gkg}^{-1}$ between the LSMs.

A change in RH during the selected period is about 20 % for ACM2, MYNN and YSU. Marginally lower value are simulated with MYJ and higher with the two NOAH-MP experiments. According to the difference in θ_e , the highest moist static energy buildup is again simulated with MYJ, while the difference among the remaining experiments is small. When comparing the results among the two LSMs, NOAH-MP predicts slightly lower values than NOAH.

Table 6. The diagnostics extracted from the mixing diagrams at Figure 36 for R1 and R2: The mean ratio between sensible and latent heat flux at the interfacial layer (β_{entr}), the mean ratios of latent ($A_{\lambda E}$) and sensible heat (A_H) at the land surface to those at the interfacial layer, the mean quantified impact of horizontal advection of moisture ($AD_{\lambda E}$) and heat (AD_H). The mean surface Bowen ratio (β_{surf}) is calculated from the model output. All the mean variables are averaged temporally over 6.5 (9) hours and spatially over R1 (R2) on 25 August 2009 for the six experiments. Values extracted from for R1 and R2 in separated columns.

Experiment	β_{sfc}		β_{entr}		$A_{\lambda E}$		A_H		$AD_{\lambda E}$		AD_H	
	R1	R2	R1	R2	R1	R2	R1	R2	R1	R2	R1	R2
ACM2	0.84	0.44	0.15	-1.1	-1	-0.83	-0.16	2.02	0.16	-0.11	-0.01	0.1
MYJ	0.9	0.45	-1	-1.3	-0.99	-0.58	0.97	1.69	0.26	-0.08	-0.04	0.06
MYNN	0.88	0.45	-0.79	-0.86	-1.1	-0.74	0.86	1.37	0.26	-0.1	0	0.13
YSU	0.87	0.45	-0.99	-1.14	-1.36	-0.81	1.34	2.04	0.25	-0.1	-0.02	0.08
MYNN-MP	1.27	0.6	-0.79	-0.97	-1.65	-0.94	0.72	1.52	0.35	-0.13	-0.02	0.14
YSU-MP	1.75	0.6	-1.04	-1.19	-2.17	-1	1.17	1.99	0.35	-0.12	-0.05	0.08

The PBLH can be particularly critical for CI (e.g. Trier et al., 2003; Santanello et al., 2011). The PBL evolution strongly depends on sensible heating at the land surface, which together with small scale vertical mixing are critical for the PBL growth. Furthermore, very strong influence on the PBL evolution has entrainment, which can significantly increase the PBLH. In certain conditions entrainment can weaken the strength of the capping inversion, and in such a way facilitate the parcel to become positively buoyant and to reach the LFC. Therefore, accurate simulations of entrainment processes may be critical for the CI and precipitation as well. The mixing diagram diagnostics given in Table 6 show that H at the land surface is on average lower for all the NOAH experiments than λE (β_{sfc} is < 1), with low variability among the PBL schemes for both R1 and R2. About 50% lower β_{sfc} is obtained in R2 relative to R1, which indicates significantly higher λE . NOAH-MP increases β_{sfc} obtained for both regions and for both PBL schemes deployed. The increase is more pronounced in R1 region compared to R2. No significant change in β_{entr} is simulated between NOAH and NOAH-MP. Negative values of β_{entr} and $A_{\lambda E}$ suggest entrainment of dry air. Among the PBL schemes in R1, the highest dry air entrainment is obtained with YSU. For ACM2 and the local schemes the $A_{\lambda E}$ values are similar. In R2 a significantly different value is simulated with MYJ, which show the least dry air entrainment among the PBL schemes. NOAH-MP increases the dry air entrainment relative to NOAH for MYNN and YSU in both regions, but the difference is more pronounced in the R1 region. Entrainment of warm air is the lowest with the MYNN experiment in R2 (corresponds to the A_H values), while in R1 ACM2 simulates entrainment of cold air (due to the change in sign). In the case of ACM2, the mixing diagram captures the time after the DMC onset and the CBL collapse, which includes abrupt cooling of the CBL. Since A_H represents a value averaged over the selected time period, this suggest that the simulated entrainment of cold air after 12 UTC was higher than the warm air entrainment before 12 UTC. Due to this, the analysis of entrainment fluxes for ACM2 in R1 will be excluded from the discussion. This accounting for the time steps after the CBL collapse for the ACM2 experiment in the mixing diagrams is a compromise made in order to include the complete PBL evolution before the precipitation onset. For most of the schemes this is simulated at 13:30, only with ACM2 it 1.5 hours earlier. Values of $AD_{\lambda E}$ and AD_H suggest that the mean advected moisture contributes less to the total CBL flux in R2 than in R1. In R2 the values are ~ 0.1 , and the variability among the experiments is small. The contribution of the mean heat advection is not significant, for both regions it is < 0.15 .

4.4. Discussion

The 6 simulations of the convection case on 25 August 2009 are assessed in order to analyse and quantify the influence of the land surface processes calculated in LSMs and PBL features obtained from the PBL schemes on the simulated CI, cloud formation and precipitation. The analysis is done over the two regions with different climatological and soil moisture conditions. For each of the two regions a high variability exists among the results for accumulated precipitation, clouds and the strength of convection. Furthermore, simulated lower atmospheric conditions, vertical humidity profiles and atmospheric stability due to different differ among the experiments. The representation of the land-atmosphere coupling, assessed with the mixing diagram approach, show the sensitivity to the model configuration as well.

4.4.1. Sensitivity to PBL schemes

Lower atmospheric conditions prior to the CI in both assessed regions simulated with MYJ exhibit the highest differences when compared with the remaining 5 simulations. MYJ predicts significantly higher moisture close to the ground in both regions. Higher moisture with MYJ is primarily related to C_h (Figure 37c), which higher values correspond to the stronger mixing in the surface layer. Therefore, local transfer of heat and moisture from the land surface to the first model level simulated with MYJ is stronger than with the remaining experiments. This corresponds to the study by Xie et al. (2013), as well as to the results from the dry case study given in section 3. This suggests that the higher values for C_h may be systematically related to the Eta surface layer scheme that is coupled to MYJ relative to the revised MM5 scheme coupled with the other PBL schemes.

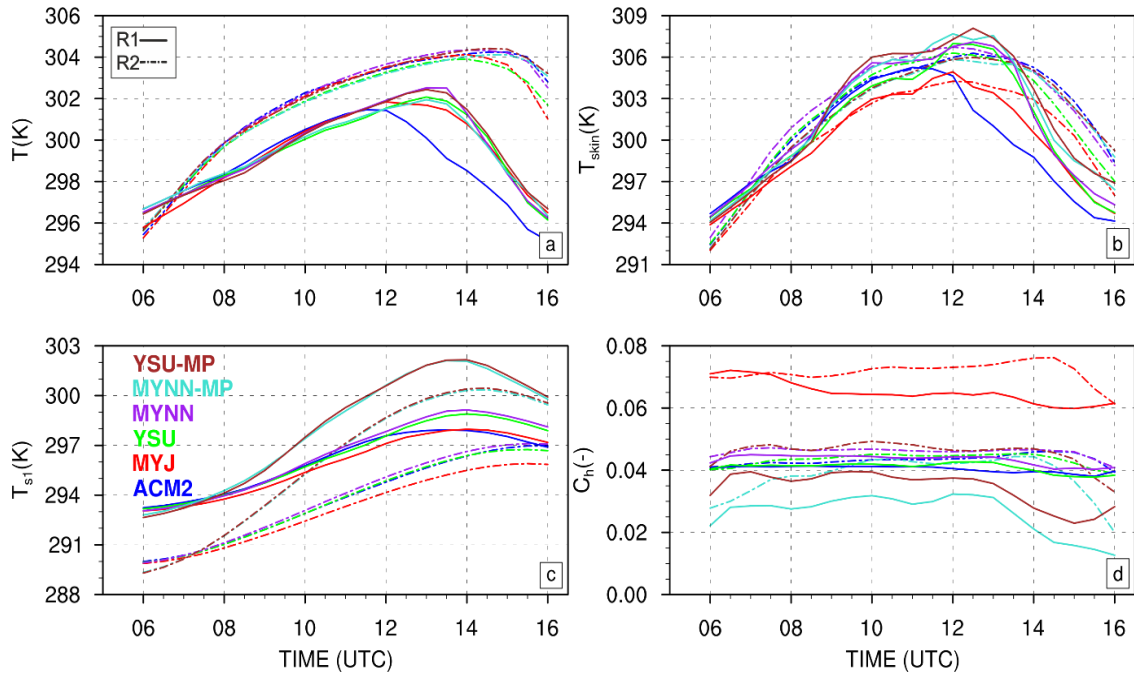


Figure 37. Simulations of temporal change of (a) the temperature at the first model level (T), (b) the surface temperature T_{skin} , (c) the temperature in the first soil layer T_{st} , and the surface exchange coefficient for scalar variables C_h divided by the friction velocity (d) on 25 August 2009 between 6 and 17 UTC.

The moisture is higher with MYJ not only close to the ground, but also within the whole CBL at times prior to the CI in both regions, as represented in the Skew T -log p diagrams in section 4.3.5. This coincides with the results obtained in the dry case study as well. Figure 38 demonstrates the temporal evolution of moisture and temperature averaged over the R1 region. The results suggest that with MYJ the moisture from the lower atmospheric levels is not transported as high as with the remaining schemes. This suggests that on average the convection events simulated with MYJ are not as deep as with the other PBL schemes, which is demonstrated in the two examples of vertical cross-sections for the maximum rainfall in R1 and R2 showed in section 4.3.4. The reason for that is in the weakest vertical mixing and the shallowest CBL simulated with MYJ relative to the remaining 3 PBL schemes.

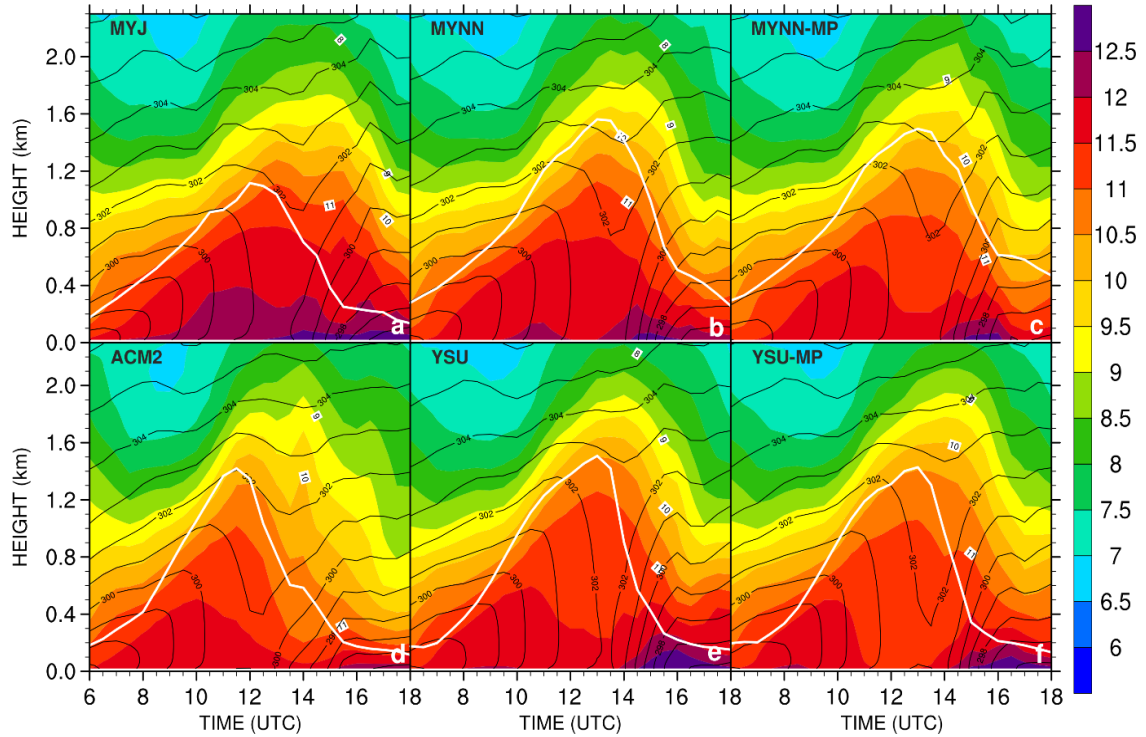


Figure 38. Temporal change of vertical profiles of q in gkg^{-1} from 6 to 18 UTC on 25 August 2009 averaged over the R1 region. Overlaid are lines for θ (black; K) and the PBLH (white; km).

Calculation of the mixing properties in the MYJ PBL scheme is artificially limited with the PBLH, which may result in less entrainment of dry air aloft. This corresponds to the mixing diagram diagnostic for $A_{\lambda E}$ obtained with MYJ, which is the lowest among the PBL schemes. MYNN generally accounts for a deeper CBL than MYJ (Figure 38 a, b c). This is associated to the stronger mixing simulated with this scheme. The parameterizations of the mixing properties in the local approach strongly depends on the l parameterization (see section 2.3.1), which differs between MYNN and MYJ (Table 3). This is crucial for the local parameterizations in general (e.g. Mellor and Yamada, 1982; Grisogono and Belusic, 2008). The MYNN parameterisation for l includes effects of stability and the land surface, which is not the case for the MYJ scheme. Furthermore, l is calculated within the whole atmospheric column, and is not limited up to the PBLH, as in MYJ. This allows the CBL to grow higher with MYNN than with MYJ.

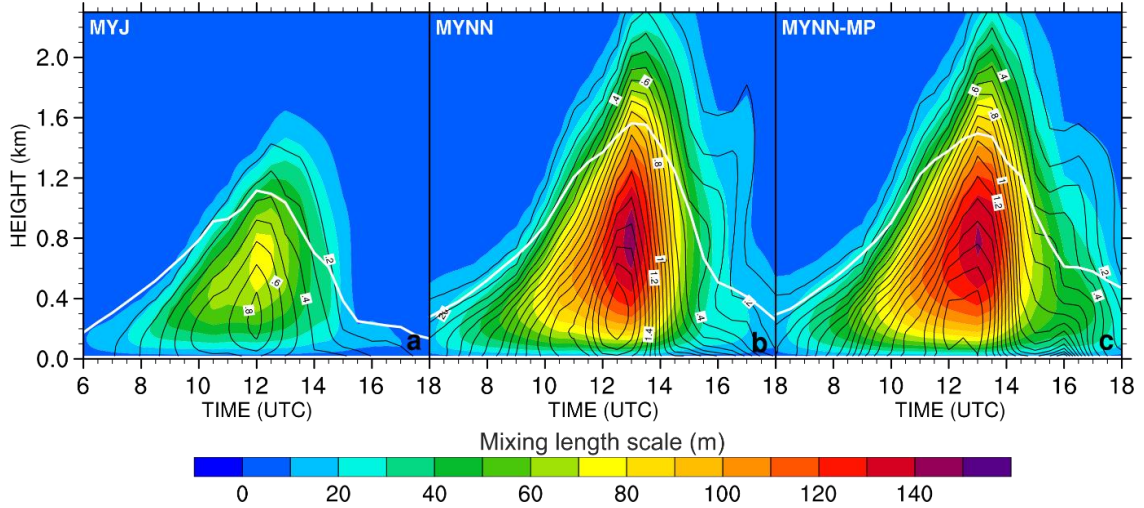


Figure 39. Temporal change of mixing length scale l in m from 6 to 18 UTC on 25 August 2009 averaged over the R1 region, as simulated with WRF configured with MYJ (a), MYNN (b), MYNN-MP (c). Overlaid are lines for TKE (black; Jkg^{-1}) and the PBLH (white; km).

MYNN simulates a significantly higher TKE as well (Figure 39 – TKE averaged over R1), which corresponds to the stronger mixing. On the other hand, the K_h simulations by the local schemes given in Figure 40 (averaged of over R1) show that the difference in values between MYJ and MYNN is not as high. K_h is an important parameter for calculating the turbulent fluxes as denoted in Eq. (8). Since K_h is related to l , TKE and the stability function S_h , this leads to a conclusion that the representation of S_h differs significantly among the local schemes (not shown). This result corresponds to the findings by e.g. Olson and Brown (2009).

When comparing the remaining values for K_h on Figure 40, the highest mean values over R1 are obtained with YSU (Figure 40d). This indicates the strongest mixing and consequently the highest CBL simulated with this experiment, as it is shown with the white solid lines in Figure 38 and Figure 40. This outcome agrees with the results of multitude of studies (e.g. Holtslag and Bolliulle, 1993; Olson and Brown, 2009; Hu et al., 2010; Coniglio et al., 2013; Xie et al., 2013, Cohen et al., 2015). ACM2 simulates the higher CBL as well, but with the earliest collapse (after 12 UC) among the schemes due to the precipitation onset. Such behaviour of the nonlocal schemes is primarily related to the incorporation of mixing done by largest eddies, which is the major discrepancy relative to the local approach. This large-eddy mixing in YSU is represented by including the countergradient term in Eq. (10) and in ACM2 by using the transient matrix Mu in Eq. (11), and these are responsible for a typically stronger transport of moisture from the

lower to higher atmospheric levels when comparing to the local schemes (Figure 38). Therefore the nonlocal schemes are more appropriate for the convective cases (e.g. Holtslag and Boville, 1993; 2009; Hu et al., 2010; Coniglio et al., 2013). The results suggest that mostly stronger convective activity and deeper convection is simulated with a nonlocal than a local approach. The stronger mixing with the nonlocal schemes is mostly accompanied with the stronger entrainment given in Table 6 for the nonlocal schemes (except for ACM2 in R1, which values are not relevant since the calculation include the time of the precipitation onset and the PBL collapse, see section 4.3.6).

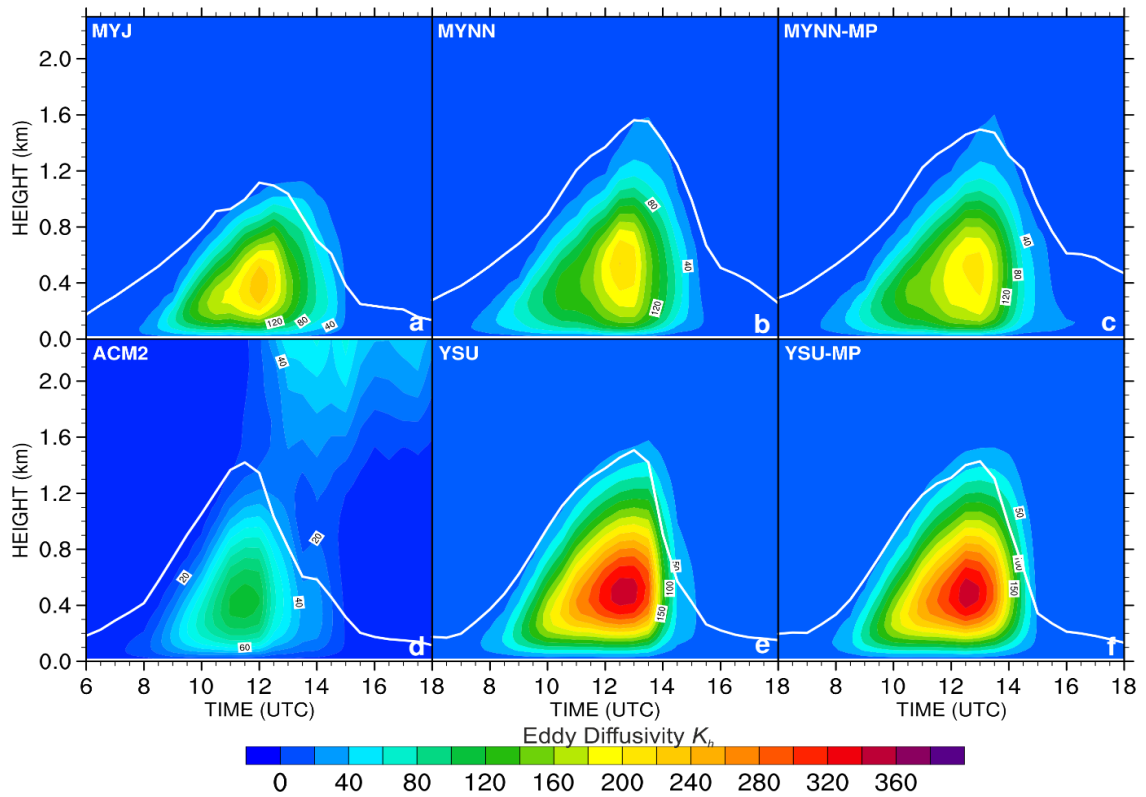


Figure 40. Temporal change of the eddy diffusivity for scalars K_h from 6 to 18 UTC on 25 August 2009 averaged over the R1 region, as simulated with WRF configured with MYJ (a), MYNN (b), MYNN-MP (c), YSU (d), MYNN-MP (e), and YSU-MP (d). Overlaid white lines denote the PBLH.

On average YSU simulates significantly higher values for K_h are in both regions than ACM2 (Figure 40d, e, f for R1, for R2 see in A3 in Appendices). This suggests that f_{cv} in Eq. (11) which controls nonlocal versus local mixing in ACM2 is close to 1. Furthermore, this indicates highly unstable conditions within the CBL simulated with ACM2, since this parameter is controlled by the atmospheric stability as denoted in Table 4. On the

other hand, the earliest convection onset with ACM2 in R1 may be related with the incoming solar radiation as suggested by Kleczek et al., (2014), which is a bit lower with ACM2 in this case study as well (not shown).

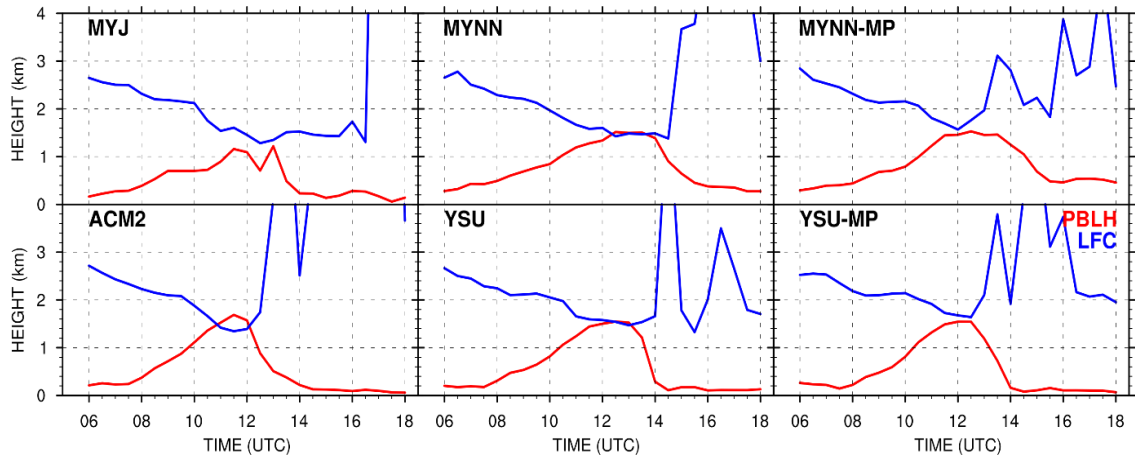


Figure 41. The simulated time series of the PBLH and LFC on 25 August 2009 averaged over the grid cells with accumulated precipitation exceeding 30 mm between 13 and 18 UTC in R1.

The PBL evolution plays an important role on the characteristics of the convection (e.g. Findell and Eltahir, 2003a; Ek and Mahrt, 1994; Betts, 2007; Santanello et al., 2011; 2013). The DMC is triggered when a lifted parcel manages to overcome negative buoyancy between the LCL and LFC and becomes positively buoyant. At that time the PBLH meets or exceeds the LFC and a DMC will occur. Therefore this can be a good indicator for the DMC onset (Findell and Eltahir, 2003a). The time series of the PBLH and LFC displayed in Figure 41 denote averaged values over the grid cells in R1 with the moderate to strong precipitation rate (e.g. over 30 mm within the 5 hour time frame). The plot suggests that on average at the locations with the strong rainfall simulated by ACM2, MYNN and YSU the DMC occurs. With MYJ the PBLH does not meet the LFC, even though a decrease of the LFC is simulated as with the other experiments. Furthermore, the plots confirms the results for the earliest precipitation onset predicted with ACM2. A similar outcome is simulated in R2 as well (see Figure A2 in Appendices).

The results with respect to the sensitivity of WRF to the PBL schemes may suggest that a shallow CBL followed by weaker mixing obtained with MYJ makes this scheme a isolated case, since it simulates atmospheric conditions quite altered from the other schemes. Significantly more humid lower atmospheric levels with MYJ is primarily

related to the different parameterization of the parameters which are calculated in the surface layer scheme. On the other hand, despite using the local approach as MYJ, MYNN gives more similar results to the nonlocal schemes deployed in this study. The reason for that may be in the modified representation of l and the extended calculation of the turbulent parameters throughout the whole atmospheric column. ACM2 exhibits an altered behaviour from the other schemes as well, which is particularly evident in R1. The time and strength of the DMC simulated with ACM2 within this region differs substantially from the remaining PBL schemes. The ACM2 morning profiles show the weaker residual layer, and significantly higher moisture in the upper atmosphere between 1.5 and 3 km. A weaker residual layer and higher moisture in the air aloft in the morning (Figure 34) supports an easier and faster CBL evolution (e.g. Stull, 1988; Angevine, 2008; Blay-Carreras et al., 2014) which can be seen when comparing the PBLH lines in Figure 38, a, b, d, and e. These conditions makes favourable environment for a DMC to occur (e.g. Khodayar, 2009; Gentine et al., 2013), which are not simulated with the other three schemes in R1.

4.4.2. Sensitivity to LSMs

The results from this case study show that the difference between NOAH and NOAH-MP simulations is not as apparent as in the dry case study. NOAH-MP accounts for marginally more (less) initial soil moisture at the top soil layer in R1 (R2) and overall significantly higher T_{sl} in both regions (see Figure 23) than NOAH. Consequently, as expected, significant variations in energy balance at the land surface between the LSM are obtained. As in the dry case study, λE averaged over the regions is significantly lower with NOAH-MP than with NOAH, and the difference range up to 70 Wm^{-2} (Figure 42b). The differences in H among the LSMs (Figure 42a) are up to $\sim 20 \text{ Wm}^{-2}$. The most of the residual energy goes to the ground which is not sensitive to the location. The discussion regarding the differences in energy balance between the LSMs is given in section 3.5.2, and can be applied in this case as well.

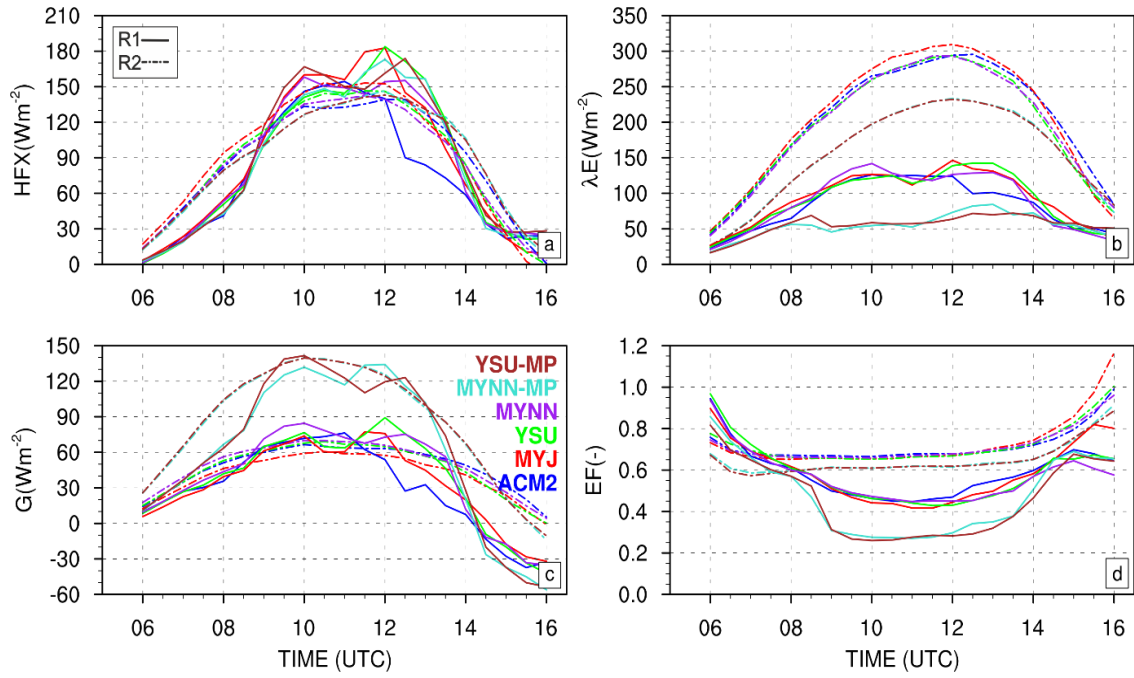


Figure 42. Simulations of the temporal change of (a) sensible heat flux (H), (b) latent heat flux (λE), (c) ground heat flux (G), and (d) Evaporative fraction (EF) on 25 August 2009 from 6 to 16 UTC.

The difference between R1 and R2 regions is apparent from the results for the evaporative fraction (EF ; Figure 42d), which can be defined as the ratio between λE and the available energy at the land surface [$EF \equiv \lambda E / (H + \lambda E)$]. In R1 it is more pronounced than in R2. The averaged values over R1 give the difference of more than 20 % in EF between the LSMs, while in R2 it is less than 10 %. This may be primarily related to the different schemes used for the calculation of stomatal resistance. The results obtained from the offline NOAH-MP sensitivity study by Ingwersen et al. (2015) showed that the photosynthesis based Ball-Berry scheme in NOAH-MP accounts for lower EF than the Jarvis scheme in NOAH, which relies on a parameterised minimum canopy resistance and meteorological variables, such as air temperature and incident radiation. The photosynthesis based schemes, such as the Ball-Berry scheme is more sensitive to soil and vegetation conditions at the land surface, which are represented through LAI in the model (e.g. Kumar et al., 2011). Therefore the higher difference in R1 relative to R2 can be related to different vegetation conditions among the regions which are introduced in section 4.1. In R1 the land is mostly converted into croplands, while in R2 the share of grassland is about 50 %. Since $LAI(\text{grassland}) > LAI(\text{cropland})$, and stomatal resistance is inversely proportional to LAI, this contributes to higher λE in R2 than in R1 through transpiration term in the potential evapotranspiration (see section 2.2). Furthermore, the

highest difference in EF appears when the CBL is well mixed. The difference decreases at the time which coincides with the precipitation onset in the NOAH-MP experiments. Lower EF corresponds to lower moisture availability at the land surface. NOAH-MP in both regions accounts for lower Ch as well (Figure 37d), which is responsible for the mixing in the surface layer and moisture transport from the land surface to the first model level. This can explain the drier lower atmospheric conditions with NOAH-MP than with NOAH presented in section 4.3.3. With respect to the temperature, NOAH-MP simulates colder conditions, but the difference is not as pronounced as in the case of moisture. This is related to the significantly smaller differences in H relative to λE between the LSMs.

The diagnostics for dry air entrainment from the mixing diagram show that the values are higher with NOAH-MP than NOAH. The difference between the LSMs is greater within R1, than in R2. On the other hand, the heat entrainment at the CBL top is mostly lower with NOAH-MP, only in R2 with the MYNN experiment the value is marginally higher.

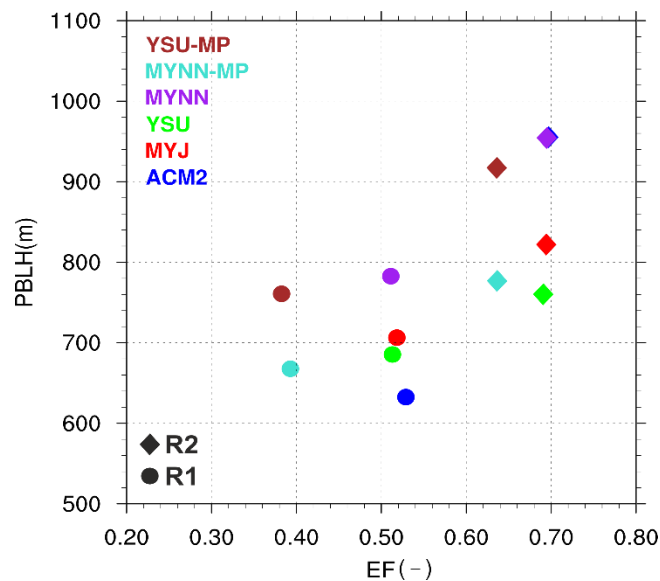


Figure 43. Mean EF versus $PBLH$ averaged over the R1 and R2 region averaged between 6 and 16 UTC. The colours of the markers correspond to the experiment as denoted in the upper left corner, and the shape to the region (circles to R1, diamonds to R2).

Figure 43 demonstrates PBLH over EF, both spatially averaged over R1 and R2, and temporally from 6 to 16 UTC. The drier conditions at the land surface in R1 relative to R2 are apparent, but the drier conditions simulated with NOAH-MP generally does not increase the PBLH over both regions. It is just the opposite, the values are decreased.

Only in the case of MYNN in R2 the PBLH is slightly augmented. This correlates to the warm air entrainment given in the mixing diagram, which is higher with MYNN-MP compared to MYNN.

The land surface conditions simulated with the LSMs show a strong influence on the simulated vertical humidity and temperature profiles, and subsequently precipitation. The averaged values over the whole study area show weaker rainfall with NOAH-MP (Figure 25). This is expected since NOAH-MP overall simulates less moisture close to the ground, and the CBL is overall drier than with NOAH. Therefore less moisture is transported to the higher atmospheric levels with NOAH-MP, and consequently the chance for DMC to occur is lower than with NOAH. Overall, the CBL up to the CBL top simulated with NOAH-MP is on average drier with NOAH-MP relative to NOAH (for R1 Figure 38b, c, e, f, and similar for R2 see Figure A1 in Appendices).

The surprising results are obtained over R1 with respect to strong precipitation events (i.e. $> 10 \text{ mmh}^{-1}$). NOAH-MP when coupled with YSU simulates both higher averaged precipitation (see Figure A4 in Appendices) and the higher spread of moderate to strong precipitation events over R1 than NOAH. Vertical profiles prior to the onset of the precipitation given in section 4.3.5 in Figure 34b show a high discrepancy between YSU and YSU-MP, while the vertical structure of the atmosphere is similar for the two MYNN experiments. This may indicate that more advected clouds were simulated in R1 with YSU-MP than with YSU. Therefore, this does not mean that YSU-MP simulates a higher convection activity within the R1. This is confirmed with a significantly lower CAPE averaged over the locations where accumulated precipitation is over 10 mmh^{-1} within R1 for the time prior to the rainfall onset. The change in θ_e from the mixing diagram shows also indicates that the moist static energy buildup with the two NOAH-MP experiments is reduced when comparing to the NOAH experiments. The lower moist static energy buildup suggests a smaller decrease in LFC, and consequently a less likelihood for a DMC to occur (Findell and Eltahir, 2003a). Figure 41 demonstrates that the PBLH and LFC come close together with NOAH-MP in R1 region, but the crossover does not occur like in NOAH experiments (similar is happening in the R2, see A2 in Appendices). This may indicate that at the locations with the strong rainfall (over 10 mmh^{-1}) DMC occurs more often with NOAH than NOAH-MP.

5. General conclusions

In this thesis the sensitivity of WRF to PBL parameterization schemes and LSMs was studied with respect to the model representation of the PBL and land surface features relevant for two different weather conditions. The simulations of the CBL characteristics, which include the PBLH, humidity and temperatures profiles, are assessed on a clear sky day. In a convective environment, the study was focused on the model representation of clouds, lower atmospheric conditions, with special emphasis on moisture, temperature and wind. Furthermore, the atmospheric stability, vertical distribution of heat and moisture and the model simulation of precipitation were assessed as well. In both case studies the nature of simulated SVA feedbacks was studied by applying the mixing diagrams. In this approach, the land-atmosphere coupling is assessed through the analysis of the surface layer heat and moisture coevolution and their impact on the processes at the CBL top, such as entrainment of free tropospheric air into the CBL.

An ensemble comprising six simulations was conducted with the WRF model version 3.5.1. The horizontal grid spacing was set to 2 km, which corresponds to the CP scale. The simulations differed in their model configuration: two local (MYJ and MYNN) and two nonlocal (ACM2 and YSU) PBL schemes were combined with two LSMs, NOAH and NOAH-MP. NOAH-MP is an advancement of NOAH. It is a state of the art LSM developed as a standalone model and available in WRF since 2014. NOAH-MP includes a selection of 12 additional physics options for parameterizing the processes in the soil and at the land surface at higher complexity than NOAH. This comprehensive study represents one of the sparse studies performed with NOAH-MP coupled to WRF. Its configuration was carefully chosen for the sensitivity studies according to numerous test simulations. The NOAH-MP configuration deployed for this research is depicted in Table 2 in section 2.2.2.

The analysis was performed for three locations in Germany. The dry case study was analysed for a site located in NW Germany close to Jülich, and was supported by high resolution WVDIAL and radiosonde measurements. The convection case study is a model experiment in which the emphasis is put on the sensitivity of WRF results to the variability in the model configuration with respect to the PBL schemes and LSMs. The purpose of this study was not to validate the simulations, but to show the variability in

the results from the 6 simulations in representing convection and precipitation. Therefore, the model validation with observation has not been performed. The model intercomparison was done for two regions in SW Germany (Kraichgau – R1 and Swabian Alb – R2), different in their land surface characteristics and climatology. In R1 most of the agricultural land is converted into cropland, while in R2 the share of grassland is nearly equal to the share of croplands. Silty clay loam is the prevailing top soil texture in R1, while in R2 it is mostly silty loam (Wizemann et al., 2015). A more humid top soil layer (top 10 cm of the soil) was simulated in R1 than in R2.

All research presented here was performed in order to answer the main research questions given in the beginning of this thesis in section 1.4. Therefore, the major conclusions are given as answers to those imposed questions. These are the questions with corresponding answers:

Question 1: How sensitive are the CP WRF simulations of PBL processes and DMC to the PBL parameterization in temperate climate conditions?

The major findings from the dry case study with respect to the sensitivity of WRF to the PBL schemes are primarily related to a different behaviour of MYJ compared to the remaining 3 schemes. MYJ with NOAH accounts for the highest moisture in the CBL. This is related to weaker mixing simulated with MYJ, which coincides with studies such as e.g. Holtslag and Boville, 1993; Cuijpers and Holtslag, 1998; Teixeira and Cheinet, 2004; Coniglio et al., 2013; Cohen et al., 2015. Furthermore, it is also related to the Eta similarity land surface scheme that is coupled with MYJ (a fixed setting in WRF), and is different from the surface layer scheme used in all the other simulations. The exchange coefficient for heat and moisture simulated by the Eta scheme is significantly higher compared to the other experiments. This results in higher surface heating simulated with MYJ which leads to the faster build-up of the CBL in the morning. But due to limited mixing in MYJ, the CBL in the afternoon is not evolved like e.g. with MYNN. This is primarily related to the parameterization of the mixing length scale, which in MYJ is not related on the PBL stability and is inconsistent in more unstable environments. More mixing in the CBL is simulated with the MYNN scheme, which uses MYJ as a baseline, but with a more sophisticated and stability dependent parameterization of the mixing length scale. The dry case study showed that this leads to a better agreement with the

measurements of humidity profiles. The differences between the results obtained with the two nonlocal schemes are negligible. Both simulate a higher and drier CBL and stronger mixing than the local schemes, which coincides with studies such as Coniglio et al. (2013), Xie et al. (2012, 2013) and Cohen et al. (2015). However, when comparing the model results to the WVDIAL measurements, the CBL with the nonlocal schemes is too high and too dry.

The convective case analysis reveals a strong impact of the model configuration with respect to the PBL schemes on simulating preconditions for the DMC and resulting precipitation. The variability in the simulated amount and location of the precipitation between the experiments is strong. The major findings with respect to the CBL features, such as the PBLH, moisture and temperature within the CBL, correspond to those obtained in the dry case study. For example, the lower atmospheric conditions are more humid with MYJ, which is primarily related to the parameters simulated in the surface layer scheme here as well. Averaged precipitation over the whole study site accumulated over 24 hours is higher with the nonlocal schemes than with the local PBL schemes. The simulated convection within the two regions shows distinctive characteristics which strongly depend on the selection of the PBL parameterization schemes. The analysis shows that the convection simulated with MYJ is limited and does not evolve as deep as with the other three PBL schemes. The reason for that could be related to the free atmospheric moisture (Gentine et al., 2013) which is lower with MYJ relative to the other three schemes, and this does not depend on the location.

Question 2: To what extent do LSM physics influences simulated atmospheric processes, especially PBL evolution, entrainment, convection and precipitation?

The results from the research presented in this thesis demonstrate that the influence of the land surface processes extends up to the interfacial layer, where air from the free atmosphere entrains into the CBL. Simulations with NOAH-MP in the dry case study result in a drier and higher CBL than with NOAH. This is related to the higher Bowen ratio (lower evaporative fraction) at the land surface. Furthermore, the entrainment fluxes from the free atmosphere into the CBL are generally higher with NOAH-MP. This is

much more pronounced in the dry case study (up to 6 time higher), while the difference in the convective case study is not as evident (up to 1.5 time higher).

The LSM choice in the convective case shows a strong influence on the model representation of humidity and temperature profiles, CI and rainfall, with respect to both location and amount. The averaged values over the whole study area show less precipitation with NOAH-MP than with NOAH. Moreover, NOAH-MP simulates lower moisture in the lower atmospheric levels, and the CBL is drier. Furthermore, NOAH-MP gives weaker updrafts when the convection is triggered, which decreases the chance for DMC to occur. The results suggest that at the locations with the strong rainfall (over 10 mmh^{-1}) DMC occurs more often with NOAH than NOAH-MP, which is related to the *EF* which is generally lower with NOAH-MP. Further the difference depends on the vegetation cover. This shows the higher sensitivity of NOAH-MP to vegetation parameters than NOAH, which is primarily related to calculation of the stomatal resistance. The entrainment fluxes of dry air are higher with NOAH-MP, and the difference is higher within R1 (lower *EF*), than in R2 (higher *EF*). The heat entrainment is mostly lower with NOAH-MP, only with the MYNN-MP experiment it is marginally higher in R2.

Question 3: What coupling effects exist between the land surface and PBL model physics and are they dependent on location and weather conditions?

The budget analysis in the form of mixing diagrams allows for the calculation of the mean entrainment-to-surface ratios of sensible and latent heat flux in the CBL, the relative impact of mean heat and moisture advection terms, and the mean Bowen ratio at the interfacial layer. It shows that a significantly higher dry air entrainment is simulated with NOAH-MP than with NOAH. Due to lack of eligible flux observations, the mixing diagrams could not be supported by the measurements. Nevertheless, both studies have demonstrated that the analysis of such diagrams is an effective way of testing the WRF model sensitivity to different parameterization schemes in both clear sky and convective weather conditions.

The major conclusion from the analysis is that the land-atmosphere coupling in WRF is more dependent on the LSMs than on the PBL schemes for both cases. This supports the findings by Santanello et al. (2009; 2011; 2013) from studies exhibited over the U. S.

Southern Great Planes with the same model, but configured with different PBL parametrization schemes and LSMs. Furthermore, the results indicate that the coupling strength between the local and nonlocal schemes on one hand side and the LSMs on the other hand side is different. In the dry case study an influence of the LSM choice on the simulated CBL features is higher when the model is configured with MYNN than with YSU, which is evident from both the humidity profiles and the mixing diagrams. This opposes the results obtained in the convective case study, where the stronger coupling is evident when the model is coupled with the YSU scheme.

Moreover, both studies demonstrated that the coupling strength is sensitive to the surface Bowen ratio. The higher the surface Bowen ratio the stronger the coupling of WRF towards the land surface, and vice versa. The Bowen ratio strongly depends on the vegetation and soil conditions, which is spatially variable and depends on soil characteristics such as soil texture. This leads to the conclusion that the coupling strength between the land surface and atmosphere is strongly related to the location. This supports the findings from e.g. Koster et al., (2006) on global and e.g. Findell and Eltahir (2003), Gentine et al. (2013), Knist et al. (2016) on regional scales.

Question 4: To what extent the WVDIAL measurements can be used for the assessment of actual and modelled PBL evolution at the CP scale?

In the dry case study the model results were supported with the high resolution WVDIAL measurements. These measurements were used for model validation for the first time. The results overall demonstrated high potential for a detailed analysis of the grid-cell averaged structure of the humidity profiles, PBLH, development of the CBL and the moist residual layer. The analysis of these features through the simulated humidity profiles in comparisons with the WVDIAL measurements, showed that all 6 experiments simulate a too fast CBL evolution, with significant overshooting in the afternoon. This overshooting is more pronounced with the nonlocal YSU and ACM2 schemes, as well as in the simulations coupled with NOAH-MP, while the best agreement with the observations is obtained with MYNN coupled with NOAH. Furthermore, none of the schemes has been able to reproduce the strong residual layer as measured, as well as the observed strength and height of the inversion at the CBL top (also evident from the comparisons with the RS measurements). The reason for this great difference between

the simulations and measurements may be partly due to the model initialization data (ECMWF analysis). To decrease discrepancies between the model simulations and observations, the initial and boundary conditions need to be improved, and this dry case study confirms that. To do so, moving toward data assimilations as a standard for case studies such as this is a prerequisite.

Question 5: What LSMs and PBL parameterizations show the most promising results at the CP scale?

The results from the sensitivity studies represented in this thesis reveal advantages and disadvantages of the parameterization schemes deployed. More sensitivity studies on different cases and study locations in conjunction with high quality observational data are required define the best configuration among the experiments. Nevertheless, from the major conclusions presented above, some information with respect to the most promising results can be given. First and foremost, it has been demonstrated that the two PBL schemes, MYJ in the dry case study and ACM2 in the convective case study exhibit the results which are very distinct from the other experiments. Therefore, for long term runs on the CP scale, it is advisable to use the YSU or MYNN scheme. The MYNN scheme coupled with NOAH gives the best agreement with the available measurements in the dry case study. It is worth mentioning that the MYNN scheme computationally is up to 20% more costly than the widely used YSU, but on the other hand too strong mixing and too high CBL can contribute positive biases on the simulation of precipitation on CP scales. Such a systematic bias may build up in climate simulations.

Among the two LSMs deployed in the study, NOAH may exhibit better results compared to NOAH-MP relative to WVDIAL measurements, but the simulations of certain variables at the land surface, such as *EF* and the parameters used within the scheme are more physically consistent. NOAH-MP is a complex land surface model that deals with processes at the land surface and in the soil which become increasingly important on finer model resolutions. Furthermore, this model is more sensitive to the land surface inhomogeneities, therefore the results strongly depend on the model representation of the vegetation, soil texture and land use. The LSMs are not independently applied from the surface layer scheme, which calculates the turbulent exchange coefficients in cases when an LSM is coupled to an atmospheric model. However all the surface layer schemes were

developed prior to NOAH-MP and might need to be revised when using such a complex LSM in which the energy partitioning is strongly sensitive to the model representation of vegetation.

6. Outlook

The high impact of the land surface on the PBL features, and the height to which this impact extends are distinct findings of this study. The results suggest that the energy partitioning at the land surface strongly influences the CBL evolution, also affecting the processes at interfacial layer, such as the entrainment of free-atmospheric air into the CBL. From this study it is evident that there is a greater sensitivity of WRF to the LSMs than to the PBL schemes, which is more pronounced in the clear sky weather conditions. However, this conclusion might be dependent on the LSM choice itself, or to the particular NOAH-MP configuration. Therefore, additional sensitivity studies of WRF to NOAH-MP switches are essential. For the case studies such as these, particularly important would be to test the switches related to the radiative transfer (`opt_rad`), the calculation of canopy stomatal resistance (`opt_crs`), the soil moisture factor for stomatal resistance (`opt_btr`) and the surface layer drag coefficient (`opt_sfc`). These switches strongly affect the energy partitioning at the land surface in short time scale simulations, as well as the heat and moisture transport from the land surface to the first model level, which showed the largest difference among NOAH and NOAH-MP. Furthermore, for RCMs on a longer time scale a choice of dynamic vegetation model (`dveg`) should be considered as well. For the presented studies it was switched off, but in long term runs for more than a year it should be switched on. With this option the model includes more dynamics in phenology parameters.

Furthermore, the monthly partitioning between bare soil and vegetated part of a grid cell in WRF is controlled with F_{veg} , which is based on a 20 year old data set, and hence does not reflect changes in agricultural management or modifications imposed by recent climate change (Nielsen et al., 2013). Neglecting such modifications will subsequently affect the PBL evolution, cloud formation and precipitation occurrence. Updating F_{veg} in WRF would improve the model's surface energy and water balance representation. Furthermore, the implementation of vegetation-growth models into LSMs at least for agriculturally managed land will increase consistency in energy partitioning at the land surface processes. In such a way, the lower boundary conditions for PBL schemes will be improved. The advanced representation of land surface heterogeneity in models is increasingly important at finer grid resolutions (e.g. Ament and Simmer, 2006), where

land surface data at a field scale can be used, as well as in the more sophisticated LSMs such as NOAH-MP. An effort towards this direction has already been made within the RU 1695 project. A sophisticated crop-growth model, Genotype-by-Environment interaction on CROp growth Simulator (GECROS), which differentiates summer from winter crops is coupled to NOAH-MP offline. The GECROS model is implemented into WRF-NOAH-MP and currently under verification. This crop growth model will affect the calculation of the stomatal resistance and LAI, two parameters on which the surface energy balance is strongly sensitive. Therefore it is expected that the implementation of GECROS will contribute to more consistent results at the land surface and consequently in the overlaying atmosphere as well. It is most likely that this effort will lead towards the better representation of seasonal variability in the RCMs.

The entrainment fluxes are an important aspect of the PBL schemes. It is of great relevance to obtain a realistic insight in the sensible and latent heat flux profiles, with special emphasis on the fluxes at the interfacial layer. In these studies only one scheme (YSU) uses the explicit parameterization of the entrainment fluxes. This has been shown already beneficial for the model accuracy (Hong et al., 2006). To further improve the PBL parameterizations, new approaches can be implemented and tested. Wulfmeyer et al. (2016) developed a new theoretical concept for representing the entrainment fluxes, which is more physically consistent than the approach used in e.g. YSU. A possible way to advance PBL parameterization schemes would be an implementation of such a theory into the schemes. A general shortcoming of the PBL schemes is that they are mostly calibrated with LES results, and very often only for dry atmospheric conditions (e.g. MYNN). Such parameterizations need an extensive evaluation and validation with realistic high resolution measurements in different weather conditions, such as WVDIAL humidity, TRRL temperature and DL wind measurements. For that, detailed observations of flux profiles are a prerequisite. Onwards, these studies showed a strong sensitivity of the WRF model to the surface layer scheme as well. The MO similarity theory needs an extensive evaluation, with special emphasis on the stability functions. The evaluation should be done over the regions with different land-surface characteristic to test whether the MO similarity theory is applicable over e.g. complex terrain with respect to orography. Within the RU 1695 field experiment SABLE such measurement were performed. The measurement design permits to map surface fluxes along the line-of-sight of the lidar combination by closing the full set of the MO similarity relationships.

Furthermore, in the vertically steering mode, profiles of mean variables and their gradients of higher-order turbulent moments as well as of latent and sensible heat fluxes can be derived. This gives a valuable data set that can be used for model validation and updating the critical parameters and certain parameterizations in the PBL schemes that are shown to be critical, such as the mixing length scale and entrainment fluxes, as well as scaling strategies for parameterizations from LES scale to CP scale.

For further improvement of model accuracy, it is essential to investigate the SVA feedback which varies across seasons and regions, and to identify regions with strong SVA feedbacks since they play a major role in a changing climate. Numerous studies have been already done in order to identify regions with strong land-atmosphere coupling based on modelling studies on global (Koster et al., 2006; Guo et al., 2006) and regional climate scales (e.g. Seneviratne et al., 2010; Knist et al., 2016). The importance of the land-atmosphere coupling on local scales will increase with the model resolution. Therefore, analyses such as these case studies should be carried out in different weather conditions, over various land covers and over different time scales as well. It is essential to validate the results with measurements. This study demonstrates the experimental setup and the benefits of analyses methods such as the mixing diagram approach for studying the SVA feedback in the future, namely with the increasing number of high resolution observational data becoming available to support the validation. Such data sets for detailed studies of SVA feedback processes will be available within the Land-Atmosphere-Feedback-Experiment (LAFE³) campaign. In August 2017, the campaign will deploy the novel synergy of remote sensing systems for simultaneous measurements of land-surface fluxes and horizontal and vertical transport processes in the CBL. The data set of such simultaneous measurements will enable detailed studies of SVA feedback processes in dependence of large-scale and local conditions, such as soil moisture and vegetation, as well as verification of the model representation of SVA feedback processes on various scales. New generation experiments such as SABLE and LAFE are a prerequisite to improve our understanding of SVA feedback processes and their representation in weather and climate models.

³ <http://www.arm.gov/campaigns/sgp2017lafe>

7. Abbreviations

ACM2	Asymmetric Convective Model version 2
BATS	Biosphere – Atmosphere Transfer Scheme
CAPE	Convective Potential Energy
CBL	Convective planetary boundary layer
CI	Convection Initiation
CIN	Convection Inhibition
CLM	Community land model
DAIL	Differential Abortion Lidar
DL	Doppler Lidar
DMC	Deep Moist Convection
DWD	German Meteorological Service (Deutscher Wetterdienst)
ECMWF	European Centre for Medium Range Weather Forecasts
EF	Evaporative Fraction
EUMETSAT	European Organisation for the Exploitation of Meteorological Satellites
FLUXPAT	Fluxes and Patterns in the Soil-Vegetation-Atmosphere System
FVEG	Vegetation Fraction
GECROS	Genotype-by-Environment interaction on CROp growth Simulator
HD(CP) ²	High Definition Clouds and Precipitation
HOPE	HD(CP) ² Observational Prototype Experiment
HTESSEL	Hydrology Tiled ECMWF Scheme for Surface Exchanges over Land
HWSD	Harmonized World Soil Database
IGSP	International Geosphere-Biosphere Programme
KC	Kraichgau
LAFE	Land-Atmosphere Feedback Experiment
LAI	Leaf Area Index
LCL	Lifting Condensation Level
LES	Large Eddy Simulations
LFC	Level of Free Convection
LSM	Land surface model
MM5	Mesoscale Meteorological Model, version 5
MODIS	Moderate Resolution Imaging Spectroradiometer

MRF	Medium Range Forecast
MYJ	Mellor – Yamada – Janjić
MYNN	Mellor – Yamada – Nakanishi – Niino
MYNN-MP	MYNN coupled with NOAH-Multiple Physics
NOAH-MP	NOAH – Multiple Physics
NWP	Numerical Weather Prediction
PBL	Planetary Boundary Layer
PBLH	PBL Height
RCM	Regional Climate Model
RRTMG	Rapid Radiative Transfer Model for Global circulation models
RU	Research Unit
SA	Swabian Alb
SABLE	Surface Atmosphere Boundary Layer Exchange
SVA	Soil Vegetation Atmosphere
TKE	Turbulent Kinetic Energy
TOA	Top of the Atmosphere
TR	TransRegio
TRRL	Temperature Rotational Raman lidar
WRF	Weather Research and Forecasting
WRF-NOAH	WRF coupled with NOAH
WRF-NOAH-MP	WRF coupled with NOAH-MP
WVDIAL	Water Vapour Differential Absorption Lidar
YSU	Yonsei University
YSU-MP	Yonsei University coupled with NOAH-MP

8. Symbols

AD_H	Quantified impact of horizontal advection of heat
$AD_{\lambda E}$	Quantified impact of horizontal advection of moisture
A_H	Ratio of sensible heat flux at the land surface to its value at the interfacial layer
$A_{\lambda E}$	Ratio of latent heat flux at the land surface to its value at the interfacial layer
C_h	Exchange coefficient for scalar variables (heat)
C_m	Exchange coefficient for momentum
C_p	Specific heat capacity of moist air
C_q	Exchange coefficient for scalar variables (moisture)
E	Evapotranspiration
EF	Evaporative Fraction
E_p	Potential evapotranspiration
f_{cv}	Weighting factor in ACM2 (controls local versus nonlocal mixing)
F_{veg}	Vegetation fraction
G	Ground heat flux
H	Sensible heat flux
z_i	Planetary boundary layer height (PBLH)
$z_{i(TKE)}$	PBLH calculated with the TKE method
$z_{i(\theta)}$	PBLH calculated with the θ -increase method
K_m	Eddy diffusivity for momentum
K_h	Eddy diffusivity for scalar variables
LW	Longwave radiation
l	Mixing length scale
l_b	Mixing length scale related to the buoyancy force
L	Monin-Obukhov length scale
l_s	Mixing length scale in the surface layer
l_t	Turbulent length scale
m	Momentum
Mu	Upward convective mixing rate in ACM2
N	Brunt-Väisälä frequency
Pr	Prandtl number
q	Mixing ratio

q_c	Velocity scale in MYNN
q_{sat}	Saturated humidity
RH	Relative humidity
Ri_b	Bulk Richardson number
Ri_{bcr}	Critical bulk Richardson number
R_N	Net radiation
SW	Solar shortwave radiation
S_h	Stability function for scalar variables (heat)
S_ψ	Stability function for ψ variable (momentum or scalar)
T	Temperature
t_{end}	End time (in the mixing diagram)
TKE	Turbulent kinetic energy
T_{s1}	Temperature in the first (top) soil layer
T_{skin}	Skin temperature
t_{start}	Start time (in the mixing diagram)
T_v	Virtual temperature
u	Horizontal wind speed
w'	Vertical velocity fluctuation
w_e	Entrainment rate at the inversion layer
w_f	Weighting factor (in MYNN for calculating PBLH)
w_s	Mixed layer velocity scale
w_{s0}	Mixed layer velocity scale at height = $0.5h$
z	Model level height
z_1	Height of the first model level
z_s	Estimated height in YSU
β_{entr}	Bower ratio at the interfacial layer
β_{sfc}	Bowen ratio at the land surface
γ_ψ	Correction to the local gradient in YSU
Δ	Saturated vapour pressure curve
Δt	Time interval
$\Delta\psi _{zi}$	Jump of the variable ψ at the inversion layer (in YSU)
η	Soil moisture
θ	Potential temperature

θ_e	Equivalent potential temperature
θ_s	Virtual potential temperature close to the land surface
θ_v	Virtual potential temperature
θ_v'	Virtual potential temperature fluctuation
κ	von Karman constant
κ_h	Surface soil thermal conductivity
λ	Latent heat of vaporization
λE	Latent heat flux
ρ	Density
Φ_h	Nondimensional profile function for heat
Φ_m	Nondimensional profile function for momentum
ψ'	Fluctuation of momentum or a scalar variable

9. List of tables

Table 1. The WRF experiments with the selected PBL schemes, surface layer schemes, and LSMs.	16
Table 2. Complete configuration of NOAH-MP as deployed in this study.	22
Table 3. Parameterizations of the mixing length scale (l) as deployed in MYNN and MYJ. l_s is l in the surface layer, l_t is the turbulent length scale, and l_b is l related to the buoyancy force, κ is the von Karman constant, L is the MO length scale and w_c is a velocity scale, N is the Brunt-Väisälä frequency, z is the height of a model level, and z_i is the PBLH.	25
Table 4. Parameterizations used in YSU and ACM2: $z_s = \min(z, 0.1z_i)$ for unstable and $z_s = z$ for stable conditions. w_s is the turbulent velocity scale, w_{s0} is w_s at $z = 0.5h$, $\overline{(w'\psi')_0}$ is the surface flux. w_e is the entrainment rate at the inversion layer, and $\Delta\psi _{z_i}$ is the jump of the variable ψ at the inversion layer. Φ is a nondimensional profile function, κ is the von Karman constant, subscripts m and h stand for momentum and scalar variables (heat and moisture), respectively. Detailed parameterizations can be found in Hong et al. (2006) and Pleim (2007).	27
Table 5. The diagnostics extracted from the mixing diagram at Figure 13: Mean ratio between sensible and latent heat flux at the interfacial layer (β_{entr}), the mean ratios of the fluxes of latent ($A_{\lambda E}$) and sensible heat (A_H) at the land surface to those at the interfacial layer are also diagnosed from the mixing diagrams, the mean quantified impact of moisture ($AD_{\lambda E}$) and heat (AD_H) horizontal advection. Only the mean surface Bowen ratio (β_{surf}) is calculated from the model output. All the mean variables are values averaged over 10-hour period (from 7 UTC to 17 UTC) on 8 September 2009 for the six experiments.	46
Table 6. The diagnostics extracted from the mixing diagrams at Figure 36 for R1 and R2: The mean ratio between sensible and latent heat flux at the interfacial layer (β_{entr}), the mean ratios of latent ($A_{\lambda E}$) and sensible heat (A_H) at the land surface to those at the	

interfacial layer, the mean quantified impact of horizontal advection of moisture ($AD_{\lambda E}$) and heat (AD_H). The mean surface Bowen ratio (β_{surf}) is calculated from the model output. All the mean variables are averaged temporally over 6.5 (9) hours and spatially over R1 (R2) on 25 August 2009 for the six experiments. Values extracted from for R1 and R2 in separated columns.75

10. List of figures

- Figure 1. Schematic representation of the PBL diurnal evolution. The arrows denote the mean direction of heat and moisture transport. Circles with arrows represent turbulent eddies, which form the main mechanism of transportation in the convective PBL. ...3
- Figure 2. Schematic representation of the SVA system (Wulfmeyer et al., 2015a).....4
- Figure 3. SVA feedback loops showing positive (red arrows) and negative (blue arrows) feedbacks of sensible heat flux (H) on PBL evolution (left), and of soil moisture η on latent heat flux (λE) and precipitation P (right). The grey arrow depicts an impact that can be both positive and negative. z_i is the PBLH, while θ and q are symbols for potential temperature and humidity, respectively. The black vertical upward arrows next to H , P , λE and η indicate an increase. Adapted from van Heerwaarden et al. (2009) and Seneviratne et al. (2010).5
- Figure 4. The outer within the red boundaries and the inner domain in the white boundaries for the WRF simulations along with the orography field (in m ASL). ... 15
- Figure 5. Schematic representation of the preformed WRF simulations in the corresponding time frames, with denoted dates of the case studies. 18
- Figure 6. Schematic representation of the “weather forecast mode”. Start denotes the start date and N is the number of simulated days. 18
- Figure 7. The WVDIAL scans of absolute humidity on 8 September 2009. The starting time of the each scan in UTC is denoted in the lower left corner of the corresponding panel. The duration of the each scan was approximately 24 minutes. White rectangles on the scans denote the area (3 km in horizontal and 2.5 km in vertical direction) over which the measured data were averaged to obtain the absolute humidity profiles....32

- Figure 8. The mixing diagram - an example of diurnal coevolution of $Cp\theta$ vs. λq from 7 to 17 UTC, with vectors (dashed lines with arrows) and their components (horizontal and vertical dashed lines) that contribute to the PBL total flux.....33
- Figure 9. Comparisons of the measured absolute humidity profiles (black dots) with the profiles simulated with WRF configured with the four PBL schemes (ACM2 in blue, MYJ in red, MYNN in green and YSU in purple) and the NOAH LSM. Shaded grey areas correspond to the standard deviation of the scans due to averaging.....37
- Figure 10. Comparisons of the WVDIAL absolute humidity profiles with the profiles simulated with WRF configured with the two PBL schemes (MYNN and YSU) and the two LSMs (NOAH and NOAH-MP). Turquoise lines show MYNN with NOAH-MP and brown YSU with NOAH-MP. Remaining colours as in Figure 9.....39
- Figure 11. Skew T -log p diagram (a) showing dew point temperature (right profiles) and air temperature profiles (left profiles) at 16 UTC 8 September 2009 as simulated with the six WRF runs along with the radiosonde measurements. Lines perpendicular to the left vertical axis of the diagram are the LCL values in hPa as calculated from the simulations and the measurements. On (b) the potential temperature profiles valid at 16 UTC as simulated with the six model simulations and measured with the radiosonde. Colours of the lines depicted in the legend located in the lower right corner of the (b), with RS standing for radiosonde measurements.40
- Figure 12. Temporal change of PBLH from WRF compared with the PBLH estimates obtained from the WVDIAL measurements (black dots) on 8 September 2009 between 7 and 17 UTC. The PBLH from the model is calculated using the virtual potential lapse rate method (panel a) and the bulk Richardson method (panel b).....42
- Figure 13. Mixing diagrams for 8 September 2009 between 7 and 17 UTC. The simulated coevolutions of moisture content λq and heat content $Cp\theta$ are in solid lines, while dashed lines stand for vectors corresponding to the surface (\mathbf{V}_{sfc}), advected (\mathbf{V}_{adv}) and entrainment (\mathbf{V}_{entr}) fluxes. The simulations with the 4 PBL schemes coupled with NOAH are on panel (a), and on (b) are the simulations with MYNN and YSU in combination with NOAH and NOAH-MP. Colours of the lines correspond the

experiments as denoted in the legend in the upper right corner of panel (b). Overlaid are lines of constant θ_e (in K; black dashed) and RH (in %; orange dashed).44

Figure 14. Simulations of the temporal change of (a) sensible heat flux (H), (b) latent heat flux (λE), (c) ground heat flux (G), and (d) net radiation flux (R_n) on 8 September 2009 from 7 to 17 UTC.....48

Figure 15. Simulations of the temporal change of (a) the temperature at the first model level (T), (b) the surface temperature (T_{skin}), (c) the surface exchange coefficient for heat and moisture divided by the friction velocity (C_h) and (d) the temperature in the first soil layer (T_{s1}) on 8 September 2009 from 7 to 17 UTC.49

Figure 16. Vertical profiles of (a) the mixing length scale (l), and (b) TKE on 8 September 2009 at 16 UTC as simulated with WRF configured with the local MYN and MYNN schemes.50

Figure 17. Temporal change of mixing ratio vertical profiles q in gkg^{-1} from 7 to 18 UTC on 8 September 2009 at the study site, as simulated with WRF configured with MYNN and NOAH (a), YSU and NOAH (b), MYNN and NOAH-MP (c), and YSU and NOAH-MP (d).52

Figure 18. Temporal change of the difference between the NOAH and NOAH-MP mixing ratio profiles in gkg^{-1} for the simulations with MYNN (e) and YSU (f) PBL schemes.53

Figure 19. The model domains with the orography field (left panel), with the study area (the red square). The site locations are given in blue stars. More detailed with field management around the Kraichgau (KC) station (upper right panel) and the Swabian Alb (SA) station (bottom right panel).56

Figure 20. Synoptic weather map (a) and the satellite image of clouds over Europe (b) on 25 August 2009 at 12 UTC. The orange square show the location of the study area. The source – DWD/EUMETSAT.57

- Figure 21. Radar images of rainfall at 6:30 UTC, 10 UTC, 16 UTC and 22 UTC (a), and the 24 hour precipitation on 25 August 2009 (b) as observed on the DWD weather stations. The black box shows the boundaries of the analysed domain. The source – DWD.....57
- Figure 22. Horizontal distribution of soil moisture content in m^3m^{-3} (shaded) in the first 10 cm of soil on 25 August 2009 at 6 UTC as simulated with the 6 experiments. The overlaid lines denote soil temperature (K) in the same soil layer over the study area, with contour interval of 2 K. The black and red boxes denote boundaries of the R1 and R2 regions, respectively.....59
- Figure 23. Differences in simulated soil moisture in the top soil layer in ($\text{m}^{-3}\text{m}^{-3}$) between NOAH and NOAH-MP coupled with MYNN (a) and YSU (b); differences in simulated soil temperature in the top soil layer in (K) between NOAH and NOAH-MP coupled with MYNN (c) and YSU (d). The results are valid on 25 August 2009 at 6 UTC over the analysed area.60
- Figure 24. Accumulated rain in mm over 24 h period on 25 August 2009 within the study area as simulated with the 6 experiments. The simulated locations and amount of maximum precipitation are denoted in blue letters, and in black dots are locations of RU 1695 measurements sites. Boxes as in Figure 22.61
- Figure 25. Hourly accumulated precipitation in mm on 25 August 2009 averaged over the study area. In the upper right corner the areal mean of the accumulated 24 h precipitation for the each experiment.62
- Figure 26. Number of grid cells with hourly precipitation $> 10 \text{ mmh}^{-1}$ on 25 August 2009 within R1 (a) and R2 (b). Total number of grid cells with hourly precipitation $> 10 \text{ mmh}^{-1}$ are placed in the upper right corner of the each panel.63
- Figure 27. Locations of the maximum hourly precipitation on 25 August 2009 within R1 (black box) and R2 (red box), with the simulated time of occurrence in UTC hours, denoted in colours corresponding to the experiments. The amounts of the maximum precipitation for the both regions in mmh^{-1} are given in the upper right corner.64

Figure 28. Radiation at the top of the atmosphere (Wm^{-2}) as simulated with the experiments on 25 August 2009 at the time denoted in the lower left corners of the each panel. The R1 region is enclosed with the black box. The experiment names are denoted in the upper right corners of the each panel.65

Figure 29. As in Figure 28 at 15 UTC, with R2 denoted in black boxes.66

Figure 30. Horizontal distribution of mixing ratio in gkg^{-1} (shaded) with overlaid wind vectors (ms^{-1}) and temperature lines with contour interval of 2 K (navy blue lines) as simulated at the first model level on 25 August 2009 at 11 UTC.....67

Figure 31. As in Figure 30 at 15 UTC, with R2 region denoted in the black boxes.68

Figure 32. Vertical cross-sections of precipitable water in mm (shaded) and vertical wind velocity in ms^{-1} (solid black lines) on 25 August 2009 along the horizontal lines through the locations with the maximum hourly precipitation in R1 (shown in Figure 27 at times prior to the maximum precipitation event which is denoted in upper left corners of the panels). Red arrows denote the exact locations with the hourly maximums.....69

Figure 33. As in Figure 32, but along the horizontal lines through the locations with the maximum hourly precipitation in R2.....70

Figure 34. Simulated profiles of virtual (right profiles) and dew-point temperature (left profiles) in the SkewT – logp diagram on 25 August 2009 at 6 UTC (a) and 11 UTC (b). The obtained profiles are spatially averaged over the grid-cells with precipitation over 30 mm between 12 and 18 UTC. Averaged values of CAPE in (J) are given in the upper right corners. Colours of the profiles and CAPE values correspond to the experiments as denoted in the legend in the lower left corner of the panel (a).72

Figure 35. As in Figure 34 at 6 UTC (a) and 15 UTC (b) for the grid cells in the R2 region. CAPE for the morning sounding is not denoted since all the values equal to zero.....73

- Figure 36. Mixing diagrams for 25 August 2009 averaged over R1 between 6 and 13:30 UTC (a) and over R2 between 6 and 15 UTC (b). The simulated coevolution of moisture λq and heat content $Cp\theta$ are in solid lines, while dashed lines stand for vectors corresponding to the surface (\mathbf{V}_{sfc}), advected (\mathbf{V}_{adv}) and entrainment (\mathbf{V}_{entr}) fluxes. Colours of the lines correspond to the experiments as denoted in the legend in the upper right corner of the panel (b). Overlaid are lines of constant θ_e (in K; black dashed) and RH (in %; orange dashed).....74
- Figure 37. Simulations of temporal change of (a) the temperature at the first model level (T), (b) the surface temperature T_{skin} , (c) the temperature in the first soil layer T_{s1} , and the surface exchange coefficient for scalar variables C_h divided by the friction velocity (d) on 25 August 2009 between 6 and 17 UTC.78
- Figure 38. Temporal change of vertical profiles of q in gkg^{-1} from 6 to 18 UTC on 25 August 2009 averaged over the R1 region. Overlaid are lines for θ (black; K) and the PBLH (white; km).....79
- Figure 39. Temporal change of mixing length scale l in m from 6 to 18 UTC on 25 August 2009 averaged over the R1 region, as simulated with WRF configured with MYJ (a), MYNN (b), MYNN-MP (c). Overlaid are lines for TKE (black; Jkg^{-1}) and the PBLH (white; km).....80
- Figure 40. Temporal change of the eddy diffusivity for scalars K_h from 6 to 18 UTC on 25 August 2009 averaged over the R1 region, as simulated with WRF configured with MYJ (a), MYNN (b), MYNN-MP (c), YSU (d), MYNN-MP (e), and YSU-MP (d). Overlaid white lines denote the PBLH.81
- Figure 41. The simulated time series of the PBLH and LFC on 25 August 2009 averaged over the grid cells with accumulated precipitation exceeding 30 mm between 13 and 18 UTC in R1.....82
- Figure 42. Simulations of the temporal change of (a) sensible heat flux (H), (b) latent heat flux (λE), (c) ground heat flux (G), and (d) Evaporative fraction (EF) on 25 August 2009 from 6 to 16 UTC.84

Figure 43. Mean EF versus $PBLH$ averaged over the R1 and R2 region averaged between 6 and 16 UTC. The colours of the markers correspond to the experiment as denoted in the upper left corner, and the shape to the region (circles to R1, diamonds to R2)...85

11. Bibliography

- Ament, F. and C. Simmer (2006), Improved Representation of Land-surface Heterogeneity in a Non-hydrostatic Numerical Weather Prediction Model, *Bound.-Layer Meteor.*, 121, 1, 153-174, doi:10.1007/s10546-006-9066-4.
- Angevine, W. (2008), Transitional, entraining, cloudy, and coastal boundary layers, *Acta Geophys.*, 56, 2–20, doi:10.2478/s11600-007-0035-1.
- Angevine, W. M., E. Bazile, D. Legain, and D. Pino (2014), Land surface spinup for episodic modeling, *Atmos. Chem. Phys.*, 14, 8165-8172, doi:10.5194/acp-14-8165-2014.
- Ansmann, A., Fruntke, J., and Engelmann, R. (2010). Updraft and downdraft characterization with Doppler lidar: cloud-free versus cumuli-topped mixed layer. *Atmos. Chem. Phys.*, 10, 7845–7858, doi:10.5194/acp-10-7845-2010.
- Ball, J. T., I. Woodrow, and J. Berry (1987), A Model Predicting Stomatal Conductance and its Contribution to the Control of Photosynthesis under Different Environmental Conditions, In J. Biggins (Eds.), *Progress in Photosynthesis Research*, Springer Netherlands, 221–224, doi:10.1007/s00442-007-0951-4.
- Balsamo, G., P. Viterbo, A. Beljaars, B. van der Hurk, M. Hirschi, A. K. Betts and K. Scipal (2009), A Revised Hydrology for the ECMWF Model: Verification from Field Site to Terrestrial Water Storage and Impact in the Integrated Forecast System, *J. Hydrometeorolo.*, 10, 623-643, doi:10.1175/2008JHM1068.1.
- Behrendt, A., A. Blyth, M. Dorninger, N. Kalthoff, C. Flamant, P. Di Girolamo, and E. Richard (2013), Convective Precipitation in complex terrain: Results of the COPS campaign, *Meteorol. Z.*, 22, 367–372, doi: 10.1127/0941-2948/2013/0541.
- Behrendt, A., V. Wulfmeyer, A. Riede, G. Wagner, S. Pal, H. S. Bauer, M. Radlach, and F. Späth (2009), 3-Dimensional observations of atmospheric humidity with a scanning differential absorption lidar, *Proceedings of SPIE - The International Society for Optical Engineering*, 7475, Article number 74750L, doi:10.1117/12.835143.
- Behrendt, A., V. Wulfmeyer, E. Hammann, S. K. Muppa, and S. Pal (2015), Profiles of second- to fourth-order moments of turbulent temperature fluctuations in the

- convective boundary layer: first measurements with rotational Raman lidar, *Atmos. Chem. Phys.*, 15, 5485-5500, doi:10.5194/acp-15-5485-2015.
- Betts, A. K. (1992), FIFE atmospheric boundary layer budget methods, *J. Geophys. Res.*, 97, 18523–18532, doi:10.1029/91JD03172.
- Betts, A. K. (2007), Coupling of water vapour convergence, clouds, precipitation, and land-surface processes, *J. Geophys. Res.*, 112, D10108, doi:10.1029/2006JD008191.
- Betts, A. K. (2009), Land-surface-atmosphere coupling in observations and models, *J. Adv. Model Earth Syst.*, 1 (4), 18 pp., doi:10.3894/JAMES.2009.1.4
- Bhawar, R., P. Di Girolamo, D. Summa, C. Flamant, D. Althausen, A. Behrendt, C. Kiemle, P. Bossler, M. Cacciani, C. Champollion, T. Di Iorio, R. Engelmann, C. Herold, S. Pal, A. Riede, M. W. Wirth, and V. Wulfmeyer (2011), The water vapour intercomparison effort in the framework of the Convective and Orographically-induced Precipitation Study: airborne-to-ground-based and airborne-to-airborne lidar systems, *Q. J. R. Meteorol. Soc.*, 137, 325–348, doi:10.1002/qj.697.
- Blackadar, A. K. (1962), The vertical distribution of wind and turbulent exchange in a neutral atmosphere, *J. Geophys. Res.*, 67, 3095-3102, 1962.
- Blay-Carreras, E., D., Pino, J. Vilà-Guerau de Arellano, A. van de Boer, O. De Coster, C. Darbieu, O. Hartogensis, F. Lohou, M. Lothon, and H. Pietersen (2014), Role of the residual layer and large-scale subsidence on the development and evolution of the convective boundary layer, *Atmos. Chem. Phys.*, 14, 4515-4530, doi:10.5194/acp-14-4515-2014, 2014.
- Bonan, G. B. (2008), *Ecological climatology: Concepts and applications*. Cambridge: Cambridge University Press.
- Borge, R., V. Alexandrov, J. J. del Vas, J. Lumbreras, and E. Rodríguez (2008), A comprehensive sensitivity analysis of the WRF model for air quality applications over the Iberian Peninsula, *Atmos. Environ.*, 42, 8560-8574, doi:10.1016/j.atmosenv.2008.08.032.
- Branch, O. (2014), The impact of irrigated biomass plantations on mesoscale climate in coastal arid regions, Doctoral dissertation, Retrieved from the Hohenheim library

- Branch, O., K. Warrach-Sagi, V. Wulfmeyer, and S. Cohen (2014), Simulation of semi-arid biomass plantations and irrigation using the WRF-NOAH model – a comparison with observations from Israel, *Hydrol. Earth Syst. Sci.*, 18, 1761-1783, doi:10.5194/hess-18-1761-2014.
- Bruyère, C. L., J. M. Done, G. J. Holland, and S. Fredrick (2013), Bias corrections of global models for regional climate simulations of high-impact weather, *Clim. Dyn.*, 43, 1847–1856, doi:10.1007/s00382-013-2011-6.
- Chen, F., and J. Dudhia (2001a), Coupling an Advanced Land Surface–Hydrology Model with the Penn State–NCAR MM5 Modeling System. Part I: Model Implementation and Sensitivity, *Mon. Wea. Rev.*, 129, 569–585, doi:http://dx.doi.org/10.1175/1520-0493(2001)129<0569:CAALSH>2.0.CO;2.
- Chen, F., and J. Dudhia, (2001b), Coupling an Advanced Land Surface–Hydrology Model with the Penn State–NCAR MM5 Modeling System. Part II: Preliminary Model Validation, *Mon. Wea. Rev.*, 129, 587–604, doi:http://dx.doi.org/10.1175/1520-0493(2001)129<0587:CAALSH>2.0.CO;2.
- Chen, F., Z. Janjić, and K. Mitchell (1997), Impact of atmospheric surface layer parameterizations in the new land surface scheme of the NCEP mesoscale Eta model, *Bound. Lay. Meteorol.*, 85, 391–421, doi:10.1023/A:1000531001463.
- Cheng, Y., V. M. Canuto, and A. M. Howard (2002), An improved model for the turbulent PBL, *J. Atmos. Sci.*, 59, 1550-1565, doi:http://dx.doi.org/10.1175/1520-0469(2002)059<1550:AIMFTT>2.0.CO;2
- Cohen, A. E., S. M. Cavallo, M. C. Coniglio, and H. E. Brooks (2015), A Review of Planetary Boundary Layer Parameterization Schemes and Their Sensitivity in Simulating Southeastern U.S. Cold Season Severe Weather Environments, *Weather and Forecasting*, 30(3), 591-612, doi:10.1175/WAF-D-14-00105.1.
- Coniglio, M. C., J. Correia, P. T. Marsh, and F. Kong (2013), Verification of Convection-Allowing WRF Model Forecasts of the Planetary Boundary Layer Using Sounding Observations, *Wea. Forecasting*, 28, 842–862, doi:http://dx.doi.org/10.1175/WAF-D-12-00103.1.

- Cooper, D. I., W. E. Eichinger, J. Archuleta, L. Hipps, C. M. U. Neale, and J. H. Prueger (2007), An Advanced Method for Deriving Latent Energy Flux from a Scanning Raman Lidar, *Agron. J.*, 99, 272-284, doi:10.2134/agronj2005.0112S.
- Corsmeier, U., N. Kalthoff, Ch. Barthlott, A. Behrendt, P. Di Girolamo, M. Dorninger, F. Aoshima, J. Handwerker, Ch. Kottmeier, H. Mahlke, St. Mobbs, G. Vaughan, J. Wickert, and V. Wulfmeyer (2011), Driving processes for deep convection over complex terrain: A multiscale analysis of observations from COPS-IOP 9c, *Q. J. R. Meteorol. Soc.*, 137, 137–155, doi:10.1002/qj.754.
- Cuijpers, J. W. M., and A. A. M. Holtslag, 1998: Impact of skewness and nonlocal effects on scalar and buoyancy fluxes in convective boundary layers, *J. Atmos. Sci.*, 55, 151–162, doi:10.1175/1520-0469(1998)055<0151:IOSANE>2.0.CO;2.
- Darbieu, C., F. Lohou, M. Lothon, J. Vilà-Guerau de Arellano, F. Couvreux, P. Durand, D. Pino, E. G. Patton, E. Nilsson, E. Blay-Carreras, and B. Gioli (2015), Turbulence vertical structure of the boundary layer during the afternoon transition, *Atmos. Chem. Phys.*, 15, 10071-10086, doi:10.5194/acp-15-10071-2015.
- Dirmeyer, P. A., B. A. Cash, J. L. Kinter III, C. Stan, T. Jung, L. Marx, P. Towers, N. Wedi, J. M. Adams, E. L. Altshuler, B. Huang, E. K. Jin, and J. Manganello (2012), Evidence for Enhanced Land–Atmosphere Feedback in a Warming Climate, *J. Hydrometeorol.*, 13(3), 981-995, doi:10.1175/JHM-D-11-0104.1.
- Ek, M. B., and A. A. M. Holtslag, (2004), Influence of Soil Moisture on Boundary Layer Cloud Development, *J. Hydrometeorol.*, 5, 86–99, doi: 10.1175/1525-7541(2004)005<0086:IOSMOB>2.0.CO;2.
- Ek, M. B., K. E. Mitchell, Y. Lin, E. Rogers, P. Grunmann, V. Koren, G. Gayno, and J. D. Tarpley (2003), Implementation of Noah land surface model advances in the National Centres for Environmental Prediction operational mesoscale Eta model, *J. Geophys. Res.*, 108, D22, 8851, doi:10.1029/2002JD003296.
- Ek, M., and Mahrt, L., 1994. Daytime evolution of relative-humidity at the boundary-layer top, *Mon. Weather Rev.* 122 (12), 2709–2721, doi:http://dx.doi.org/10.1175/1520-0493(1994)122<2709:DEORHA>2.0.CO;2

- Findell, K. L. and E. A. B. Eltahir (2003a), Atmospheric Controls on Soil Moisture–Boundary Layer Interactions. Part I: Framework Development, *J. Hydrometeor.*, 4:3, 552–569, doi:[http://dx.doi.org/10.1175/1525-7541\(2003\)004<0570:ACOSML>2.0.CO;2](http://dx.doi.org/10.1175/1525-7541(2003)004<0570:ACOSML>2.0.CO;2)
- Findell, K. L. and E. A. B. Eltahir (2003b), Atmospheric Controls on Soil Moisture–Boundary Layer Interactions. Part II: Feedbacks within the Continental United States, *J. Hydrometeor.*, 4:3, 570–583, doi:[http://dx.doi.org/10.1175/1525-7541\(2003\)004<0570:ACOSML>2.0.CO;2](http://dx.doi.org/10.1175/1525-7541(2003)004<0570:ACOSML>2.0.CO;2).
- Findell, K. L., P. Gentine, B. R. Lintner, and C. Kerr (2011), Probability of afternoon precipitation in eastern United States and Mexico enhanced by high evaporation. *Nat. Geosci.* 4, 434–439, doi:10.1038/ngeo1174
- García-Díez, M., J. Fernández, L. Fita, and C. Yagüe, (2013), Seasonal dependence of WRF model biases and sensitivity to PBL schemes over Europe, *Q. J. R. Meteorol. Soc.*, 139, 501–514, doi:10.4236/ajcc.2014.35042.
- Gayler, S., T. Wohling, M. Grzeschik, J. Ingwersen, H.-D. Wizemann, K. Warrach-Sagi, P. Hogy, S. Attinger, T. Streck, and V. Wulfmeyer (2014), Incorporating dynamic root growth enhances the performance of Noah-MP at two contrasting winter wheat field sites, *Water Resour. Res.*, 50, 1337–1356, doi:10.1002/2013WR014634.
- Gentine, P., A. A. M. Holtslag, F. D’Andrea, and M. Ek (2013), Surface and Atmospheric Controls on the Onset of Moist Convection over Land, *J. Hydrometeor.*, 14, 1443–1462, doi:<http://dx.doi.org/10.1175/JHM-D-12-0137.1>
- Goulart, A., B. Bodmann, M. Vilhena, P. Soares, and D. Moreira (2010), On the Time Evolution of the Turbulent Kinetic Energy Spectrum for Decaying Turbulence in the Convective Boundary Layer, *Bound.-Lay. Meteorol.*, 138, 61–75, doi:10.1007/s10546-010-9546-4.
- Grisogono, B., and D. Belušić, (2008), Improving mixing length-scale for stable boundary layers, *Quart. J. Roy. Meteor. Soc.*, 134, 2185–2192, doi:10.1002/qj.347.
- Guillod, B., E. Davin, C. Köndig, G. Smittek, and S. Seneviratne (2013), Impact of soil map specifications for European climate simulations, *Clim. Dyn.*, 40, 123–141, doi:<http://dx.doi.org/10.1175/JHM-362.1>.

- Guilod B. P., Orlowsky B., Miralles D. G., Teuling A. J., and S. I. Seneviratne (2015), Reconciling Spatial and Temporal Soil Moisture Effects on Afternoon Rainfall, *Nat. Commun.*, **6**, 6443, doi:10.1038/ncomms7443.
- Guo, Z., P.A. Dirmeyer, R.D. Koster, G.B. Bonan, E. Chan, P. Cox, C.T. Gordon, S. Kanae, E. Kowalczyk, D.M. Lawrence, P. Liu, C.H. Lu, S. Malyshev, B. McAvaney, K. Mitchell, D. Mocko, T. Oki, K. Oleson, A. Pitman, Y.C. Sud, C.M. Taylor, D. Verseghy, R. Vasic, Y. Xue, and T. Yamada (2006) GLACE: The global land-atmosphere coupling experiment. Part II: Analysis. *J. Hydrol.*, **7**, 611-625, doi:10.1175/JHM511.1.
- Hamilton, S.K., J.E. Doll, and G.P. Robertson, editors, (2015), *The ecology of agricultural landscapes: Long-term research on the path to sustainability*, Oxford University Press, New York, USA, 448 pp.
- Hammann, E., A. Behrendt, F. Le Mounier, and V. Wulfmeyer (2015), Temperature profiling of the atmospheric boundary layer with rotational Raman lidar during the HD(CP)² Observational Prototype Experiment, *Atmos. Chem. Phys.*, **15**, 2867-2881, doi:10.5194/acp-15-2867-2015.
- Hohenegger, C., P. Brockhaus, C. S. Bretherton, and C. Schär (2009), The Soil Moisture–Precipitation Feedback in Simulations with Explicit and Parameterized Convection, *Journal of Climate* **22**(19), 5003-5020, doi:10.1175/2009JCLI2604.1
- Holtslag, A. A. M., and B. A. Boville (1993), Local Versus Nonlocal Boundary-Layer Diffusion in a Global Climate Model, *J.Clim.*, **6**, 1825-1842, doi:http://dx.doi.org/10.1175/1520-0442(1993)006<1825:LVNBLD>2.0.CO;2.
- Hong, S.-Y., Y. Noh, and J. Dudhia (2006), A New Vertical Diffusion Package with an Explicit Treatment of Entrainment Processes, *Mon. Wea. Rev.*, **134**, 2318-2341, doi:http://dx.doi.org/10.1175/MWR3199.1.
- Hong, S.-Y., and H.-L. Pan, (1996) Nonlocal boundary layer vertical diffusion in a medium-range forecast model, *Mon. Wea. Rev.*, **124**, 2322–2339, doi:10.1175/1520-0493(1996)124,2322:NBLVDI.2.0.CO;2.

- Hu, X.-M., J. W. Nielsen-Gammon, and F. Zhang (2010), Evaluation of Three Planetary Boundary Layer Schemes in the WRF Model, *J. Appl. Meteor. Climatol.*, 49, 1831–1844, doi:<http://dx.doi.org/10.1175/2010JAMC2432.1>.
- Huang, H.-Y., A. Hall, and J. Teixeira (2013), Evaluation of the WRF PBL parameterizations for marine boundary layer clouds: Cumulus and stratocumulus. *Mon. Wea. Rev.*, 141, 2265–2271, doi:10.1175/MWR-D-12-00292.1.
- Ingwersen, J., K. Steffens, P. Högy, K. Warrach-Sagi, D. Zhunusbayeva, M. Poltoradnev, R. Gäbler, H. D. Wizemann, A. Fangmeier, V. Wulfmeyer, and T. Streck (2011), Comparison of Noah simulations with eddy covariance and soil water measurements at a winter wheat stand, *Agric. For. Meteorol.*, 151, 345-355, doi:10.1016/j.agrformet.2010.11.010.
- Ingwersen, J., K. Imukova, P. Högy, and T. Streck (2015), On the use of the post-closure methods uncertainty band to evaluate the performance of land surface models against eddy covariance flux data, *Biogeosciences*, 12, 2311-2326, doi:10.5194/bg-12-2311-2015.
- Janjić, Z. (2002), Nonsingular Implementation of the Mellor-Yamada Level 2.5 Scheme in the NCEP Meso model. National Centres for Environmental Prediction, (pp. 61), <http://www.emc.ncep.noaa.gov/officenotes/newernotes/on437.pdf>
- Jarvis, P. G. (1976), The Interpretation of the Variations in Leaf Water Potential and Stomatal Conductance Found in Canopies in the Field, *Phil. Trans. R. Soc. Lond. B.*, 273, 593-610, doi:10.1098/rstb.1976.0035.
- Jeričević, A. and B. Grisogono (2006), The critical bulk Richardson number in urban areas: verification with application in a numerical weather prediction model, *Tellus*, 58A, 19-27, doi:10.1111/j.1600-870.2006.00153.x
- Jiménez, P. A., J. Dudhia, J. F. González-Rouco, J. Navarro, J. P. Montávez, and E. García-Bustamante (2012), A Revised Scheme for the WRF Surface Layer Formulation, *Mon. Wea. Rev.*, 140, 898–918, doi:<http://dx.doi.org/10.1175/MWR-D-11-00056.1>.

- Kain, J. S. (2004), The Kain–Fritsch Convective Parameterization: An Update, *J. Appl. Meteor. Climatol.*, 43, 170–181, doi:[http://dx.doi.org/10.1175/1520-0450\(2004\)043<0170:TKCPAU>2.0.CO;2](http://dx.doi.org/10.1175/1520-0450(2004)043<0170:TKCPAU>2.0.CO;2).
- Kendon, E. J., N. M. Roberts, C. A. Senior, and M. J. Roberts (2012), Realism of Rainfall in a Very High-Resolution Regional Climate Model, *J. Climate*, 25(17), 5791–5806, doi:10.1175/JCLI-D-11-00562.1
- Khodayar Pardo, S. (2009), High-resolution analysis of the initiation of deep convection forced by boundary-layer processes, Doctoral dissertation, Retrieved from https://www.imk-tro.kit.edu/download/Khodayar_diss.pdf
- Kleczek, Michal A., Gert-Jan Steeneveld, and Albert AM Holtslag (2014) Evaluation of the weather research and forecasting mesoscale model for GABLS3: impact of boundary-layer schemes, boundary conditions and spin-up, *Bound.-Lay. Meteorol.*, 152.2 (2014): 213–243.
- Klüpfel, V., N. Kalthoff, L. Gantner, and C. M. Taylor (2012), Convergence zones and their impact on the initiation of a mesoscale convective system in West Africa, *Q. J. R. Meteorol. Soc.*, 138, 950–963. doi:10.1002/qj.979
- Knist, S., K. Goergen, E. Buonomo, O. B. Christensen, A. Colette, R. M. Cardoso, R. Fealy, J. Fernandez, M. Garcia-Diez, D. Jacob, S. Kartsios, E. Katragkou, K. Keuler, S. Mayer, E. van Meijgaard, G. Nikulin, P. M. M. Soares, S. Sobolowski, G. Szepszo, C. Teichmann, R. Vautard, K. Warrach-Sagi, V. Wulfmeyer, and C. Simmer (2016), Land-atmosphere coupling in EURO-CORDEX evaluation experiments, submitted to *J. Geophys. Res. Atmos.*
- Koster, R. D., Y. C. Sud, Z. Guo, P. A. Dirmeyer, G. Bonan, K. W. Oleson, E. Chan, D. Verseghy, P. Cox, H. Davies, E. Kowalczyk, C. T. Gordon, S. Kanae, D. Lawrence, P. Liu, D. Mocko, C.-H. Lu, K. Mitchell, S. Malyshev, B. McAvaney, T. Oki, T. Yamada, A. Pitman, C. M. Taylor, R. Vasic, and Y. Xue (2006), GLACE: The Global Land–Atmosphere Coupling Experiment. Part I: Overview, *J. Hydrometeorol.*, 7, 590–610, doi:<http://dx.doi.org/10.1175/JHM510.1>.
- Kotlarski, S., K. Keuler, O. B. Christensen, A. Colette, M. Deque, A. Gobiet, K. Goergen, D. Jacob, D. Luethi, E. van Meijgaard, G. Nikulin, C. Schaer, C. Teichmann, R. Vautard, K. Warrach-Sagi, and V. Wulfmeyer (2014), Regional climate modeling on

- European scales: a joint standard evaluation of the EURO-CORDEX RCM ensemble, *Geosci. Model Dev.*, 7, 1297-1333. doi:10.5194/gmd-7-1297-2014
- Kumar A., F. Chen, D. Niyogi, J. Alfieri, M. Ek, and K. Mitchell (2011), Evaluation of a Photosynthesis-based Canopy Resistance Formulation in the Noah Land Surface Model, *Bound.-Layer Meteorol.*, 138, 263-284, doi:10.1007/s10546-010-9559-z.
- LeMone, M. A., M. Tewari, F. Chen, and J. Dudhia (2013), Objectively Determined Fair-Weather CBL Depths in the ARW-WRF Model and Their Comparison to CASES-97 Observations, *Mon. Wea. Rev.*, 141, 30–54, doi:http://dx.doi.org/10.1175/MWR-D-12-00106.1.
- Lenderink, G. and E. van Meijgaard (2008), Increase in hourly precipitation extremes beyond expectations from temperature changes, *Nat. Geosci.*, 1, 511–514, doi:10.1038/ngeo262
- Lenschow, D. H., J. Mann, and L. Kristensen (1994), How Long Is Long Enough When Measuring Fluxes and Other Turbulence Statistics?, *J. of Atmos. Oceanic Technol.*, 11, 661-673, doi:http://dx.doi.org/10.1175/1520-0426(1994)011<0661:HLILEW>2.0.CO;2.
- Lenschow, D. H., M. Lothon, S. D. Mayor, P. P. Sullivan, and G. Canut (2012), A Comparison of Higher-Order Vertical Velocity Moments in the Convective Boundary Layer from Lidar with In Situ Measurements and Large-Eddy Simulation, *Bound. Lay. Meteorol.*, 143, 107–123, doi:10.1007/s10546-011-9615-3.
- Mahmood, R., R. A. Pielke, K. G. Hubbard, D. Niyogi, P. A. Dirmeyer, C. McAlpine, A. M. Carleton, R. Hale, S. Gameda, A. Beltrán-Przekurat, B. Baker, R. McNider, D. R. Legates, M. Shepherd, J. Du, P. D. Blanken, O. W. Frauenfeld, U. S. Nair, and S. Fall (2013), Land cover changes and their biogeophysical effects on climate, *Int. J. Climatol.*, 34, 929–953, doi:10.1002/joc.3736.
- Mahrt, L., and M. Ek (1984), The Influence of Atmospheric Stability on Potential Evaporation, *J. Climate Appl. Meteorol.*, 23, 222-234, doi:http://dx.doi.org/10.1175/1520-0450(1984)023<0222:TIOASO>2.0.CO;2.

- Mellor, G. L., and T. Yamada (1982), Development of a turbulence closure model for geophysical fluid problems, *Rev. Geophys. Space Phys.*, 20, 851-875, doi:10.1029/RG020i004p00851.
- Milovac, J., J. Ingwersen, and K. Warrach-Sagi (2014a), Soil texture forcing data for the whole world for the Weather Research and Forecasting (WRF) Model of the University of Hohenheim (UHOH) based on the Harmonized World Soil Database (HWSD) at 30 arc-second horizontal resolution, World Data Centre for Climate (WDCC), doi:10.1594/WDCC/WRF_NOAH_HWSD_world_TOP_SOILTYP
- Milovac, J., J. Ingwersen, and K. Warrach-Sagi (2014b), Top soil texture forcing data for the area of Germany for the Weather Research and Forecasting (WRF) Model based on the Bodenerhebungs- und -bewertungskarte (BUK) at a scale 1:1000000 (BUK1000) and provided by the University of Hohenheim (UHOH), World Data Centre for Climate (WDCC), doi:10.1594/WDCC/WRF_NOAH_BUK_Ger_top_SOILTYP
- Milovac, J., K. Warrach-Sagi, A. Behrendt, F. Späth, J. Ingwersen, and V. Wulfmeyer (2016), Investigation of PBL schemes combining the WRF model simulations with scanning water vapour differential absorption lidar measurements, *J. Geophys. Res. Atmos.*, 121, 624–649, doi:10.1002/2015JD023927.
- Mirocha, J. D., B. Kosovic, M. L. Aitken, and J. K. Lundquist (2014), Implementation of a generalized actuator disk wind turbine model into the weather research and forecasting model for large-eddy simulation applications, *Journal of Renewable and Sustainable Energy*, 6, 013104, doi:http://dx.doi.org/10.1063/1.4861061.
- Misenis, C., and Y. Zhang (2010), An examination of sensitivity of WRF/Chem predictions to physical parameterizations, horizontal grid spacing, and nesting options, *Atmos. Res.*, 97, 315–334, doi:10.1016/j.atmosres.2010.04.005.
- Moeng, C.-H., and P. P. Sullivan, P. P. (1994), A Comparison of Shear- and Buoyancy-Driven Planetary Boundary Layer Flows, *J. Atmos. Sci.*, 51, 999–1022, doi:http://dx.doi.org/10.1175/1520-0469(1994)051<0999:ACOSAB>2.0.CO;2.
- Morrison, H., Curry, J. A., and Khvorostyanov, V. I. (2005), A New Double-Moment Microphysics Parameterization for Application in Cloud and Climate Models. Part I: Description, *J. Atmos. Sci.*, 62, 1665–1677.

- Muppa, S. K., A. Behrendt, F. Späth, V. Wulfmeyer, S. Metzendorf, and A. Riede (2016), Turbulent humidity fluctuations in the convective boundary layer: Case studies using DIAL measurements, *Bound.-Layer Meteorol.*, 158, 43-66, doi:10.1007/s10546-015-0078-9
- Nakanishi, M. and Niino, H. (2009), Development of an Improved Turbulence Closure Model for the Atmospheric Boundary Layer, *J. Meteor. Soc. Japan*, 87, 895-912, 2009.
- Nielsen, J. R., D. Ebba, A. N. Hahmann, and E. Boegh (2013), Representing vegetation processes in hydrometeorological simulations using the WRF model, *DTU Wind Energy*, 128 p., (Riso – PhD; No. 0016(EN)).
- Nielsen-Gammon, J. W., C. L. Powell, M. J. Mahoney, W. M. Angevine, C. Senff, A. White, C. Berkowitz, K. Doran, and K. Knupp (2008) Multisensor Estimation of Mixing Heights over a Coastal City, *J. Appl. Meteor. Climatol.*, 47, 27–43.
- Niu, G. Y., Z. L. Yang, K. E. Mitchell, F. Chen, M. B. Ek, M. Barlage, A. Kumar, K. Manning, D. Niyogi, E. Rosero, M. Tewari, and Y. Xia (2011), The community Noah land surface model with multiparameterization options (Noah-MP): 1. Model description and evaluation with local-scale measurements, *J. Geophys. Res.*, 116, D12109, doi:10.1029/2010JD015139.
- Noh, Y., W. G. Cheon, S. X. Hong, and S. Raasch (2003), Improvement of the K-profile Model for the Planetary Boundary Layer based on Large Eddy Simulation Data, *Bound. Lay. Meteorol.*, 107, 401–427.
- Olson, J. B., and J. M. Brown (2009) A comparison of two Mellor-Yamada-based PBL schemes in simulating a hybrid barrier jet, Preprints, 23rd Conf. on Weather Analysis and Forecasting/ 19th Conf. on Numerical Weather Prediction, Omaha, NE, Amer. Meteor. Soc., JP1.13. [Available online at <http://ams.confex.com/ams/pdfpapers/154321.pdf>.]
- Otte, M. J., and J. C. Wyngaard (2001), Stably Stratified Interfacial-Layer Turbulence from Large-Eddy Simulation, *J. Atmos. Sci.*, 58, 3424–3442, doi:[http://dx.doi.org/10.1175/1520-0469\(2001\)058<3424:SSILTF>2.0.CO;2](http://dx.doi.org/10.1175/1520-0469(2001)058<3424:SSILTF>2.0.CO;2).
- Pal, J. S. and E. A. B. Eltahir (2001), Pathways relating soil moisture conditions to future summer rainfall within a model of the land–atmosphere system. *J. Climate* 14 (6),

1227–1242,doi:[http://dx.doi.org/10.1175/1520-0442\(2001\)014<1227:PRSMCT>2.0.CO;2](http://dx.doi.org/10.1175/1520-0442(2001)014<1227:PRSMCT>2.0.CO;2)

- Pal, J. S., A. Behrendt, and V. Wulfmeyer (2010), Elastic-backscatter-lidar-based characterization of the convective boundary layer and investigation of related statistics, *Ann. Geophys.*, 28, 825-847, doi:10.5194/angeo-28-825-2010.
- Pino, D., H. Jonker, J. Vilà-Guerau De Arellano, and A. Dosio (2006), Role of Shear and the Inversion Strength During Sunset Turbulence Over Land: Characteristic Length Scales, *Bound.-Lay. Meteorol.*, 121, 537–556, doi:10.1007/s10546-006-9080-6.
- Pleim, J. E.: A Combined Local and Nonlocal Closure Model for the Atmospheric Boundary Layer. Part I: Model Description and Testing, *J. Appl. Meteor. Climatol.*, 46, 1383–1395, 2007a. doi:<http://dx.doi.org/10.1175/JAM2539.1>
- Prandtl, L. (1942), *Führer durch die Strömungslehre*, Vieweg und Sohn, Braunschweig, 648 pp.
- Prein, A. F., W. Langhans, G. Fosser, A. Ferrone, N. Ban, K. Goergen, M. Keller, M. Tölle, O. Gutjahr, F. Feser, et al. (2015), A review on regional convection-permitting climate modeling: Demonstrations, prospects, and challenges, *Rev. Geophys.*, 53, 323–361. doi:10.1002/2014RG000475.
- Radlach, M., A. Behrendt, and V. Wulfmeyer (2008), Scanning rotational Raman lidar at 355 nm for the measurement of tropospheric temperature fields, *Atmos. Chem. Phys.*, 8, 159–169, doi:10.5194/acp-8-159-2008.
- Sanchez, P., S. Ahamed, and F. Carré (2009), Digital soil map of the world, *Science*, 325, 680-681, doi:10.1126/science.1175084.
- Santanello, J. A., M. A. Friedl, and W. P. Kustas (2005), An empirical investigation of convective planetary boundary layer evolution and its relationship with the land surface, *J. Appl. Meteorol.*, 44, 917–32, doi:<http://dx.doi.org/10.1175/JAM2240.1>
- Santanello, J. A., C. D. Peters-Lidard, S. V. Kumar, C. Alonge, and W. K. Tao (2009), A Modeling and Observational Framework for Diagnosing Local Land–Atmosphere Coupling on Diurnal Time Scales, *J. Hydrometeorol.*, 10, 577–599, doi:<http://dx.doi.org/10.1175/2009JHM1066.1>.

- Santanello, J. A., C. D. Peters-Lidard, and S. V. Kumar (2011), Diagnosing the Sensitivity of Local Land–Atmosphere Coupling via the Soil Moisture–Boundary Layer Interaction, *J. Hydrometeor.*, 12, 766–786, doi:<http://dx.doi.org/10.1175/JHM-D-10-05014.1>.
- Santanello, J. A., C. D. Peters-Lidard, A. Kennedy, and S. V. Kumar (2013), Diagnosing the Nature of Land–Atmosphere Coupling: A Case Study of Dry/Wet Extremes in the U.S. Southern Great Plains, *J. Hydrometeor.*, 14, 3–24, doi:<http://dx.doi.org/10.1175/JHM-D-12-023.1>.
- Seibert, P. (2000), Review and intercomparison of operational methods for the determination of the mixing height, *Atmos. Environ.*, 34, 1001–1027, doi:[10.1016/S1352-2310\(99\)00349-0](https://doi.org/10.1016/S1352-2310(99)00349-0).
- Seidel, D. J., C. O. Ao, and K. Li (2010), Estimating climatological planetary boundary layer heights from radiosonde observations: Comparison of methods and uncertainty analysis, *J. Geophys. Res.*, 115, D16113, doi:[10.1029/2009JD013680](https://doi.org/10.1029/2009JD013680).
- Seneviratne, S. I., D. Lüthi, M. Litschi and C. Schär (2006), Land-atmosphere coupling and climate change in Europe. *Nature* 443, 205-209, doi:[10.1038/nature05095](https://doi.org/10.1038/nature05095).
- Seneviratne, S.I., and R. Stöckli (2008), The role of land-atmosphere interactions for climate variability in Europe. In: *Climate Variability and Extremes during the Past 100 years*, Brönnimann et al. (eds.), *Adv. Global Change Research*, 33, Springer Verlag. (Book chapter).
- Seneviratne, S. I., T. Corti, E. L. Davin, M. Hirschi, E. B. Jaeger, I. Lehner, B. Orlowsky, and A. J. Teuling (2010), Investigating soil moisture-climate interactions in a changing climate: A review, *Earth-Sci. Rev.*, 99, 125-161, doi:[10.1016/j.earscirev.2010.02.004](https://doi.org/10.1016/j.earscirev.2010.02.004).
- Sherwood, S. C., R. Roca, T. M. Weckwerth, and N. G. Andronova (2010), Tropospheric water vapour, convection, and climate, *Rev. Geophys.*, 48, RG 2001, doi:[10.1029/2009RG000301](https://doi.org/10.1029/2009RG000301)
- Shin, H. H., and S. Y. Hong (2011), Intercomparison of Planetary Boundary-Layer Parameterizations in the WRF Model for a Single Day from CASES-99, *Bound. Lay. Meteorol.*, 139, 261–281, doi:[10.1007/s10546-010-9583-z](https://doi.org/10.1007/s10546-010-9583-z)

- Simmer, C., M. Masbou, I. Thiele-Eich, W. Amelung, S. Crewell, B. Diekkrüger, F. Ewert, H. Hendricks-Franssen, J. A. Huisman, A. Kemna, N. Klitzsch, S. Kollet, M. Langensiepen, U. Löhnert, A. M. Rahman, U. Rascher, K. Schneider, J. Schween, Y. Shao, P. Shrestha, M. Stiebler, M. Sulis, J. Vanderborght, H. Vereecken, J. van der Kruk, G. Waldhoff, and T. Zerenner (2015), Monitoring and Modeling the Terrestrial System from Pores to Catchments – the Transregional Collaborative Research Center on Patterns in the Soil-Vegetation-Atmosphere System, *B. Am. Meteorol. Soc.*, 96 (10), 1765 – 1787, doi:10.1175/BAMS-D-13-00134.1.
- Skamarock, W. C., J. B. Klemp, J. Dudhia, D. O. Gill, D. M. Barker, M. Duda, X. Y. Huang, W. Wang, and J. G. Powers (2008), A Description of the Advanced Research WRF Version 3. NCAR Technical Note, doi:10.5065/D68S4MVH.
- Sorbjan, Z. (1989), *Structure of the Atmospheric Boundary Layer*, Prentice Hall, Englewood Cliffs, N. J., 317 pp.
- Späth, F., A. Behrendt, S. K. Muppa, S. Metzendorf, A. Riede, and V. Wulfmeyer (2016), 3-D water vapor field in the atmospheric boundary layer observed with scanning differential absorption lidar, *Atmos. Meas. Tech.*, 9, 1701-1720, doi:10.5194/amt-9-1701-2016.
- Stéfanon, M., P. Drobinski, F. D’Andrea, C. Lebeaupin-Brossier, and S. Bastin (2014), Soil moisture-temperature feedbacks at meso-scale during summer heat waves over Western Europe, *Clim. Dyn.*, 42, 1309–1324, doi:10.1007/s00382-013-1794-9.
- Stull, R. B. (1988), *An Introduction to Boundary Layer Meteorology*, Kluwer Academic Publishers, Dordrecht, 666 pp.
- Talbot, C., E. Bou-Zeid, and J. Smith (2012) Nested Mesoscale Large-Eddy Simulations with WRF: Performance in Real Test Cases. *J. Hydrometeor.*, 13, 1421–1441, doi:http://dx.doi.org/10.1175/JHM-D-11-048.1
- Taylor, C. M., R. A. M. de Jeu, F. Guichard, P. P. Harris, and W. A. Dorigo (2012), Afternoon rain more likely over drier soils, *Nature*, 489, 423–426, doi:10.1038/nature11377.

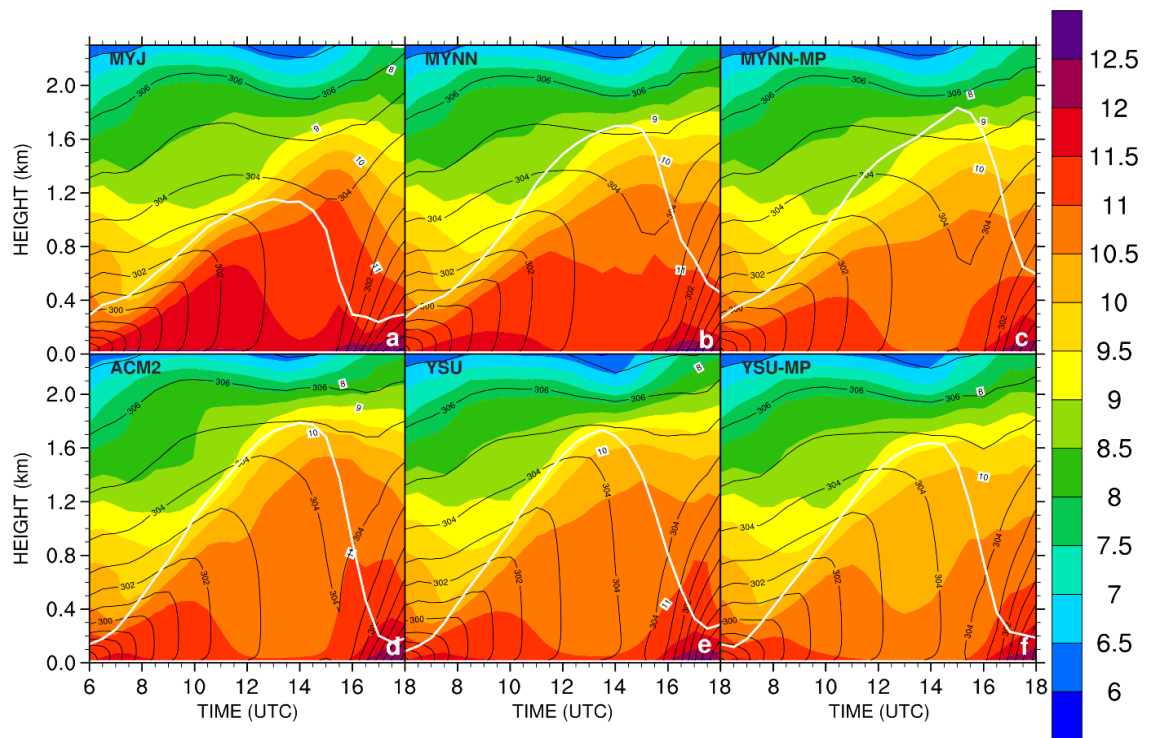
- Teixeira, J., and S. Cheinet (2004), A Simple Mixing Length Formulation for the Eddy-Diffusivity Parameterization of Dry Convection, *Bound. Lay. Meteorol.*, 110, 435–453, doi:10.1029/2003GL017377.
- Teuling, A.J., M. Hirschi, A. Ohmura, M. Wild, M. Reichstein, P. Ciais, N. Buchmann, C. Ammann, L. Montagnani, A.D. Richardson, G. Wohlfahrt, and S.I. Seneviratne (2009), A regional perspective on trends in continental evaporation, *Geophys. Res. Lett.*, 36, L02404, doi:10.1029/2008GL036584.
- Tribbia, J., and D. Baumhefner (2004), Scale interactions and atmospheric predictability: An updated perspective. *Mon. Wea. Rev.*, 132, 703–713, doi:10.1175/1520-0493(2004)132,0703: SIAAPA.2.0.CO;2
- Trier, S.B. (2003), Convective storms: Convective initiation, in *Encycl. Atmos. Sci.*, Academic Press, 560-569, (Book chapter).
- Turner, D.D., R.A. Ferrare, L.A. Heilman Brasseur, W.F. Feltz, and T.P. Tooman (2002), Automated retrievals of water vapour and aerosol profiles from an operational Raman lidar, *J. Atmos. Oceanic Technol.*, 19, 37-50, DOI:10.1175/1520-0426(2002)019<0037:AROWVA>2.0.CO;2.
- van Heerwaarden, C.C., J. Vilà-Guerau de Arellano, A.F. Moene and A.A.M. Holtslag (2009), Interactions between dry-air entrainment, surface evaporation and convective boundary layer development, *Q. J. R. Meteorol. Soc.*, 135, 1277-1291, doi:10.1002/qj.431
- van der Velde, R., Z. Su, M. Ek, M. Rodell, and Y. Ma (2009), Influence of thermodynamic soil and vegetation parameterizations on the simulation of soil temperature states and surface fluxes by the Noah LSM over a Tibetan plateau site, *Hydrol. Earth Syst. Sci.*, 13, 759-777, doi:10.5194/hess-13-759-2009.
- Wagner, G., A. Behrendt, V. Wulfmeyer, F. Späth, and M. Schiller (2013), High-power Ti:sapphire laser at 820nm for scanning ground-based water-vapour differential absorption lidar, *Appl. Optics*, 52, 2454–2469, doi:10.1364/AO.52.002454.
- Warrach-Sagi, K., V. Wulfmeyer, R. Grasselt, F. Ament, and C. Simmer (2008), Streamflow simulations reveal the impact of the soil parameterization, *Meteorol. Z.*, 17, 751-762, doi:10.1127/0941-2948/2008/0343.

- Warrach-Sagi, T. Schwitalla, V. Wulfmeyer, and H.-S. Bauer (2013), Evaluation of a simulation based on the WRF-Noah model system: Precipitation in Germany. *Climate Dyn.*, 41, 755–774, doi:10.1007/s00382-013-1727-7
- Williams, K. D., A. Bodas-Salcedo, M. Déqué, S. Fermepin, B. Medeiros, M. Watanabe, C. Jakob, S. A. Klein, C. A. Senior, and D. L. Williamson (2013), The Transpose-AMIP II Experiment and Its Application to the Understanding of Southern Ocean Cloud Biases in Climate Models, *J. Climate*, 26, 3258–3274, doi:http://dx.doi.org/10.1175/JCLI-D-12-00429.1.
- Wizemann, H.-D., J. Ingwersen, P. Högy, K. Warrach-Sagi, T. Streck, and V. Wulfmeyer (2015), Three year observations of water vapour and energy fluxes over agricultural crops in two regional climates of Southwest Germany, *Meteorol. Z.*, 24(1), 39-59, doi:10.1127/metz/2014/0618
- Wulfmeyer, V. (1999a), Investigation of Turbulent Processes in the Lower Troposphere with Water Vapour DIAL and Radar-RASS, *J. Atmos. Sci.*, 56, 1055–1076, doi:http://dx.doi.org/10.1175/1520-0469(1999)056<1055:IOTPIT>2.0.CO;2.
- Wulfmeyer, V. (1999b), Investigations of humidity skewness and variance profiles in the convective boundary layer and comparison of the latter with large eddy simulation results, *J. Atmos. Sci.*, 56, 1077–1087, doi:http://dx.doi.org/10.1175/1520-0469(1999)056<1077:IOHSAV>2.0.CO;2.
- Wulfmeyer, V., A. Behrendt, H. S. Bauer, C. Kottmeier, U. Corsmeier, A. Blyth, G. Craig, U. Schumann, M. Hagen, S. Crewell, P. Di Girolamo, C. Flamant, M. Miller, A. Montani, S. Mobbs, E. Richard, M. W. Rotach, M. Arpagaus, H. Russchenberg, P. Schlüssel, M. König, V. Gärtner, R. Steinacker, M. Dorninger, D. D. Turner, T. Weckwerth, A. Hense, and C. Simmer (2008), The Convective and Orographically-induced Precipitation Study: A Research and Development Project of the World Weather Research Program for improving quantitative precipitation forecasting in low-mountain regions, *Bull. Amer. Meteor. Soc.*, 89, 1477-1486, doi:10.1175/2008BAMS2367.1.
- Wulfmeyer, V., and T. Janjić (2005), Twenty-Four-Hour Observations of the Marine Boundary Layer Using Shipborne NOAA High-Resolution Doppler Lidar, *J. Appl. Meteor.*, 44, 1723–1744, doi:http://dx.doi.org/10.1175/JAM2296.1.

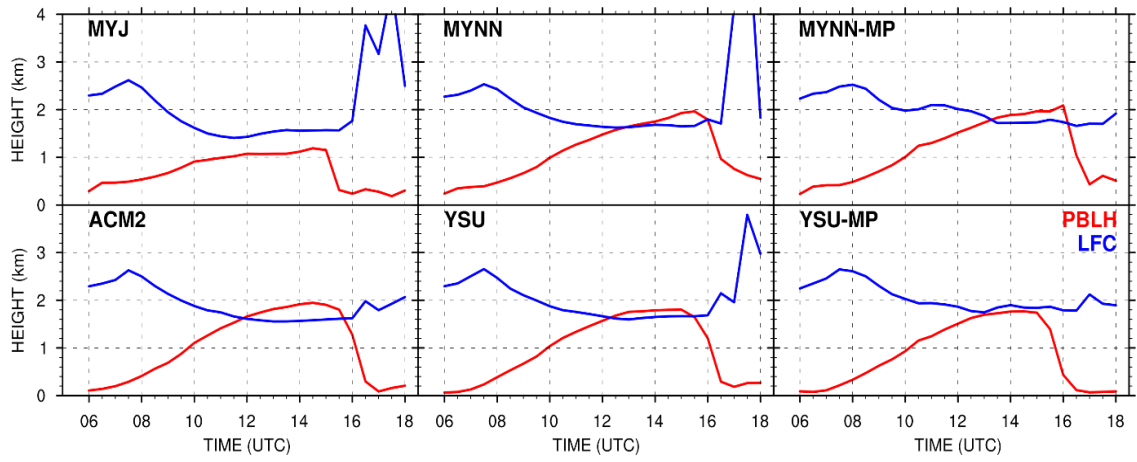
- Wulfmeyer, V., A. Behrendt, C. Kottmeier, U. Corsmeier, C. Barthlott, G. C. Craig, M. Hagen, D. Althausen, F. Aoshima, M. Arpagaus, H. S. Bauer, L. Bennett, A. Blyth, C. Brandau, C. Champollion, S. Crewell, G. Dick, P. Di Girolamo, M. Doringner, Y. Dufournet, R. Eigenmann, R. Engelmann, C. Flamant, T. Foken, T. Gorgas, M. Grzeschik, J. Handwerker, C. Hauck, H. Höller, W. Junkermann, N. Kalthoff, C. Kiemle, S. Klink, M. König, L. Krauss, C. N. Long, F. Madonna, S. Mobbs, B. Neiningner, S. Pal, G. Peters, G. Pigeon, E. Richard, M. W. Rotach, H. Russchenberg, T. Schwitalla, V. Smith, R. Steinacker, J. Trentmann, D. D. Turner, J. van Baelen, S. Vogt, H. Volkert, T. Weckwerth, H. Wernli, A. Wieser, and M. Wirth (2011), The Convective and Orographically-induced Precipitation Study (COPS): the scientific strategy, the field phase, and research highlights, *Q.J.R. Meteorol. Soc.*, 137: 3–30, doi:10.1002/qj.752.
- Wulfmeyer, V., O. Branch, K. Warrach-Sagi, H.-S. Bauer, T. Schwitalla, and K. Becker (2014a), The Impact of Plantations on Weather and Climate in Coastal Desert Regions, *J. Appl. Meteorol. Climatol.*, 53:5, 1143-1169, doi:http://dx.doi.org/10.1175/JAMC-D-13-0208.1.
- Wulfmeyer, V., K. Warrach-Sagi, T. Schwitalla, H. S. Bauer, and J. Milovac (2014b), Towards seamless mesoscale prediction of the land system for Europe, The World Weather Open Science Conference, Montreal, Canada, August 16-21.
- Wulfmeyer, V., R. M. Hardesty, D. D. Turner, A. Behrendt, M. P. Cadeddu, P. Di Girolamo, P. Schlüssel, J. Van Baelen, and F. Zus (2015a), A review of the remote sensing of lower tropospheric thermodynamic profiles and its indispensable role for the understanding and the simulation of water and energy cycles, *Rev. Geophys.*, 53, 819–895, doi:10.1002/2014RG000476
- Wulfmeyer, V. and Coauthors (2015b), New concepts for studying land-surface-atmosphere feedback based on a new lidar synergy and grey zone simulations. *Geophys. Res. Abstr.*, Vol. 17, EGU2015-5054, EGU General Assembly 2015 [available online at <http://meetingorganizer.copernicus.org/EGU2015/EGU2015-5054.pdf>]
- Wulfmeyer, V., S. K. Muppa, A. Behrendt, S. M. E. Hammann, F. Späth, Z. Sorbjan, D. D. Turner, and R. M. Hardesty (2016), Determination of convective boundary layer entrainment fluxes, dissipation rates, and the molecular destruction of variances:

- Theoretical description and a strategy for its confirmation with a novel lidar system synergy, *J. Atmos. Sci.*, 73 (2), 667-692, doi:10.1175/JAS-D-14-0392.1.
- Xie, B., J. C. H. Fung, A. Chan, and A. Lau (2012), Evaluation of nonlocal and local planetary boundary layer schemes in the WRF model, *J. Geophys. Res.*, 117, D12103, doi:10.1029/2011JD017080.
- Xie, B., J. C. R. Hunt, D. J. Carruthers, J. C. H. Fung, and J. F. Barlow (2013), Structure of the planetary boundary layer over Southeast England: Modeling and measurements. *J. Geophys. Res. Atmos.*, 118, 7799–7818, doi:10.1002/jgrd.50621.
- Yang, Z. L., G. Y. Niu, K. E. Mitchell, F. Chen, M. B. Ek, M. Barlage, L. Longuevergne, K. Manning, D. Niyogi, M. Tewari, and Y. Xia (2011), The community Noah land surface model with multiparameterization options (Noah-MP): 2. Evaluation over global river basins, *J. Geophys. Res.*, 116, D12110, doi:10.1029/2010JD015140.
- Zhang, Y., J. Hemperly, N. Meskhidze, and W. Skamarock (2012), The Global Weather Research and Forecasting (GWRf) Model: Model Evaluation, Sensitivity Study, and Future Year Simulation. *Atmospheric and Climate Sciences*, 2, 231–253, doi:10.4236/acs.2012.23024
- Zhang, Y., Z. Gao, D. Li, Y. Li, N. Zhang, X. Zhao, and J. Chen (2014), On the computation of planetary boundary layer height using the bulk Richardson number method, *Geosci. Model Dev. Discuss.*, 7, 4045-4079, doi:10.5194/gmd-7-2599-2014.
- Zolina, O., C. Simmer, K. Belyaev, S. K. Gulev, and P. Koltermann (2013), Changes in the Duration of European Wet and Dry Spells during the Last 60 Years, *J. Climate*, 26, 2022–2047, doi:http://dx.doi.org/10.1175/JCLI-D-11-00498.1.

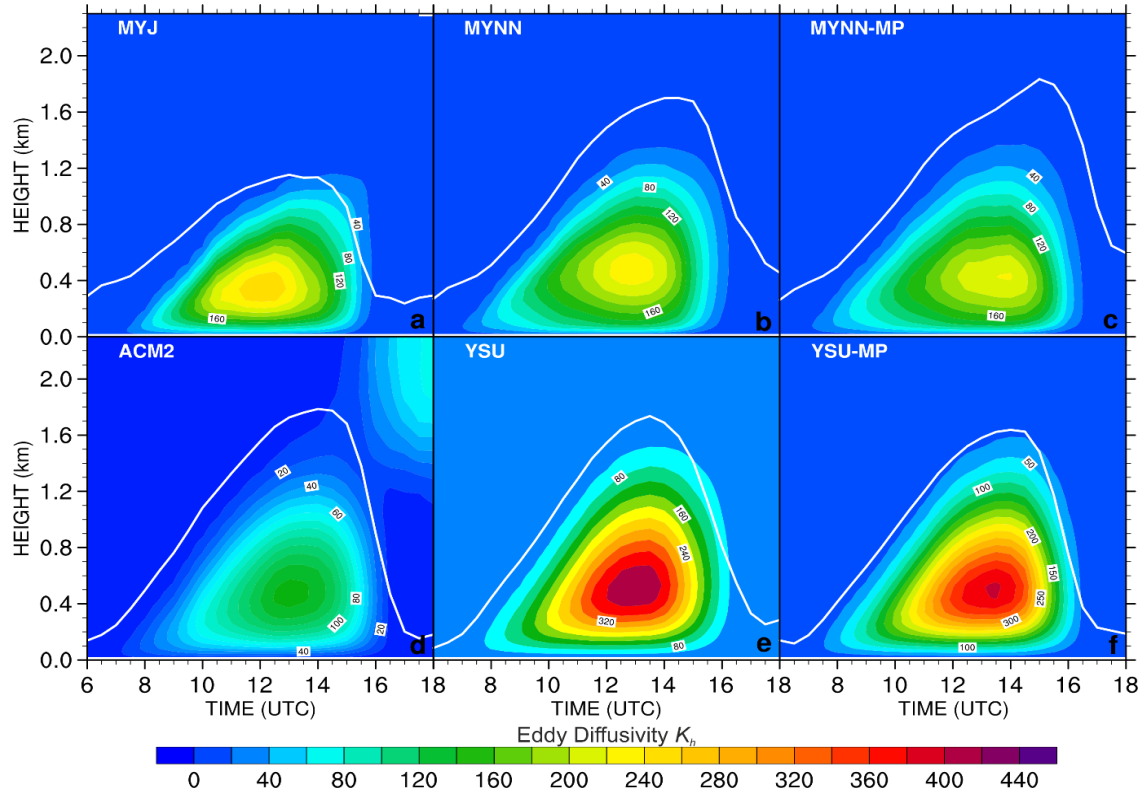
12. Appendices



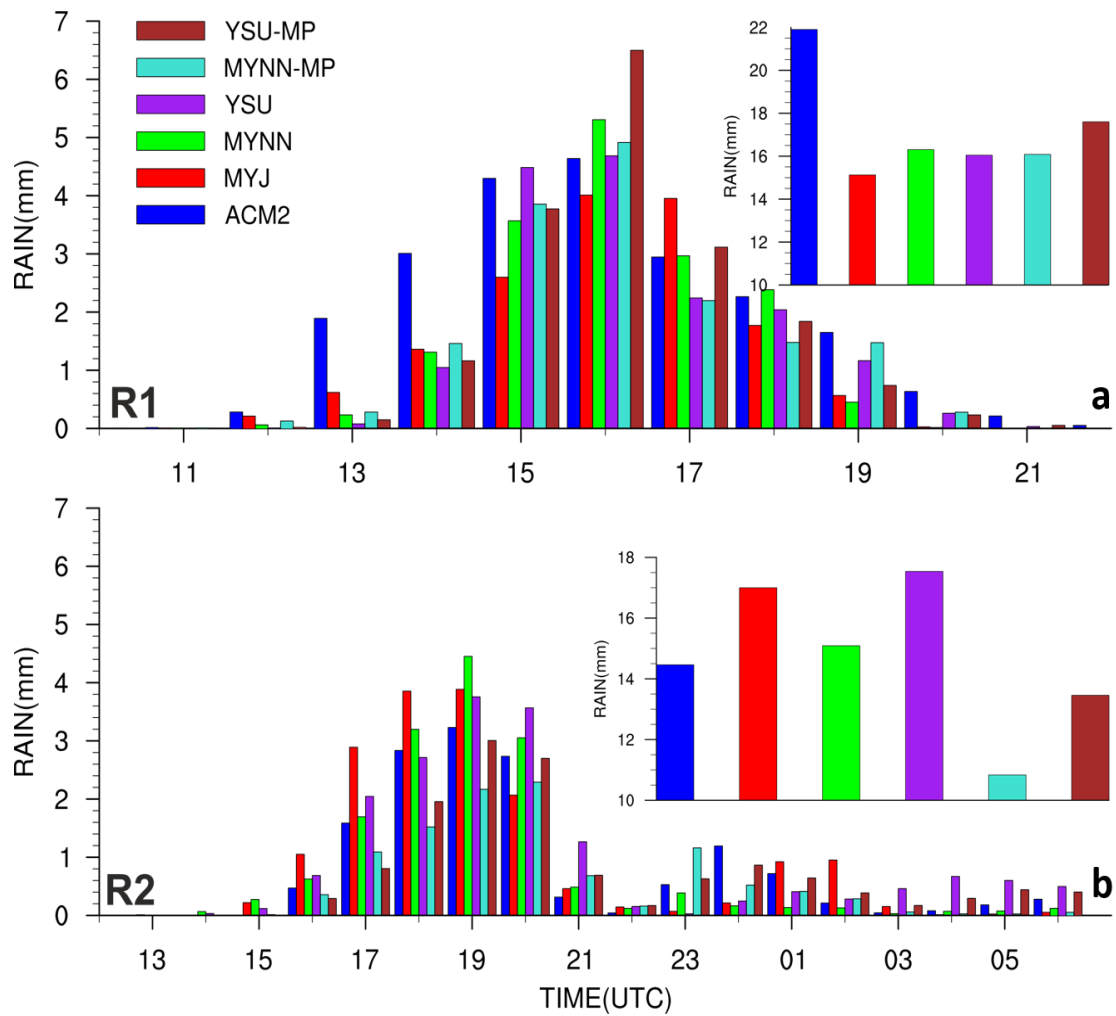
A1. Temporal change of vertical profiles of q in gkg^{-1} from 6 to 18 UTC on 25 August 2009 averaged over the R2 region. Overlaid are lines for θ (black; K) and the PBLH (white; km).



A2. The simulated time series of the PBLH and LFC on 25 August 2009 averaged over the grid cells with accumulated precipitation exceeding 30 mm between 13 and 18 UTC within R2.



A3. Temporal change of the eddy diffusivity for scalars K_h from 6 to 18 UTC on 25 August 2009 averaged over the R2 region. Overlaid white lines denote the PBLH in km.



A4. Hourly accumulated precipitation on 25 August 2009 averaged over the R1 (a) and over R2 (b). The spatial mean of the accumulated 24 h precipitation for the each experiment is given in the upper right corners of the panels.

Curriculum Vitae

Personal Data

Name: Josipa Milovac
Address: Lupinenstr. 15, 70599 Stuttgart
Date of Birth: 19 July 1979
Place of Birth: Split, Croatia
Citizenship: Croatian

Education

2012 – Present University of Hohenheim, PhD student
1998 – 2011 University of Zagreb, Department of Geophysics, Faculty of
Science, Croatia, M.Sc. in Physics – Geophysics
1994 – 1998 Grammar School “Josip Pupacic”, Omis, Croatia

Work History

06/2012 – 02/2016 Researcher on the RU 1695 project, University of Hohenheim,
Stuttgart, Germany
02/2003 – 05/2012 Meteorologist in Meteo centar d.o.o., Zagreb, Croatia
02/2004 – 12/2008 TV producer and weather presenter on RTL Croatia television,
Zagreb, Croatia

Publications

Milovac, J., Warrach-Sagi, K., Behrendt, A., Späth, F., Ingwesen, J. and V. Wulfmeyer
(2016), Investigation of PBL schemes combining the WRF model simulations with
scanning water vapour differential absorption lidar measurements, *J. Geophys. Res.*
Atmos., 121, 624-649, doi:10.1002/2015JD023927.

- Milovac, J., O.-L. Branch, H.-S. Bauer, T. Schwitalla, K. Warrach-Sagi, and V. Wulfmeyer (2016), High-Resolution WRF Model Simulations of Critical Land Surface-Atmosphere Interactions within Arid and Temperate Climates (WRFCLIM), In: "High Performance Computing in Science and Engineering 15", Eds: Wolfgang E. Nagel, Dietmar H. Kroener, Michael M. Resch, pp 607-622, doi:10.1007/978-3-319-24633-8_39.
- Milovac, J., J. Ingwersen, and K. Warrach-Sagi (2014), Soil texture forcing data for the whole world for the Weather Research and Forecasting (WRF) Model of the University of Hohenheim (UHOH) based on the Harmonized World Soil Database (HWSD) at 30 arc-second horizontal resolution, World Data Centre for Climate (WDCC).
- Milovac, J., J. Ingwersen, and K. Warrach-Sagi (2014), Top soil texture forcing data for the area of Germany for the Weather Research and Forecasting (WRF) Model based on the Bodenubersichtskarte (BUK) at a scale 1:1000000 (BUK1000) and provided by the University of Hohenheim (UHOH), World Data Centre for Climate (WDCC).
- Warrach-Sagi, K., H.-S. Bauer, T. Schwitalla, J. Milovac, O. Branch, and V. Wulfmeyer (2014), High-resolution climate predictions and short -range forecasts to improve the process understanding and the representation of land-surface interactions in the WRF model in Southwest Germany (WRFCLIM), In: "High Performance Computing in Science and Engineering '14", Eds: Wolfgang E. Nagel, Dietmar H. Kroener, Michael M. Resch, pp 575-592, doi:10.1007/978-3-319-10810-0_38.
- Warrach-Sagi, K., H.-S. Bauer, O. Branch, J. Milovac, T. Schwitalla, and V. Wulfmeyer (2013), High-resolution climate predictions and short-range forecasts to improve the process understanding and the representation of land-surface interactions in the WRF model in Southwest Germany (WRFCLIM), In: "High Performance Computing in Science and Engineering 13", Eds: Wolfgang E. Nagel, Dietmar H. Kroener, Michael M. Resch, pp 531-544, doi:10.1007/978-3-319-02165-2_36.
- Master degree thesis:* Milovac, J. (2011), An implementation of the new generalized mixing length scale into the numerical model WRF (in Croatian), available at https://bib.irb.hr/datoteka/512874.DIPLOMSKI_RAD_JOSIPA_MILOVAC.pdf.

Conferences contribution

Poster presentations:

Milovac, J., K. Warrach-Sagi, A. Behrendt, F. Späth, F. and V. Wulfmeyer (2014), Sensitivity of the WRF model to PBL schemes and LSMs: Comparisons with water vapour DIAL measurements, GEWEX conference, The Hague, Netherlands, (July 14 – 17), awarded a “Certificate of Achievement” and second prize at the 7th GEWEX conference.

Milovac, J., K. Warrach-Sagi, A. Behrendt, F. Späth, and V. Wulfmeyer: Sensitivity of WRF to PBL schemes and LSMs in simulating humidity profiles (2014), Comparisons with water vapour DIAL measurements, 21st Symposium on Boundary Layers and Turbulence, Leeds, Great Britain (June 09 – 13), awarded a “Commended Student Poster Presentation at AMS 21BLT”.

Milovac, J., K. Warrach-Sagi, A. Behrendt, F. Späth, V. Wulfmeyer, and T. Schwitalla (2013), WRF absolute humidity profile simulations: Sensitivity studies and comparisons against scanning water vapour DIAL measurements, 14th Annual WRF Users' Workshop, Boulder, Colorado, The USA, (June 24 – 28).

Grisogono, B., J. Milovac, M. T. Prtenjak, and T. Bašić (2011), An airflow over the Dinaric Alps simulated with a modified mixing-length formulation in WRF model, ICAM, Aviemore, Scotland, (May 23 - 27).

Oral presentation:

Milovac, J., Späth, F., Warrach-Sagi, K., Behrendt, A., and V. Wulfmeyer V.: Evaluation of WRF BL parameterization schemes and LS models by comparing an ensemble with 44 members with scanning water vapour DIAL measurements, TR32-HOBE Int. Symposium “Patterns in Soil Vegetation Atmosphere Systems: Monitoring, Modelling and Data Assimilation”, Bonn, Germany 2013 (March 11 – 14).

Declaration of Originality

I, Josipa Milovac, hereby declare that the present dissertation and the work reported herein was composed by and originated entirely from me without any help. All sources used from published or unpublished work of others are reported in the list of references. All parts of my work that are based on others' work are cited as such. This dissertation has not been submitted for any degree or other purposes, neither at the University of Hohenheim nor at any other university or college.

Stuttgart, 19 July 2016

Affidavit according to Sec. 7(7) of the University of Hohenheim doctoral degree regulations for Dr. rer. nat.

1. For the dissertation submitted on the topic

“Studies of soil-vegetation-atmosphere feedback processes with WRF on the convection permitting scale”

I hereby declare that I independently completed the work.

2. I only used the sources and aids documented and only made use of permissible assistance by third parties. In particular, I properly documented any contents which I used - either by directly quoting or paraphrasing - from other works.
3. I did not accept any assistance from a commercial doctoral agency or consulting firm.
4. I am aware of the meaning of this affidavit and the criminal penalties of an incorrect or incomplete affidavit.

I hereby confirm the correctness of the above declaration: I hereby affirm in lieu of oath that I have, to the best of my knowledge, declared nothing but the truth and have not omitted any information.

Place and Date

Signature